

---

# Gas Flows and Stars in Nuclear Regions of Nearby Seyfert Galaxies

Ming-Yi Lin

---



München 2017



---

# Gas Flows and Stars in Nuclear Regions of Nearby Seyfert Galaxies

Ming-Yi Lin

---

Dissertation  
an der Fakultät für Physik  
der Ludwig-Maximilians-Universität  
München

vorgelegt von  
Ming-Yi Lin  
aus Taipei, Taiwan

München, den 28. Juli 2017

Erstgutachter: Prof. Dr. Reinhard Genzel

Zweitgutachter: Prof. Dr. Andreas Burkert

Tag der mündlichen Prüfung: 9. Oktober 2017

# Zusammenfassung

Aktive Galaxienkerne (AGNs) werden durch das Wachstum von supermassiven Schwarzen Löchern (SMBHs), die sich im Zentrum jeder Galaxie befinden, mit Energie versorgt. Wenn man jedoch die Entstehungsgeschichte von SMBHs betrachtet, so ist der Zeitraum ihrer Aktivität nur wenige  $10^8$  Jahre. Auch die physikalischen Prozesse, die zu AGN-Aktivität führen, müssen noch im Detail studiert werden. Die enge Korrelation zwischen der Masse von SMBHs und den Eigenschaften der sphäroidalen Bulge-Komponente ihrer Wirtsgalaxien legt eine Koevolution der SMBHs und ihrer Wirtsgalaxien nahe. Aus der Beobachterperspektive stellen die zentralen Regionen innerhalb des galaktischen Bulges ein großartiges Labor dar, um sich mit dem Wachstum und Feedback von AGNs im Zusammenhang mit Galaxienentwicklung zu befassen. In dieser Arbeit werden die zentralen Bereiche nahgelegener AGNs mit modernsten Beobachtungstechniken studiert, um wichtige Erkenntnisse zu diesen Themen zu erlangen. Zwei Wellenlängenbereiche werden hier diskutiert: Millimeter und Nahinfrarot.

Wir diskutieren das dichte, molekulare Gas in den Zentralregionen nahgelegener Seyfert-Galaxien und präsentieren neue Millimeterbeobachtungen mit Bogensekundenauflösung der HCN (1-0) und HCO+(1-0) Molekularlinien von 3 Objekten. NGC 3079 zeigt ein komplexes Spektrum, in dem sowohl Selbstabsorption als auch saturierte Kontinuumsabsorption vorhanden sind. Das Kontinuumsabsorptionsprofil besitzt einen Höchstwert nahe der systemischen Geschwindigkeit der Galaxie, der Scheibenrotation auf der Millibogensekunden-Skala darstellt. Ein zweiter, blauverschobener Bestandteil stellt wahrscheinlich einen zentralen Ausfluss dar. Die morphologischen und spektralen Eigenschaften der Emissionslinien erlauben uns, die Dynamik des dichten Gases zu bestimmen. Wir kombinieren unsere kinematische Analyse dieser 3 Objekte mit einem weiteren Objekt, für das Archivdaten zur Verfügung stehen, und einer vorangegangenen, vergleichbaren Analyse 4 anderer Objekte zu einem Sample von 8 Seyfert-Galaxien. Die Emissionslinienkinematik in 7 Galaxien deutet auf eine dicke Scheibenstruktur mit einer radialen Ausdehnung von  $\sim 100$  pc hin, was wiederum nahelegt, dass solche Strukturen häufig sind. Wir finden eine Relation zwischen der zentralen HCN Leuchtkraft und der dynamischen Masse. Wenn wir schließlich eine andere Methode anwenden, um die physikalischen Eigenschaften des Gases um AGN zu untersuchen, so finden wir, dass das interstellare Medium im Zentrum nahgelegener Seyfert-Galaxien konsistent damit ist, von Supernovae dominiert zu sein.

Im zweiten Teil der Arbeit präsentieren wir nahinfrarote Beobachtungsdaten für ein vollständiges, volumenlimitiertes Sample von nahgelegenen AGN, die nach 14-195 keV-

Emission ausgewählt worden sind, zusammen mit einem entsprechenden Sample von inaktiven Galaxien. Wir untersuchen die räumlich aufgelöste stellare Kinematik und die Leuchtkraftverteilung auf einer Skala von 10-150 pc mit SINFONI am Very Large Telescope. Die stellaren Geschwindigkeitsfelder zeigen ein scheibenartiges Rotationsmuster. Ihre kinematische Hauptachse stimmt mit der photometrischen Hauptachse, die durch großskalige Bilder bestimmt worden ist, überein. Die mittlere stellare Oberflächenhelligkeit der inaktiven Galaxien ist im Allgemeinen vergleichbar mit der des entsprechenden AGN Sample, deckt aber eine größere Bandbreite ab. Außerdem finden wir keine AGN Oberflächenhelligkeit unter  $10^3 L_{\odot} \text{pc}^{-2}$  innerhalb der zentralen 50 pc. Nachdem wir die Bulgekomponente abgezogen haben, finden wir einen Überschuss an zentralem stellarem Licht mit einer ausgedehnten zentralen Scheibenstruktur, die einer Radius-Leuchtkraft-Relation folgt. Obwohl wir erwarten, dass die überschüssige Leuchtkraft mit einer Population von dynamisch kühleren, jungen Sternen assoziiert ist, sehen wir keinen entsprechenden systematischen Rückgang in der Geschwindigkeitsdispersion. Das könnte daran liegen, dass diese Galaxien Pseudobulges besitzen, in denen die intrinsische Geschwindigkeitsdispersion zum Zentrum hin zunimmt. Und obwohl die jungen Sterne Auswirkungen auf die beobachtete Kinematik haben, so ist ihr Anteil doch zu gering um über den Bulge zu dominieren und die Zunahme an Dispersion auf kleinen Skalen auszugleichen. Daher ist keine Abnahme der Dispersion feststellbar. Wir finden keine Anzeichen für einen Unterschied in der stellaren Kinematik und Oberflächenhelligkeit von aktiven und inaktiven Galaxien. Wenn wir allerdings die 2D Geschwindigkeitsdispersionsfelder überprüfen, so sehen wir Anzeichen für einen Gradienten entlang der kinematischen Hauptachse. Dies kommt häufig im AGN Sample vor, aber nicht bei den entsprechenden inaktiven Galaxien. Abschließend argumentieren wir, dass die asymmetrische stellare Geschwindigkeitsdispersion durch radiale Zuflüsse von Gas ins Zentrum der Galaxie hervorgerufen wird.

# Abstract

Active Galactic Nuclei (AGNs) are powered by the growth of supermassive black holes (SMBHs), which can be found at the centre of every galaxy. But looking at SMBH formation history, the timescale of the active period is only few  $10^8$  yr. And the relevant physical processes triggering an AGN still need to be investigated in detail. The tight correlation between the mass of SMBH and the properties of host spheroidal bulge component, suggests a SMBH co-evolves with its host galaxy. From the observational point of view, nuclear regions inside the galactic bulge provide a great laboratory to address the feeding and feedback of AGN in galaxy evolution. To give important insights into these topics, this thesis studies the nuclear environments of nearby AGNs with state-of-the-art observational techniques. Two wavelength perspectives are discussed below: millimeter and near-infrared.

We discuss the dense molecular gas in central regions of nearby Seyfert galaxies, and present new arcsec resolution millimeter observations of the HCN (1-0) and HCO+ (1-0) molecular lines for 3 objects. NGC 3079 shows a complex spectra with the coexistence of self-absorption and saturated continuum absorption. The continuum absorption profile has a peak close to galaxy's systemic velocity that traces milliarcsec-scale disk rotation, and a second feature with a blue wing that most likely traces a nuclear outflow. The morphological and spectral properties of the emission lines allow us to constrain the dense gas dynamics. We combine our kinematic analysis for these 3 objects, as well as another with archival data, with a previous comparable analysis of 4 other objects, to create a sample of 8 Seyferts. In 7 of these, the emission line kinematics imply thick disk structures on radial scales of  $\sim 100$  pc, suggesting such structures are a common occurrence. We find a relation between nuclear HCN luminosity and dynamical mass. Finally, adopting a different perspective to probe the physical properties of the gas around AGN, we report that the interstellar medium in the centre of nearby Seyfert galaxies is consistent with an environment dominated by supernova.

In the second part we present the near-infrared observations for a complete volume limited sample of nearby 14-195 keV selected AGNs with a matched sample of inactive galaxies. We study the spatially resolved stellar kinematics and luminosity distributions on scales of 10-150 pc, using the SINFONI instrument on the Very Large Telescope. The stellar velocity fields show a disk-like rotating pattern, for which the kinematic position angle is in agreement with the photometric position angle obtained from large scale images. The mean stellar surface brightness of the inactive galaxy sample is generally comparable

---

to the matched sample of AGN but covers a wider surface brightness range. In addition, we do not find any AGN with surface brightness below  $10^3 L_{\odot} \text{pc}^{-2}$  in the central 50 pc. After removal of the bulge contribution, we find a nuclear stellar light excess with an extended nuclear disk structure, which exhibits a size-luminosity relation. While we expect the excess luminosity to be associated with a dynamically cooler young stellar population, we do not typically see a matching drop in dispersion. This may be because these galaxies have pseudo-bulges in which the intrinsic dispersion increases towards the centre. And although the young stars may have an impact on the observed kinematics, their fraction is too small to dominate over the bulge and compensate the increase in dispersion at small radii, so no dispersion drop is seen. We find no evidence for a difference in the stellar kinematics and stellar surface brightness between active and inactive galaxies. However, when we check the 2D velocity dispersion field, we find that there may be an asymmetric velocity dispersion aligned with the galaxy major axis. It frequently occurs in the AGN sample, rather than the matched sample of inactive galaxies. Finally, we argue the stellar velocity dispersion asymmetry is induced by radial flows inward to the centre of the galaxy.

# Contents

<b>Zusammenfassung</b>	<b>v</b>
<b>1 Introduction</b>	<b>1</b>
1.1 Active Galactic Nucleus (AGN)	1
1.1.1 How are AGN defined? The most salient properties of Seyfert nuclei	3
1.1.2 Unification	5
1.1.3 Characterizing the central SMBH	7
1.2 Importance of host galaxy nuclear regions	8
1.3 The kinematic tracers in the nuclear regions	10
1.3.1 Dense molecular gas	10
1.3.2 Stellar absorption	11
1.4 Techniques to provide high resolution images	11
1.4.1 Plateau de Bure Interferometer (PdBI)	12
1.4.2 Spectrograph for INtegral Field Observations in the Near Infrared (SINFONI)	12
1.5 The outline of this work	13
<b>2 Thick Disks, and an Outflow, of Dense Gas in the Nuclei of Nearby Seyfert Galaxies</b>	<b>15</b>
2.1 Introduction	15
2.2 Observations	19
2.3 Gas distribution and kinematics	20
2.3.1 NGC 3079	23
2.3.2 NGC 6764	30
2.3.3 NGC 5033	30
2.4 Modelling the kinematics	32
2.4.1 Kinematic modelling procedure	32
2.4.2 NGC 7469	35
2.4.3 NGC 6764	36
2.4.4 NGC 5033	37
2.4.5 NGC 3079	38
2.4.6 Kinematics summary	38
2.5 Column density through the inner disk of NGC 3079	39

2.5.1	Column densities . . . . .	39
2.5.2	Origin of the absorption . . . . .	41
2.6	HCN luminosity and dynamical mass . . . . .	43
2.7	Non self-gravitating clouds in NGC 6951 . . . . .	47
2.8	Conclusion . . . . .	50
<b>3</b>	<b>LLAMA: Nuclear stellar properties of Swift BAT AGN and matched inactive galaxies</b>	<b>53</b>
3.1	Introduction . . . . .	53
3.2	Sample selection, observations and data reduction . . . . .	55
3.2.1	Matched Seyfert and inactive galaxy sample . . . . .	57
3.2.2	Observations and standard data reduction . . . . .	58
3.2.3	Differential atmospheric refraction . . . . .	59
3.3	Analysis methods . . . . .	60
3.3.1	Stellar distribution and kinematics . . . . .	60
3.3.2	Continuum luminosity profile . . . . .	65
3.4	Nuclear Stellar Continuum Excess . . . . .	67
3.4.1	Radial distribution of stellar luminosity . . . . .	67
3.4.2	Central excess of stellar light . . . . .	69
3.5	Nuclear stellar kinematics . . . . .	74
3.5.1	Nuclear dilution by non-stellar light . . . . .	74
3.5.2	Kinematic PA versus photometric PA . . . . .	77
3.5.3	Radial average kinematics . . . . .	78
3.5.4	Central velocity dispersion . . . . .	81
3.6	Conclusions . . . . .	84
<b>4</b>	<b>Asymmetric velocity dispersion</b>	<b>87</b>
4.1	Motivation . . . . .	87
4.2	Methods to quantify the asymmetries . . . . .	88
4.2.1	Quantifying asymmetries with <i>kinemetry</i> . . . . .	89
4.2.2	Quantifying asymmetries with a flip-subtracted image . . . . .	92
4.3	Discussion: the plausible origin of the asymmetries . . . . .	94
4.4	Conclusions . . . . .	95
<b>5</b>	<b>Summary &amp; Outlook</b>	<b>97</b>
<b>A</b>	<b>Chapter 3 - Disk, bar, and bulge decomposition</b>	<b>101</b>
<b>B</b>	<b>Chapter 3 - Radial flux and kinematics of individual galaxy</b>	<b>103</b>
	<b>Bibliography</b>	<b>119</b>
	<b>Acknowledgements</b>	<b>131</b>

# List of Figures

1.1	Optical spectrum of Seyfert galaxies . . . . .	4
1.2	Illustration of the AGN unified model . . . . .	6
1.3	Illustration of the host galaxy structures . . . . .	8
2.1	Continuum and integrated molecular emission maps for the 3 Seyfert galaxies	24
2.2	Radio to infrared SED for NGC 3079 . . . . .	25
2.3	Integrated spectrum for NGC 3079 . . . . .	26
2.4	The observed and reconstructed HCN (1-0) line profiles in NGC 3079 . . .	27
2.5	Integrated spectrum for NGC 6764 . . . . .	31
2.6	Integrated spectrum for NGC 5033 . . . . .	31
2.7	The map of the simulated disk models for the 3 Seyfert galaxies . . . . .	36
2.8	Position-Velocity diagram for the HCN(1-0) line in NGC 3079 . . . . .	37
2.9	The sketch for the scenario of nuclear off-centre absorption for NGC 3079 .	42
2.10	Correlation between HCN luminosity and dynamical mass . . . . .	44
2.11	LVG calculations for NGC 6951 . . . . .	48
3.1	CO absorption features observed with VLT-SINFONI . . . . .	61
3.2	Flux distribution of the stellar continuum, CO(2-0) equivalent width (EW), stellar velocity, and stellar velocity dispersion for the AGN sample . . . . .	62
3.3	<i>continued</i> . . . . .	63
3.4	Same as Figure 3.2 & Figure 3.3 but for the matched inactive galaxy sample.	64
3.5	Correlation between bulge to total luminosity ratio and Hubble type . . . . .	66
3.6	Radial distribution of stellar surface brightness . . . . .	68
3.7	The size-luminosity relation of excess nuclear star light . . . . .	70
3.8	Radial average CO(2-0) EW . . . . .	75
3.9	Simulation of the impact of non-stellar continuum on CO(2-0) EW . . . . .	76
3.10	The photometric position angle (PA) versus the kinematic PA . . . . .	78
3.11	Radial average kinematic properties of the CO(2-0) absorption . . . . .	79
3.12	Toy model to explain the velocity dispersion of NGC 7213 (AGN) . . . . .	82
4.1	Quantify asymmetry with <i>kinemetry</i> : Testing the impact of the simulated velocity dispersion asymmetry field on $\sigma_{asym}$ . . . . .	89

4.2	Quantify asymmetry with <i>kinemetry</i> : The $v_{asym}$ , $\sigma_{asym}$ , and $K_{asym}$ as a function of radius. . . . .	90
4.3	Quantify asymmetry with flip-subtract technique: Examples for the AGNs. . . . .	92
4.4	Quantify asymmetry with flip-subtract technique: Examples for the matched inactive galaxies. . . . .	93
4.5	Quantify asymmetry with flip-subtract technique: Residual velocity dispersion as a function of radius . . . . .	93
4.6	H <sub>2</sub> 2.12 $\mu$ m and Br $\gamma$ 2.16 $\mu$ m maps for NGC 7582 . . . . .	95
B.1	ESO 137-34 (Active galaxy in Pair 1) . . . . .	105
B.2	NGC 718 (Inactive galaxy in Pair 6) . . . . .	106
B.3	NGC 3351 (Inactive galaxy in Pair 7) . . . . .	107
B.4	NGC 3783 (Active galaxy in Pair 6) . . . . .	108
B.5	NGC 4224 (Inactive galaxy in Pair 3 and Pair 5) . . . . .	109
B.6	NGC 4254 (Inactive galaxy in Pair 8) . . . . .	110
B.7	NGC 4593 (Active galaxy in Pair 7) . . . . .	111
B.8	NGC 5728 (Active galaxy in Pair 4) . . . . .	112
B.9	NGC 6814 (Active galaxy in Pair 8) . . . . .	113
B.10	NGC 7172 (Active galaxy in Pair 3) . . . . .	114
B.11	NGC 7213 (Active galaxy in Pair 2) . . . . .	115
B.12	NGC 7582 (Active galaxy in Pair 5) . . . . .	116
B.13	NGC 7727 (Inactive galaxy in Pair 1, 2, and 4) . . . . .	117

# List of Tables

1.1	The observed properties of Seyfert nuclei across different wavelengths . . .	2
2.1	Summary of IRAM-PdBI observations for the 3 Seyfert galaxies. . . . .	18
2.2	Summary of the continuum properties for the 3 Seyfert galaxies . . . . .	20
2.3	The observed properties of molecular emissions . . . . .	22
2.4	Summary of simulated disk models . . . . .	34
2.5	Intrinsic kinematics of the modelled rotating disks . . . . .	35
2.6	Summary of the kinematic modelling for 8 Seyfert galaxies . . . . .	39
3.1	Summary of the galaxy properties for LLAMA sample . . . . .	56
3.2	Nuclear properties of AGN and inactive galaxy samples . . . . .	73
A.1	Summary of the model parameters from the best fits with GALFIT . . . .	102



# Chapter 1

## Introduction

A galaxy is a gravitational system containing stars, interstellar medium, dust, and dark matter. Although the flux density increases toward the centre of the galaxy, we still have little knowledge of the central compact object. The essential part is invisible to the eye, namely the 'black hole (BH)', which exhibits a strong gravitational effects that nothing, even particles or light cannot escape from inside it. Observers only can use electromagnetic radiation and kinematics to describe the phenomena related to black holes. Once matter is accreted onto the black hole, it emits vast amounts of radiation within a small area, and then it is called 'Active Galactic Nucleus (AGN)'. There is much observational evidence to show that the central black hole mass tightly correlates with the properties of the spheroidal component of the host galaxy, suggesting they have grown with each other. In this chapter, we first introduce the observed properties of AGN (Section 1.1), and then connect the BH at a galaxy centre with the properties of the host galaxy, especially in the nuclear region within a radius of a few hundred pc (Section 1.2). The appropriate kinematic tracers in the nuclear region of the host galaxy are introduced in Section 1.3. We introduce state-of-the-art observational techniques at millimeter and infrared wavelengths in Section 1.4.

### 1.1 Active Galactic Nucleus (AGN)

In general, the term "Active Galactic Nucleus", or AGN refers to the presence of energetic objects in the nuclei, or central regions of galaxies, which produce prodigious luminosities in tiny volumes. The compact source in the nucleus which emits powerful energy over the whole electromagnetic spectrum (radio, infrared, optical, ultra-violet, X-ray and gamma ray wavebands) with characteristics suggesting the luminosity and the underlying physical mechanism as well cannot be attributed clearly and directly by stars. In some cases, the compact source has an apparent luminosity as much as  $10^4$  times the typical galaxy luminosity in a small volume ( $\ll 1\text{pc}^3$ ) (Peterson , 1997). There is a wide range in AGN bolometric luminosity (bolometric luminosity is a measurement of its total energy emission) covering nearby low-luminosity AGN (LLAGN) emitting about  $10^{41}\text{ erg s}^{-1}$  to distant quasars emitting more than  $10^{48}\text{ erg s}^{-1}$ .

Table 1.1: The observational properties of Seyfert nuclei across different wavelengths.

Observational property	Seyfert 1	Seyfert 1.5	Seyfert 2
Quasar-like nucleus	Yes	Yes	No
Absorbed X-ray ( $N_H \geq 10^{22} \text{ cm}^{-2}$ )	<10%	<30%	>90%
Broad Balmer lines	Yes	Yes	No
Narrow Balmer lines	Yes	Yes	Yes
K-band colour temperatures	High (>1000K)	High (>1000K)	Low (<1000K)
Radio	Quiet	Quiet	Quiet
Optical variability	Some	Few	No
Polarization	Weak	Weak	Some

In fact, the AGNs are the most luminous and persistent objects across the Universe, their high luminosities and distinctive spectrum making it easy to pick them out at great distances. Therefore, they represent a majority among the sources analysed by recent studies at high redshifts. Their evolution as a function of cosmic time can also put constraints on the studies of the origin, evolution, and ultimate fate of the universe. Studying the host galaxies of high redshift AGN in detail is limited by spatial resolution, whereas nearby AGN offer an opportunity to probe detailed structures down to a few hundred pc scales from the central BH.

Basically, the two largest groups of AGNs are Seyfert galaxies and quasars. The fundamental difference between these two groups is in the amount of radiation emitted by the central compact source. Quasars have luminosities sufficient to outshine their host galaxies, but are rare in the local Universe. By contrast, Seyfert galaxies have quasar-like nuclei whose photometric images show high surface brightnesses, and subsequent spectrum reveal strong high ionization emission lines, but their host galaxies are clearly detected. Seyfert galaxies are very common (10% of all galaxies, Ho (2008)) in the local Universe. In the direct observations through a large telescope show that a Seyfert galaxy looks like a distant normal spiral galaxy with an unresolved star superimposed on the centre.

According to the radio luminosity dichotomy, AGNs can be separated into radio-loud and radio-quiet sources. Radio-loud AGNs have ratios of radio 5 GHz to optical B band flux  $\geq 30$ , which is approximately equivalent to 15-20% of all AGNs (Kellermann et al., 1989; Krolik, 1999). All of our sample are radio quiet Seyfert galaxies, meaning that they are not very luminous at radio wavelengths. However their nuclei still can emit synchrotron radiation as a compact core, which is sometimes accompanied by an inefficient and weak radio jet in the radio maps. Hence in the following sections mostly focus on an introduction based on the radio-quiet Seyfert galaxy viewpoint.

### 1.1.1 How are AGN defined? The most salient properties of Seyfert nuclei

First we want to know how to identify AGN. Because AGN emit across the whole electromagnetic spectrum, we can identify AGNs by their unique spectra from a multi-wavelength perspective. The identification methods can be generally classified in two ways:

(i) AGN continuum: it can be a monochromatic luminosity or a ratio between two different continuum wavebands. A non-thermal power-law continuum (determined by measuring the continuum slope) is also direct evidence for AGN activity, because AGN spectra cannot be described in terms of blackbody radiation, either as a single temperature or as a composite within a small range of temperature;

(ii) specific emission lines: the presence of emission lines at UV, optical, and infrared wavelengths. The presence of emission lines with high ionization potential indicates a high photoionization state in the surrounding gas. In addition, broad emission lines with full width half maximum (FWHM) of  $5000 \text{ km s}^{-1}$  (ranging from  $500\text{--}10000 \text{ km s}^{-1}$  in different objects) are difficult to explain with any stellar-related events.

However, the presence of dust and gas along the line of sight can dilute and mask the emission from the AGN, making the identification of AGN activity a major challenge – especially for the lower luminosity nuclei such as Seyfert galaxies or LLAGNs.

In the following we include a short summary of the observed properties of Seyfert-level AGN (i.e. bolometric luminosity  $< 10^{46} \text{ erg s}^{-1}$  (Ho et al., 1997a)) across different wavelengths. The first spectrum of a Seyfert galaxy was obtained at Lick Observatory in 1908, thus our summary starts from UV/optical, radio, and X-ray, then the final one is infrared/(sub)millimeter. This sorting roughly follows the time sequence of the development for observational astronomy.

- **UV/Optical:** UV/Optical spectrum separate the Seyfert galaxies into two distinct classes, based on their relative widths of forbidden lines and Balmer lines (Khachikian & Weedman, 1974). In Seyfert class 1 (the right panel of Figure 1.1), the Balmer lines, mainly  $\text{H}\alpha$ ,  $\text{H}\beta$ , and  $\text{H}\gamma$ , will have a broader line width than the forbidden lines, such as the oxygen [O II] and [O III] lines, and the nitrogen and neon [N II], [Ne III], and [Ne IV] lines. The broad line widths indicate FWHM velocities of  $10^3\text{--}10^4 \text{ km s}^{-1}$ .

By contrast, in Seyfert class 2 objects (the left panel of Figure 1.1), both forbidden lines and Balmer lines show the similar narrow line width. The narrow line widths indicate FWHM velocity in the range of  $200\text{--}900 \text{ km s}^{-1}$ . It is thought that the observational difference between Seyfert 1 and Seyfert 2 can be explained by the viewing angles with respect to an obscuring medium. We will explain this unified model in Section 1.1.2. Several intermediate objects have been observed, and are sorted into subclasses Seyfert 1.2, 1.5, 1.8, and 1.9 based on their Balmer characteristics, following the scheme introduced by Osterbrock (1977). However, we note that some Seyfert 2 galaxies ( $\sim 40\%$ ) have hidden broad emission lines, which are visible only in the polarized spectrum (Miller & Goodrich, 1990). The properties of hidden broad emission lines are very similar to those broad emission lines observed in typical Seyfert 1 nuclei.

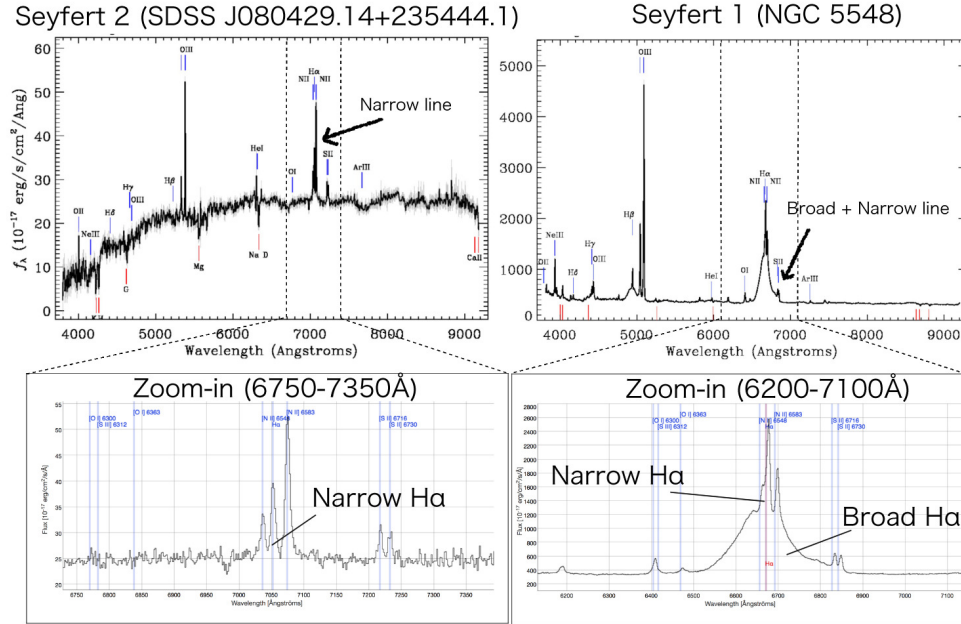


Figure 1.1: The optical spectrum of two Seyfert galaxies. Both are obtained from the Sloan Digital Sky Survey (SDSS) archive, the left panel is Seyfert 2 galaxy and the right panel is Seyfert 1 galaxy.

- **Radio:** Seyfert galaxies usually are radio-quiet objects but can still emit synchrotron radiation observed at radio wavelengths. The Very Long Baseline Array (VLBA) observations show that Seyfert galaxies with steep radio spectra have a strong tendency to exhibit radio jets at milliarcsecond scales, sometimes with considerable curvature in the jets (Ulvestad, 2003). They are very different to those powerful radio loud quasars (e.g. 3C 273) which have visible jets placed on either side of active nucleus with projected speeds in the sky plane of  $\sim 10c$  (Davis et al., 1991).

- **X-ray:** AGN taxonomy in the X-ray bands is similar to the optical, separating AGN into Type 1 and Type 2. In contrast to optical emission line classification, the X-ray classification is based on the intrinsic absorption measurement in the soft X-ray band ( $E \ll 5$  keV, corresponding to wavelength of  $\gg 0.24$  nm). Because X-ray emission comes from regions that are close to the central engine of the AGN, the intrinsic absorption may indicate either matter (e.g. neutral hydrogen) in the vicinity of the central engine, or other absorbers (e.g. gas and dust) along the observer's line of sight. The absorption is measured as column density of hydrogen  $N_H$  along the line of sight in atoms per cm<sup>2</sup>. Most X-ray column density measurements are generally in agreement with spectroscopic optical classifications, but not all. Seyfert 1 or Seyfert 1.2 usually have an inferred X-ray column density of  $\ll 10^{22}$  cm<sup>-2</sup>, while most, but again not all, Seyfert galaxies with X-ray column density of  $\gg 10^{22}$  cm<sup>-2</sup> are classified as optical Seyfert 1.8, 1.9 or 2. Although the neutral

hydrogen absorption occurs in soft X-ray band, the very hard X-ray band ( $E \gg 10$  keV) is a relatively good tracer of AGN activity, because the hard X-ray photons can penetrate through foreground obscuration. However, it is still biased against extremely obscured Compton-thick sources ( $N_H \geq 10^{25}$  cm $^{-2}$ ).

In addition to neutral hydrogen (cold gas) absorption, X-ray spectrum can also have ionized gas (warm gas) line absorption ("warm absorber"). At least 50% of the low resolution X-ray spectra of Seyfert 1 galaxies show the presence of a broad absorption feature at  $\sim 0.7$ – $0.8$  keV (e.g. NGC 3783, (Kaspi et al., 2002; Netzer et al., 2003; Krongold et al., 2003)). It ascribes to outflowing warm absorbers with velocities ranging from a few to several 100 km s $^{-1}$  and it is located between  $\sim 0.2$  pc and  $\sim 3$  pc from the ionizing, nuclear source (Maiolino & Risaliti, 2007).

- **Infrared/(sub)millimeter:** In principle, most infrared emissions are thought to be due to thermal radiation of dust grains, the spectral slope of which is described in terms of equivalent temperatures. The far-infrared emission is dominated by host galaxy cold dust (at kiloparsec, "kpc", scales) with a temperature of  $\sim 30$ K (e.g. Schweitzer et al. (2006)). On the other hand, at mid-infrared and near-infrared wavelengths, there is much information related to the AGN. The power-law-like continuum is likely a result of thermal emission from dust heated close to sublimation temperature by the optical/ultraviolet continuum from the central engine (Edelson & Malkan, 1986; Alonso-Herrero et al., 2001). This hot dust component, often referred to as a "torus" (see Section 1.1.2 and Figure 1.2), can obscure the direct line of sight to the nucleus, leading to distinct observational characteristics across different wavelengths. The dusty torus is a gas-rich component, outer extent typically thought to be a few pc to few tens of pc; but it is poorly constrained in models and observations (Nenkova et al., 2008; Hönig & Kishimoto, 2010).

Table 1.1 summarizes the observed properties of Seyfert nuclei across different wavelengths, which allow us to construct a simple AGN unified model to explain them.

### 1.1.2 Unification

The unification idea is searching for a simple model (Antonucci, 1993), which is capable of describing all observed phenomena with a minimum number of parameters. By measuring the correlations, either positive or negative, between various observed properties, we can study what kind of physics might be operating behind the scenes. The AGN unified model is proposed to explain different observational classes and properties of AGN at different wavelengths which we have previously summarized in Section 1.1.1. The currently favoured unified model is the "orientation of AGN system", meaning all other observed differences would be due to orientation effects (this unification followed on radio unification, e.g. Urry & Padovani (1995); Padovani & Urry (1992)). In this scenario, all Seyfert galaxies intrinsically have the same nuclei.

The AGN unified model sketch is presented in Figure 1.2. The central engine is a supermassive black hole (SMBH mass in the range of  $10^6$ - $10^{10}$   $M_\odot$ ). It is surrounded by a geometrically thin accretion disk (generating non-thermal radiation at UV/optical

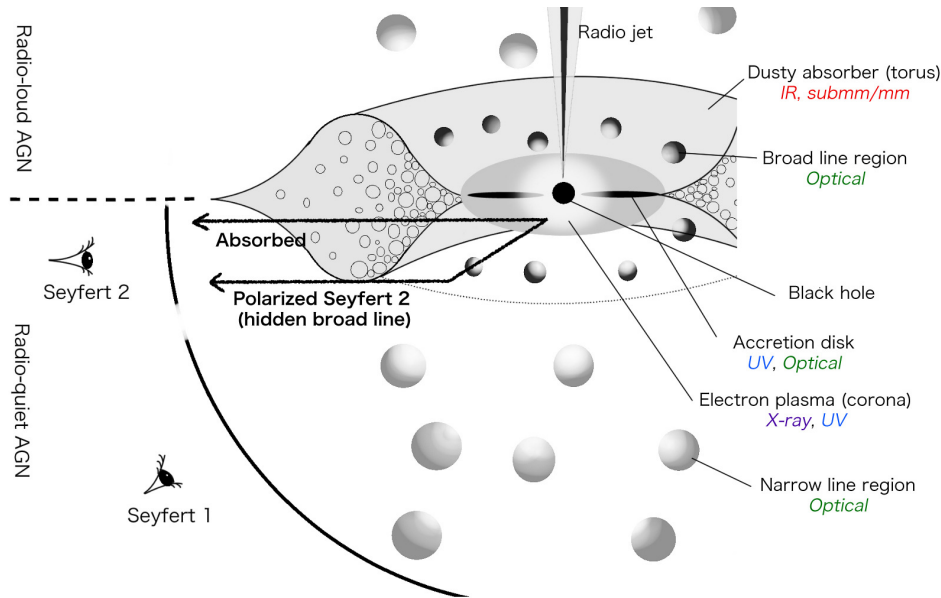


Figure 1.2: The schematic representation of our understanding of the AGN phenomenon in the AGN unified model, especially for Seyfert-level AGN. This version is modified based on Figure 4.16 of Beckmann & Shrader (2012).

wavelengths) which is composed of diffuse material in orbital motion. The black hole and the accretion disk are both embedded inside the electron plasma (named the corona), which is thought to be an origin of AGN X-ray emission. The outer region of the AGN unified model is the obscuring material composed of gas and dust (often called the “torus”), which emits infrared continuum emission. Broad line emission and narrow line emission come from the broad line region (BLR) and narrow line region (NLR), respectively. The former one is distributed inside the torus structure, whereas the NLR is the most extensive part of AGN. In some cases (e.g. NGC 5252 in Unger et al. (1987)), the narrow line emission extends over several kpc from the central black hole. The BLR is composed of dense dust free clouds between the accretion disk and torus inner edge (Davies et al., 2015). While the NLR is any part of the host galaxy illuminated and photo-ionized by the AGN, and can also refer to an outflowing wind driven by the AGN.

Many studies support the orientation dependence; but also suggest this structure is more complex (Elitzur, 2012). The unified model proposes that in Seyfert 1, the observer has a direct view to the nucleus, the spectra of which display broad and narrow emission lines superimposed on non-thermal optical continuum, together with unabsorbed X-ray spectrum. In contrast, the nucleus in Seyfert 2 is observed through an obscuring structure, which is a geometrically and optically thick torus surrounding the central engine of AGN on scale of inner edge  $< 1$  pc, outer edge several parsecs or more, size is luminosity dependent (refer to Section 1.2.4 of Netzer (2015)). It leads to the absence of broad emission lines in Seyfert 2 nucleus, as well as the high column density of neutral hydrogen in X-ray spectra. The AGN unified model implies that broad emission lines in Seyfert 2 nucleus would be

hidden, compared to Seyfert 1 nucleus observed in face-on direction.

The decisive evidence to support the AGN unified model is a proof given by Antonucci & Miller (1985), who showed that the Balmer emission lines in the Seyfert 2 NGC 1068 are broad when the AGN is observed in polarized light at optical wavelengths. In addition, they showed that the non-thermal continuum emission of the central engine also has some level of polarization as the Balmer emission lines. Many polarized Seyfert 2 galaxies with hidden broad lines have been discovered by subsequent spectropolarimetric observations.

Although the unified model can successfully explain the observed properties of Seyfert nuclei, several physical and observational questions are still required to study in further details. How does the torus form? What is the mechanism to support its geometrical structure? These questions will be discussed in Chapter 2.

### 1.1.3 Characterizing the central SMBH

The AGN can be characterized by two key parameters: SMBH mass and Eddington ratio. For nearby Seyfert galaxies, precise SMBH mass measurements can be derived using water megamaser spots in a Keplerian circumnuclear disk (e.g. NGC 4258 in Herrnstein et al. (1999)). Such megamasers are very close to the dynamical centre of galaxy and describe a disk with a Keplerian rotation curve within 0.1 pc from the central SMBH. The Eddington ratio is the ratio of an AGN's bolometric luminosity to the Eddington luminosity ( $L_{Edd}$ ), in which the latter term is the maximum luminosity of an AGN that will not blow away its accretion disk via its own radiation pressure (i.e. assuming spherical inflow balances spherical outflow). The equation is expressed as the following:

$$L_{Edd} = \frac{4\pi G M_{BH} c m_p}{\sigma_T} = 1.26 \times 10^{38} (M_{BH}/M_{\odot}) \text{ erg s}^{-1} \quad (1.1)$$

where  $m_p$  is the mass of a proton and  $\sigma_T$  is the Thomson scattering cross section for the electron. The Eddington ratio describes the efficiency with which gravitational potential energy can be converted into emergent radiative energy. Nearby Seyferts have Eddington ratios in the range of  $10^{-2}$ -0.2. Higher Eddington ratios correspond to more efficient in generating radiation, and may be a hint of 'AGN feedback' toward host galaxy.

Although the AGN is powerful, the timescale of AGN activity with respect to the age of Universe is short. Greene & Ho (2007) shows BHs with masses  $\sim 10^7 M_{\odot}$  living in  $\sim 10^{10} M_{\odot}$  spheroids are active  $\sim 0.4\%$  of the time. This suggests, that the timescale of AGN activity is  $0.004 \times 10^{10} \sim 10^8$  years: SMBHs are mostly in a quiescent state. To trigger AGN, there must be some material falling toward the central SMBH. The potential Seyfert-level AGN fuelling mechanisms are galaxy interactions, gas streamers, and secular process (bar instability). Several questions arise in this respect. Where such accreting material come from? Is there any material associate to recent star formation around the nuclear region? In order to elaborate answers to those we use a sample of AGN and a sample of matched inactive galaxies (normal galaxy, where the central SMBH is in a quiescent state). Any photometric and kinematic difference between these two samples

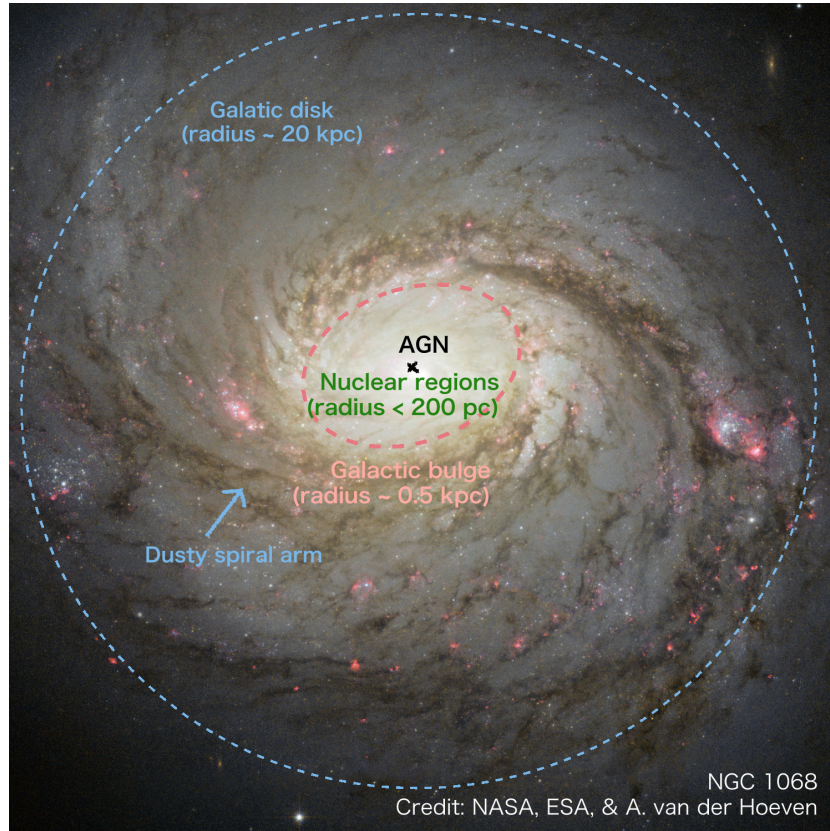


Figure 1.3: The host galaxy structures of the nearby Seyfert 2 NGC 1068. The background image is obtained from the Hubble Space Telescope (HST). The galactic disk is the plane which contains the dusty spiral arms (sometimes together with a large-scale bar). The galactic bulge has a 2–3 kpc radius across the whole galaxy and comprises randomly orbiting stars. The AGN is in the centre of the galaxy, labeled as a black cross. In this thesis, we focus on the nuclear regions on radial scales out to a few hundred pc from the centre.

provide further hints regarding whether nuclear star formation links to AGN activity. The corresponding analysis will present in Chapter 3.

## 1.2 Importance of host galaxy nuclear regions

One of the most influential discoveries is a tight correlation between the mass of the SMBH and the stellar velocity dispersion ( $\sigma$ ) of the bulge or spheroidal (e.g. elliptical galaxy) component of the host galaxy (named the "M- $\sigma$  relation"). Together with similar correlations of bulge luminosity and mass, these lead to the widespread belief that the SMBH and its host galaxy bulge coevolve by regulating each other's growth (Kormendy & Ho, 2013). The host galaxy structures are illustrated in Figure 1.3. As shown by Fabian (2010), this globally positive correlation can be described when assuming that the AGN core is operating close

to the Eddington limit. The radiation pressure will drive out the gas, the mass of which is a fraction  $f$  of the bulge mass  $M_{bulge}$ , which we assume to be spherical with a radius  $R$ . In a steady mode, the force from the time-average luminosity  $L_{Edd}/c$  is equal to the gravitational force, keeping the mass  $f M_{bulge}$  just outside the bulge at the radius  $R$ .

$$\frac{L_{Edd}}{c} = \frac{G M_{bulge} f M_{bulge}}{R^2} \quad (1.2)$$

The Eddington luminosity as in Equation 1.1 is included on the left hand side of the Equation 1.2.

Assuming that the bulge is an isothermal sphere, the mass inside  $R$  is a function of the velocity dispersion  $\sigma$ :  $M(<R) = 2 R \sigma^2 / G$  and thus

$$\frac{M_{bulge}}{R} = \frac{2 \sigma^2}{G} \quad (1.3)$$

Combining Equation 1.2 and Equation 1.3, the correlation of the SMBH mass and stellar velocity dispersion can be written as:

$$M_{bulge} = \frac{f \sigma_T}{\pi G^2 m_p} \sigma^4 \quad (1.4)$$

In order to clarify our understanding of the coevolution between SMBH and host galaxy, it is crucial to study the ambient SMBH environment. The nuclear regions can be a gas reservoir to fuel the SMBH and preserve any evidence of recent feedback from the central SMBH. In this thesis, the nuclear regions refer to a distance out to a few hundred pc from the central SMBH; all of this radial range is inside the bulge effective radius that encompasses half of the light of the bulge component. The observed phenomena in the nuclear regions are briefly introduced below.

### Nuclear star formation

Most studies focus on the origin of accreting material rather than studying the fuelling AGN mechanism. Several observations show that the gas is fairly concentrated on the centre (Lindt-Krieg et al., 2008). Once the gas is cooling then it can form stars. Numerous observations have shown recently formed young stars are often found in the nuclear regions of nearby AGNs, suggesting a connection (causal or non causal) between AGN activity and star formation (Storchi-Bergmann et al., 2001; Cid Fernandes et al., 2004; Esquej et al., 2014; Davies et al., 2007). Numerical simulations also indicate a time delay between star formation and AGN activity, implying the star forming region may provide the fuel to the central SMBH via winds of massive stars and supernovae (Hopkins, 2012; Hopkins et al., 2016).

### Nuclear inflows

The idea is that dynamically driven inflow that we discuss here brings gas in from a few hundred parsecs to a few tens of parsecs where one sees the nuclear star formation discussed

above. In several nearby Seyfert galaxies, gas flows inward the central SMBH has been found along nuclear structures such as spiral arms (NGC 6951 in Storchi-Bergmann et al. (2007), NGC 1097 in Davies et al. (2009)), bars (NGC 3227 in Davies et al. (2014)) and dust lanes (NGC 3081 in Schnorr-Müller et al. (2016)) from optical and near-infrared observations. In general, the inflowing gas velocity (non-circular motion) is in a range of 50–100 km s<sup>-1</sup>. Together with the measurement of gas column density, we then calculate the gas inflow rate, which is in a wide range of 0.2–2 M<sub>⊙</sub> yr<sup>-1</sup>.

### Nuclear AGN-driven outflows

The molecular gas in massive and powerful quasar, sometimes shows a broad wing with a velocity of  $\sim 500\text{--}1000\text{ km s}^{-1}$  on the kpc (galaxy-wide) scale, as a direct evidence of AGN-drive outflows (e.g. Mrk 231 in Feruglio et al. (2010)). By contrast, Seyfert-level AGN-driven outflowing gas only has been found near the nucleus, with a velocity of 100–400 km s<sup>-1</sup> (Combes et al., 2013; Schnorr-Müller et al., 2017). This outflow velocity is probably sufficient to exceed the escape velocity of the bulge (using NGC 5194 for example,  $v_{bulge}^{esc} = \sqrt{2GM_{bulge}/5R_{bulge}^{eff}} \sim 160\text{ km s}^{-1}$ ), but not enough to overcome the whole galaxy potential. For those outflowing gas with lower velocities, they will be stalled inside the bulge and be partially recirculated in a process similar to a galactic fountain, which increases the turbulence in the gas (Querejeta et al., 2016).

## 1.3 The kinematic tracers in the nuclear regions

In order to study the observed phenomena in the nuclear regions, several observable tracers are needed to monitor the kinematics close to the central SMBH. The kinematic tracers can be emission lines or absorption lines of gas clouds or stars at different wavelengths. In this thesis, we focus on two wavelength regimes: millimetre at  $\sim 3\text{mm}$  and near-infrared at  $\sim 1\text{--}3\mu\text{m}$ . To trace the bulk of the cold and dense molecular clouds that co-exist with the dusty torus, we observe several molecular emissions using the WideX correlator at the Plateau de Bure interferometer. In addition, for near-infrared (near-IR) observations, we study the system kinematics by tracing integrated stellar absorptions of stars inside the bulge component of the host galaxy. We obtained the near-infrared data cubes with the SINFONI instrument on the Very Large Telescope (VLT).

### 1.3.1 Dense molecular gas

The most abundant molecule in the interstellar medium (ISM) is H<sub>2</sub>. It has no permanent dipole moment, and therefore there is no electric dipole transition. However, electric quadrupole transitions may still occur. For example, H<sub>2</sub> presents rotation-vibrational (ro-vibrational) transitions at 2.12 $\mu\text{m}$  with the  $v = 1\text{--}0$  S(1) line, i.e., the transition from  $v = 1$  to  $v = 0$  and from  $J = 3$  to  $J = 1$ . Nevertheless, it is difficult to observe H<sub>2</sub> directly because

of its excitation mechanisms, even the lowest ro-vibrational level requires temperatures of more than 1000 K.

The rotational lines of the abundant CO molecule ( $H_2/CO = 10^{4-5}$ ) are usually used in the literature to trace cool and dense molecular clouds (critical density  $\sim 4.2 \times 10^3 \text{ cm}^{-3}$  for CO(1-0), with  $J = 1$  to  $J = 0$ ). However, molecular clouds usually are optically thick in this transition, and therefore the local density of emission line photons is not representative for the density of photons from the background radiation field (i.e. radiative trapping).

We choose the optically thin HCN( $J = 1$  to  $J = 0$ ) at 88.6 GHz and HCO+( $J = 1$  to  $J = 0$ ) at 89.2 GHz as target molecules for interferometer observations. The energy of the first level for the two targeted molecules corresponds to  $\sim 4$  Kelvin, and both have critical densities  $\geq 10^5 \text{ cm}^{-3}$ . Therefore these molecular transitions can properly trace the dense and cool molecular clouds, extending from the central AGN out to a few hundred pc radius.

### 1.3.2 Stellar absorption

The kinematics of the bulge component of the host galaxy can be traced by the integrated motions of individual stars. These motions are imprinted in the molecular absorption lines in stellar atmospheres. A triplet of three calcium absorption lines at  $\sim 0.85 \mu\text{m}$  (Ca II triplet lines) is most prominently observed in spectral type of G, M, and K stars, and is widely used in the literature to extract the bulge kinematics. In this thesis, we use the stellar absorption lines at near-IR wavelengths which are relatively insensitive to dust extinction. Stellar absorption lines covering the wavelengths 2.28 to 2.40  $\mu\text{m}$  are the main parts of the first overtone bands of the CO molecule. These lines are the ro-vibrational transitions ( $\Delta v = 2$ ) and occur near  $J = 50$ . The CO ro-vibrational spectrum has bands in the near-IR which are not too seriously affected by telluric absorption. The CO( $v = 2$  to  $v = 0$ ) at 2.29  $\mu\text{m}$ , CO( $v = 3$  to  $v = 1$ ) at 2.32  $\mu\text{m}$ , CO( $v = 4$  to  $v = 2$ ) at 2.35  $\mu\text{m}$ , and CO( $v = 5$  to  $v = 3$ ) at 2.38  $\mu\text{m}$ , are the targeted bandheads in our near-IR observations.

## 1.4 Techniques to provide high resolution images

The central SMBH is expected to dominate the local gravity and to lead to observable dynamical consequences only inside a sphere-of-influence radius of  $R_{infl} \equiv G M_{BH}/\sigma^2$ . Nearby spiral galaxies have  $M_{BH} \sim 10^{6.5}$  and their host galaxy velocity dispersions are  $\sigma \sim 150 \text{ km s}^{-1}$  in average, corresponding to a sphere of influence with radius of 0.6 pc. At a distance of 1–40 Mpc for nearby galaxies, the angular size of the sphere-of-influence is  $< 0.01''$ . To approach the sphere-of-influence regions, we use an interferometer (several antennas placed apart to work simultaneously) to achieve higher spatial resolution than for single antennas at millimeter wavelengths. On the other hand, at near-IR wavelengths, we use adaptive optics technology to improve the telescope performance by removing effects of atmospheric distortion.

### 1.4.1 Plateau de Bure Interferometer (PdBI)

The resolution of a telescope is described as an Airy disk with a certain radius:  $\theta \sim 1.22 \frac{\lambda}{D}$ , where  $\lambda$  is the wavelength and  $D$  is the diameter of the telescope. For a 0.2 meter optical telescope, the maximum spatial resolution that can be achieved is  $0.8''$  at  $0.656\mu\text{m}$ . In contrast, at radio wavelength of 3mm, a similar spatial resolution can only be achieved with a  $\sim 950$  meter telescope. Building a kilometer-size dish antenna as a radio telescope is difficult. An interferometer, in which several antennas work together as a single telescope to provide higher resolution images of astronomical objects, is a better solution.

The basic interferometer is a pair of a radio antennas whose voltage outputs are correlated, but one output signal is lagged by the geometric delay (time delay in arrival of a wavefront at two different locations) to the other output signal. A correlator converts the output signals into a complex visibility function, which is usually expressed as a function of the parameters  $u$  and  $v$  (in meters). Note that  $u$  and  $v$  depend on the hour angle, so as the Earth rotates and the source moves across the sky, the observation samples have different  $u$  and  $v$  at different times. With sufficient  $uv$  data, one can reconstruct a image by iteratively fitting predictive models and checking the residuals. Many antennas and sufficient observing times improve the image reconstruction.

In this thesis, we use the Plateau de Bure interferometer (PdBI) to observe dense molecular clouds in the nuclear regions of nearby Seyfert galaxies. The PdBI is an observatory operated by the Institut de radioastronomie millimétrique (IRAM), and it is located in the Hautes-Alpes in France. It has six antennas which function as a single radio telescope. It can achieve a maximum diameter of 760 meters and provide the  $\sim 1''$  spatial resolution that is required for the study of nuclear regions. The PdBI is now upgraded to the Northern Extended Millimeter Array (NOEMA), which currently consists of nine antennas, each one of which is 15 meters in diameter.

### 1.4.2 Spectrograph for INtegral Field Observations in the Near Infrared (SINFONI)

With the advent of large telescopes and improved instrumentations, an integral field unit (IFU) allows us to obtain a spectrum for each pixel within the entire 2D field of view. However, the ground-base optical/near-IR telescopes are limited by atmospheric distortions. When light enters the Earth's atmosphere, the turbulences induced by different temperature layers and different wind speeds can distort a beam of light. Adaptive optics (AO) is a technology which helps to partially overcome these effects. Given a guide star (which can be a bright natural guide star close to the scientific targets, or a laser guide star) used as a wavefront reference, the atmospheric distortions can be measured and corrected by a deformable mirror (e.g. a rapidly moving tip-tilt mirror). An IFU data cube with an AO correction can achieve a spatial resolution of  $0.05''$ - $0.1''$ , while the observations without an AO correction (seeing limited) are of the order of  $\sim 1''$ . In this thesis, we use a near-IR IFU, namely SINFONI with AO mode on the VLT, as it allows us to measure the stellar kinematics at location closely approaching toward the centre of the galaxy.

## 1.5 The outline of this work

This thesis is described in the following:

- Chapter 1 reviews the basic properties of AGN across different wavelengths. The global correlations between AGNs and their host galaxies suggest that the central SMBH and the bulge component grow with each other by radiative regulations. To better understand the relevant physical processes, we require high resolution images approaching to the sphere-of-influence radius. We use a millimeter interferometer to trace the distribution of dense molecular gas and use a near-IR IFU with AO mode to study the kinematics of stars. We briefly introduce the principle of related techniques that have been applied in this study.

- Chapter 2 presents 3mm interferometer data from the IRAM PdBI, which spatially resolves the HCN(1-0) and HCO+(1-0) molecular lines in the central few arcsec of nearby Seyfert galaxies. In this chapter, we focus on the questions: What is the geometric structure of the dense molecular clouds? What are the physical properties of the dense molecular clouds around AGN?

- Chapter 3 presents near-IR IFU data from SINFONI in AO mode at the VLT. In a sample of local 14-195 keV selected AGNs and inactive galaxies, matched by their host galaxy properties, we study the spatially resolved stellar absorption features of the CO molecule within the inner 1.5'' radius. In this Chapter, we focus on the questions: Is there any difference in kinematics and photometry between active and inactive galaxies? Is there any evidence that recent star formation is associated to the AGN fuelling process?

- Chapter 4 presents an unexpected asymmetry in the stellar velocity dispersion field along the major axis for AGNs. We apply two distinct methods to quantify the asymmetry and discuss various physical interpretations for this phenomenon.



# Chapter 2

## Thick Disks, and an Outflow, of Dense Gas in the Nuclei of Nearby Seyfert Galaxies

*This chapter is a reprint of*

*Ming-Yi Lin, R.I. Davies, L. Burtscher, A. Contursi, R. Genzel, E. González-Alfonso, J. Graciá-Carpio, A. Janssen, D. Lutz, G. Orban de Xivry, D. Rosario, A. Schnorr-Müller, A. Sternberg, E. Sturm, L. Tacconi  
MNRAS, 2016, 458, 1375-1392*

### 2.1 Introduction

The standard unification scheme for active galactic nucleus (AGN) proposes that the intrinsic properties of AGN are similar, and the disparity of observational properties arises from the different viewing angles with respect to an obscuring medium, resulting in type 1 and type 2 AGNs (Antonucci, 1993; Urry & Padovani, 1995). The reality may be more complex than this simple picture suggests (Netzer, 2015) although there is general agreement that the obscuring medium of gas and dust is a geometrically and optically thick toroidal structure (perhaps including an outflowing wind, e.g. Elitzur & Shlosman 2006) surrounding the AGN accretion disk, with its inner edge at the dust sublimation radius. Numerous observations confirm that there is dust at temperatures in the range 1000–1500 K (e.g. see Burtscher et al. 2015 and references therein). And a variety of models for smooth (Pier & Krolik, 1992; Granato & Danese, 1994; Granato et al., 1997; Schartmann et al., 2005; Fritz et al., 2006) and clumpy (Krolik & Begelman, 1988; Nenkova et al., 2002; Hönig et al., 2006; Schartmann et al., 2008, 2014) media have been constructed to reproduce the spectral energy distribution (SED) at infrared wavelengths as well as the silicate feature at  $\sim 10\mu\text{m}$  (Schweitzer et al., 2008). However, a number of difficulties remain when applying these models to observations. Feltre et al. (2012) point out that in addition to the parameters describing the physical geometry, the assumptions built into the models can have a

major impact on the resulting SED. And in the best studied cases where interferometry can spatially resolve some of the structure, a component that is aligned along a direction consistent with an outflow appears to be responsible for much of the mid-infrared continuum (Tristram et al., 2014). Finally, in the context of the observations we present here, the outer edge of the torus is poorly defined for the majority of these models, because beyond a few tens of parsecs it contributes relatively little to the warm dust continuum against which the models are tested.

On radial scales of tens to a hundred parsecs, it is not clear whether one should still refer to the gas and dust structure as a torus or a (circum-)nuclear molecular disk. There have been claims that even on these scales the molecular disk is thick enough to have an impact on obscuration towards the AGN and so contributes to the observed difference between type 1 and type 2 AGN (Hicks et al., 2009; Sani et al., 2012); and hydrodynamical simulations suggest that turbulence injected via supernova from recent or on-going star formation can puff up the disk to heights of  $\sim 10$  pc (Wada et al., 2009; Wada, 2012). Spatially resolving molecular tracers on these scales in nearby AGN has become possible during the last decade, through the use of adaptive optics systems operating at near-infrared wavelengths and interferometers working in the millimetre regime.

Hicks et al. (2009) observed the  $\sim 2000$  K  $H_2$  via the  $2.12 \mu\text{m}$  1-0S(1) line. In most cases the velocity dispersion ( $\sigma_{H_2}$ ) of this line exceeded its rotational velocity ( $v$ ) on radial scales of  $\sim 50$  pc. Their conclusion was that the disk is relatively thick. The  $2.12 \mu\text{m}$  line traces a small excited fraction of the  $H_2$  mass that might have peculiar kinematics, so that kinematics from a tracer of the bulk of the molecular gas is desirable. Using the  $3 \text{ mm HCN}$  (1-0) line, Sani et al. (2012) modeled the emission as a rotating disk, and also found that a large intrinsic velocity dispersion ( $\sigma_{HCN}$ ) was required to match the observations. Intriguingly, these results together,  $\sigma_{H_2} \sim 50\text{--}100 \text{ km s}^{-1}$  and  $\sigma_{HCN} \sim 20\text{--}40 \text{ km s}^{-1}$ , suggest that the molecular gas is stratified with the warmest gas being the most turbulent and reaching to larger scale heights while the denser clouds remain closer to the disk plane. Although several observations (e.g. Hicks et al. 2009 and Müller-Sánchez et al. 2013) have confirmed the presence of thick disks with  $\sigma/v \sim 0.4$  on radial scales of  $\sim 50$  pc in some objects, it is not clear how the kinetic energy is continuously supplied in order to maintain the vertical structure of a rotating disk. One plausible explanation is that nuclear star formation can provide the necessary energy. Stellar radiation pressure (Thompson et al., 2005) is one option if there are sufficient OB stars and the ISM is optically thick. However, while some observations are consistent with on-going star formation (Esquej et al., 2014; Riffel et al., 2009), others point more towards post-starburst populations (Cid Fernandes et al., 2004; Davies et al., 2007), and in some cases there is clear evidence that there cannot be on-going star formation in the central tens of parsecs (Hicks et al., 2013). Alternatively, supernova explosions, associated even with a very modest star formation rate, are able to generate sufficient turbulence in the disk to yield  $\sigma \sim 20 \text{ km s}^{-1}$  to radii of  $25$  pc (Wada & Norman, 2002; Wada et al., 2009). A third possibility is that the gas flows induced by disk instabilities toward inner radii can also maintain a thick disk (Hopkins et al., 2012). Vollmer et al. (2008) also argued that the energy from inflowing gas could in principle be used to thicken the central disk.

The main purpose of this work is to model the intrinsic geometry (i.e. radial and height scales) of the molecular disk in the central  $\sim 100$  pc around AGN, by using high resolution HCN (1-0) and HCO<sup>+</sup> (1-0) observations. In addition, we use Large Velocity Gradient (LVG) calculations for molecular line ratios to constrain the cloud properties in one of the objects, NGC 6951.

The HCN and HCO<sup>+</sup> molecules are ideal indicators of dense gas, since the higher dipole moments of their 1-0 rotational transitions can trace  $\sim 100$ –500 times denser gas than the same rotational transitions of the CO molecule, and are sensitive to gas at  $n_{H_2} \sim 10^{4-5} \text{ cm}^{-3}$  (Papadopoulos, 2007). These molecules have been successfully observed not only in dense star-forming regions but also in a number of Seyfert galaxies (Krips et al., 2008; Kohno, 2005; Kohno et al., 2008; Sani et al., 2012), although typically at resolutions of 5–20 arcsec. In the nuclear region of Seyfert galaxies, HCN (1-0) and HCO<sup>+</sup> (1-0) can be excited either by UV light from the accretion disk or X-ray radiation from the corona (Sternberg & Dalgarno, 1995; Maloney et al., 1996; Lepp & Dalgarno, 1996; Meijerink & Spaans, 2005; Boger & Sternberg, 2005; Meijerink et al., 2007, and the references therein).

This paper is organized as follows. The HCN (1-0) and HCO<sup>+</sup> (1-0) observations of NGC 3079, NGC 6764, and NGC 5033 are described in Section 2.2. We present the observed molecular gas distribution and kinematics for each galaxy in Section 2.3. We apply a simple dynamical model to the emission lines in Section 2.4, and in section 2.5 use the H<sup>13</sup>CN (1-0) absorption to estimate the column density of the disk in NGC 3079. Section 2.6 brings in data from the literature to explore the relation between HCN luminosity and dynamical mass for a sample of 8 objects with high spatial resolution HCN observations. Finally, Section 2.7 looks more closely at the cloud properties for one specific object NGC 6951 where data for suitable transitions are available. We summarize our conclusions in Section 2.8.

Table 2.1: Summary of IRAM-PdBI observations for the 3 Seyfert galaxies.

(1) Source name; (2) Beam size; (3) Beam position angle; (4) Channel width; (5) noise per beam; (6) Distance; (7) Physical scale of 1".

(1) Source	(2) Beam size	(3) P.A. (degree)	(4) Channel resolution (km s <sup>-1</sup> )	(5) Noise (mJy beam <sup>-1</sup> ch <sup>-1</sup> )	(6) Distance (Mpc)	(7) scale (pc/")
NGC 3079	1.17" × 0.94"	167	17.1	0.37	20	85
NGC 6764	1.16" × 0.78"	13	34.4	0.29	32	150
NGC 5033	1.13" × 0.83"	38	34.2	0.31	19	73

## 2.2 Observations

We used the six 15-m antennas of the IRAM Plateau de Bure interferometer (PdBI) to observe NGC 3079, NGC 6764, and NGC 5033 at 88 GHz (3 mm) with the WideX correlator in the extended A configuration. The basic calibration steps of three galaxies were done with the CLIC software. The observations for the individual galaxies are described below and summarised in Table 2.1.

Observations of NGC 3079 (systemic velocity  $1147 \text{ km s}^{-1}$  and inclination  $77^\circ$ , Koda et al. 2002) were carried out on 19 January 2011 for programme UD8A. The receiver band was centered at 87.55 GHz with its 3.6 GHz bandwidth covered all features from  $\text{HCO}^+$  (1-0) at 89.2 GHz to  $\text{H}^{13}\text{CN}$  (1-0) at 86.3 GHz (rest frequencies). During the 5.5 hr track the average antenna efficiency was 22.6 Jy/K, and the precipitable water vapour (pww) improved during the track from 2–4 mm to  $< 2$  mm. The calibrators include 3C273, 0923+392, 0954+556, and MWC349. After data reduction, the synthesised beam at 89 GHz was  $1.2'' \times 0.9''$  at position angle (PA) 167 deg. The data were binned to a spectral resolution of 5 MHz corresponding to a channel width of  $17 \text{ km s}^{-1}$ , yielding a root mean square uncertainty of 0.37 mJy/beam. This was chosen in order to balance signal-to-noise with high spectral resolution since some of the absorption features are much narrower than the emission lines. Images of the channels were reconstructed with a pixel size of  $0.2''$ . We adopt a distance to NGC 3079 of 19.7 Mpc, for which  $1''$  corresponds to 85 pc.

NGC 6764 was also observed on 19 January 2011, after NGC 3079, with the receiver band centered at 87.15 GHz. This setting was based on the systemic velocity of  $2416 \text{ km s}^{-1}$  used by Hota & Saikia (2006), who found deep HI absorption on the location of the nucleus at a velocity of  $2426 \text{ km s}^{-1}$  consistent with that velocity. However, the profiles of both the HCN (1-0) and  $\text{HCO}^+$  (1-0) lines in our data are centered at  $2468 \text{ km s}^{-1}$  (each differing by only  $10 \text{ km s}^{-1}$  from that mean). This implies that the HI may be outflowing, a phenomenon that has been observed in a number of galaxies (see Morganti 2012 for a review), for example in the Seyfert IC 5063 the HI absorption is blue-shifted with respect to the HI emission with velocities comparable to a blue wing in the CO (2-1) line (Morganti et al., 2007, 2015). In our analysis we use  $2468 \text{ km s}^{-1}$  as the systemic velocity for NGC 6764. We also adopt an inclination of  $62^\circ$  based on CO (1-0) kinematics (Leon et al., 2007). During the 4.9 hr track the average antenna efficiency was 22.9 Jy/K, and the pww was  $< 1$  mm. The calibrators include MWC349, 1954+513, 1739+522, 1749+096, and 1823+568. The synthesised beam at 89 GHz in the processed data was  $1.2'' \times 0.8''$  at a PA of 13 deg. The data were spectrally binned to 10 MHz, corresponding to a channel width of  $34 \text{ km s}^{-1}$  and a root mean square uncertainty of 0.29 mJy/beam. The channel binning is coarser than for NGC 3079 but sufficient to sample the velocity width of the emission lines. In order to fit disk models, the data were converted to an image plane with a pixel size of  $0.3''$ . We adopt a distance to NGC 6764 of 31.7 Mpc, for which  $1''$  corresponds to 150 pc.

Observations of NGC 5033 (systemic velocity  $875 \text{ km s}^{-1}$ , Huchra et al. 1995; inclination  $68^\circ$ , Thean et al. 1997 and Kohno et al. 2003) were conducted over two nights on 26 and 28 January 2011, with tracks of 3.1 hrs and 3.9 hrs respectively. The receiver band was centered at 87.60 GHz. The average antenna efficiency of 22.7 Jy/K, with pww  $<$

Table 2.2: Summary of the continuum properties for the 3 targets:

(1) Source name; (2) Flux density; (3) The observed FWHM of the major and minor axes; (4) Position angle (east of north).

(1) Source	(2) Flux density (mJy)	(3) Major $\times$ Minor axis (arcsec <sup>2</sup> )	(4) P.A. ( $^{\circ}$ )
NGC 3079	$27.8 \pm 0.15$	$1.19 \pm 0.01 \times 1.06 \pm 0.01$	$176 \pm 1$
NGC 6764	$0.6 \pm 0.06$	$1.04 \pm 0.05 \times 0.82 \pm 0.04$	$8 \pm 2$
NGC 5033	$0.7 \pm 0.08$	$1.01 \pm 0.04 \times 0.79 \pm 0.03$	$41 \pm 2$

1 mm on the first night and  $< 3$  mm on the second night except near the end when it increased slightly. The calibrators include 3C273, MWC349, 1308+326, and 0355+508. After data reduction, the synthesised beam size at 89 GHz was  $1.1'' \times 0.8''$  at a PA of 38 deg. The reconstructed data for NGC 5033 share the same spectral binning and pixel size as NGC 6764, and have a root mean square uncertainty of 0.31 mJy/beam. We adopt a distance to NGC 5033 of 18.7 Mpc, for which  $1''$  corresponds to 73 pc.

We also make use of HCN (1-0) data for NGC 7469 presented in Davies et al. (2004), which have a beam size of  $2.0''$ . We adopt a distance of 58 Mpc and an inclination of  $45^{\circ}$ .

## 2.3 Gas distribution and kinematics

We begin this section by describing the general properties of the three galaxies, and then present the details for each individual source in the following subsections. HCN (1-0) at 88.63 GHz, and HCO<sup>+</sup> (1-0) at 89.19 GHz were detected in all galaxies.

In every case, the 3 mm continuum (spectrally integrated over channels that are free from molecular transitions) is seen as a single compact source. Since the major and minor axes, and the position angle, are very close to those of the beam, the continuum appears to be spatially unresolved. The flux density and morphology of the continuum sources are derived from line-free regions of the spectrum, and are given in Table 2.2.

In contrast, the HCN (1-0) and HCO<sup>+</sup> (1-0) emission line morphologies are spatially extended, although by not more than a few arcsec. We define the centre from the continuum image, and extract an integrated spectrum in a  $3''$  diameter aperture around that. The flux density of the emission lines is derived from this by summing over all channels across the spectral line profile. It is important to note that for NGC 3079, HCN (1-0) and HCO<sup>+</sup> (1-0) both show a clear P-Cygni shape, with absorption cutting through the emission line profile. For both NGC 6764 and NGC 5033, the lines are seen in emission only. As for the continuum, the morphology of the molecular lines is quantified by fitting a two-dimensional Gaussian function to the line map. In addition, we have measured the centers of the emission summed over red channels and blue channels separately (the velocity ranges are from line centre to  $\pm 350$ – $480$  km s<sup>-1</sup> depending on the line and object; specific ranges are

given in the following subsections), in order to derive their relative separation and position angle. The observed properties of the molecular emission lines are summarized in Table 2.3.

Table 2.3: The observed properties of molecular emission for 3 targets:

(1) Source name; (2) Molecule; (3) Flux<sup>a</sup>; (4) Observed FWHM of major and minor axes; (5) Position angle (east of north); (6) Separation between centers of red and blue channel maps; (7) Position angle between centers of the red and blue channel maps; (8) Spectral FWHM of line (3'' aperture).

(1) Source	(2) Line	(3) Flux (Jy km s <sup>-1</sup> )	(4) Major × minor axis (arcsec <sup>2</sup> )	(5) PA (°)	(6) b/r sep. (arcsec)	(7) PA <sub>b/r</sub> (°)	(8) Line width (km s <sup>-1</sup> )
NGC 3079	HCN	8.20 <sup>b</sup>	(2.94 ± 0.14) × (1.44 ± 0.06)	167 ± 2	1.51 ± 0.02	-21 ± 2	360 <sup>c</sup>
	HCO+	4.78 <sup>b</sup>	absorption	absorption	1.70 ± 0.04	-20 ± 2	-
NGC 7469	HCN	5.30 ± 0.10	(3.43 ± 0.10) × (2.73 ± 0.08)	78 ± 15	1.14 ± 0.04	118 ± 2	236 ± 9
NGC 6764	HCN	1.92 ± 0.11	(1.71 ± 0.14) × (1.31 ± 0.09)	-54 ± 25	0.82 ± 0.11	-87 ± 7	214 ± 17
	HCO+	2.28 ± 0.09	(1.69 ± 0.11) × (1.21 ± 0.06)	-66 ± 7	1.04 ± 0.11	-85 ± 8	203 ± 16
NGC 5033	HCN	1.16 ± 0.14	(1.97 ± 0.30) × (1.09 ± 0.13)	-17 ± 10	1.06 ± 0.15	158 ± 19	181 ± 32
	HCO+	0.71 ± 0.14	(1.76 ± 0.40) × (1.22 ± 0.20)	52 ± 67	0.99 ± 0.56	184 ± 51	185 ± 71

<sup>a</sup> These are given in a 3'' aperture, except for NGC 3079 where we have used a 5'' aperture.

<sup>b</sup> Fluxes are integrated across the observed line profile above the continuum level. Applying corrections in a simple way as illustrated by the blue line in the right panel of Figure 2.4 yields fluxes for HCN (1-0) of 16.1 Jy km s<sup>-1</sup> when accounting for only the continuum absorption, and 18.7 Jy km s<sup>-1</sup> when also accounting for the self-absorption. The equivalent corrected fluxes for the HCO<sup>+</sup> (1-0) line are 13.3 and 19.5 Jy km s<sup>-1</sup>.

<sup>c</sup> Estimated intrinsic line width after correcting for continuum absorption and self-absorption (i.e. it corresponds to the blue Gaussian line profile in the right panel of Fig 2.4). We have adopted an uncertainty of 20 km s<sup>-1</sup> typical of the other linewidth measurements.

### 2.3.1 NGC 3079

The 3 mm continuum is displayed in the left panel of Figure 2.1. A Gaussian fit indicates FWHM of  $1.19'' \times 1.04''$  at a PA of  $176^\circ$ . These are comparable to the beam size, indicating that the source is not spatially resolved, and has an intrinsic size  $< 0.5''$ . Because of the absorption features we have observed, the origin of the 3 mm continuum is an important issue. Maps of the radio continuum at 5–22 GHz and at resolutions to  $< 1$  mas (Trotter et al., 1998; Kondratko et al., 2005; Middelberg et al., 2007) demonstrate that it is dominated by regions that are 1–3 pc from the dynamical centre as defined by Trotter et al. (1998). Figure 2.2 shows the radio to infrared SED for NGC 3079 and indicates that the two radio lobes A and B are likely to dominate also the 3 mm continuum. In 2001, the sum of the flux densities of these two components (68 mJy) at 22 GHz was equal to the total radio continuum integrated over arcsec scales; and there is some evidence that they have continued to brighten at 22 GHz in subsequent years (Middelberg et al., 2007). The discussion below is based on the conclusion that the 3 mm continuum, which is clearly non-thermal, is dominated by the radio components A and B, rather than by any emission from the dynamical centre.

The maps of HCN (1-0) and HCO<sup>+</sup> (1-0) are presented in the middle and right panels of Figure 2.1. The grey scale image indicates the full line distribution, while the red and blue contours represent the distribution of integrated red channels and blue channels of the emission lines. For NGC 3079, the ranges for both lines extend from line centre to approximately  $-420 \text{ km s}^{-1}$  and  $+480 \text{ km s}^{-1}$ . The spatial separation and PA of the centroids of these two channels are  $\sim 1.5''$  and  $21^\circ$ . The absorption is clearly visible in the central region for both molecules. In particular, HCO<sup>+</sup> has stronger absorption than HCN. While this means we cannot reliably fit a Gaussian to the HCO<sup>+</sup> emission, it is still possible to do so on the HCN map. The resulting FWHM is  $2.94'' \times 1.44''$  and PA is  $167^\circ$  (Table 2.3).

Panel (a) of Figure 2.3 shows the integrated spectrum of NGC 3079. Although a clear P-Cygni line profile is apparent for the HCN (1-0) and HCO<sup>+</sup> (1-0) line due to the strong emission of these lines, blue-shifted absorption with two or more components dominates the profile of other lines where an emission component is weak or absent. These include H<sup>13</sup>CN (1-0) at 86.34 GHz, H<sup>13</sup>CO<sup>+</sup> (1-0) at 86.75 GHz, SiO (2-1) at 86.85 GHz, and HN<sup>13</sup>C (1-0) at 87.09 GHz (rest frequencies). The narrow absorption peak closest to systemic velocity is strongly absorbed, reaching maximum depths of 87%, 56%, 71%, and 42% of the continuum level respectively. The absorption profiles show a second narrow peak with a blue-shifted tail (that may itself contain several sub-components) that reaches to  $-350 \text{ km s}^{-1}$ . The absorption that we have identified as C<sub>2</sub>H at 87.3–87.4 GHz is at relatively low signal-to-noise and is likely to include features from several of the hyperfine transitions (Gottlieb et al., 1983; Schöier et al., 2005). We therefore exclude this from our analysis.

Panel (b) of Figure 2.3 shows the double peaked absorption of H<sup>13</sup>CN (1-0). While there may be substructure within the full velocity extent of the absorption, for our analysis, and discussion of the implications, in Section 2.5 we consider this as only two features. The reason is that we prefer to interpret the absorption in the context of its physical origin,

## 2. Thick Disks, and an Outflow, of Dense Gas in the Nuclei of Nearby Seyfert Galaxies

24

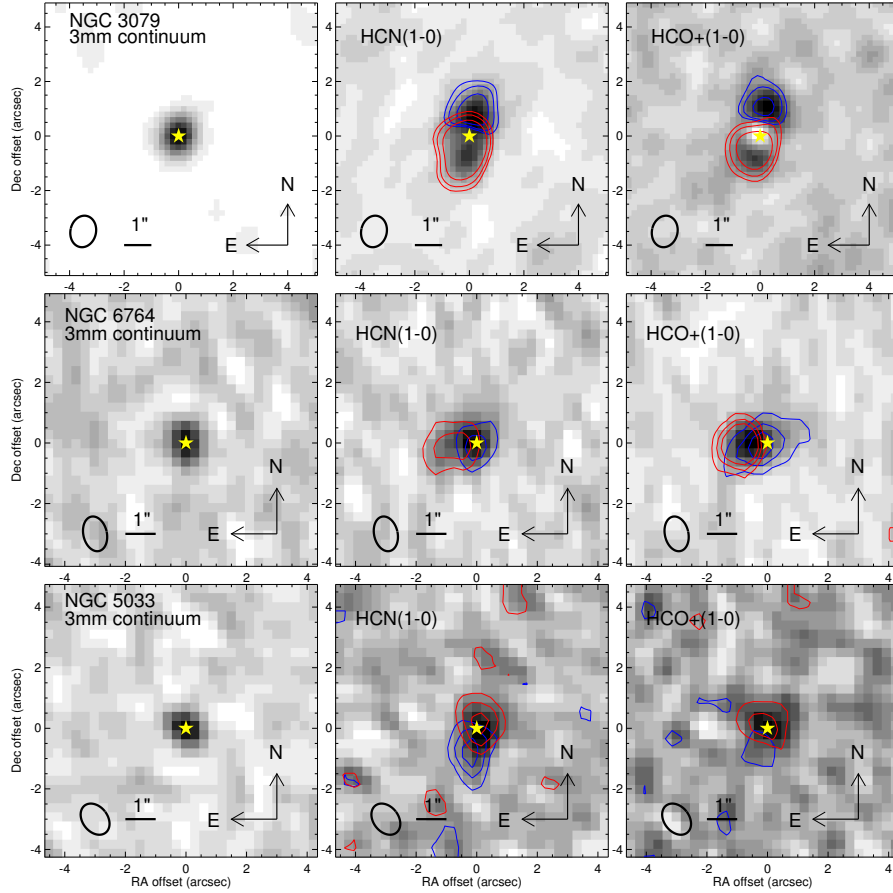


Figure 2.1: The 3 mm continuum (left panels), integrated HCN (1-0) (middle panels), and integrated HCO<sup>+</sup> (1-0) (right panels) emission maps of NGC 3079 (top row), NGC 6764 (middle row), and NGC 5033 (bottom row). In each panel, the peak position of 3 mm continuum is marked as a yellow star and the synthesized beam is drawn as an ellipse. The 3 mm continuum has been subtracted from HCN and HCO<sup>+</sup> maps. The blue and red contours represent the distribution of integrated blue and red channels of the emission lines, and are easily spatially resolved. For NGC 3079, the map is centered at 10 01 57.80 +55 40 47.2 (J2000). The absorption appears as a ‘hole’ in the central region, more clearly in the HCO<sup>+</sup> map due to the stronger absorption of that line. Blue and red contours are drawn at levels of  $2\sigma$ ,  $3\sigma$ , and  $5\sigma$ . Note that while the absorption is blue-shifted, in these images it appears to be occurring within the red contours. As becomes clear in Figure 2.8, this is because the blue-shifted emission is filling in the absorption and therefore remains below the continuum level, so the blue contours do not extend over that region. For NGC 6764, the map is centered at 19 08 16.38 +50 55 59.4 (J2000), and blue and red contours are drawn at levels of  $0.5\sigma$ ,  $1\sigma$ , and  $1.5\sigma$ . For NGC 5033, the map is centered at 13 13 27.47 +36 35 37.9 (J2000), and blue and red contours are drawn at levels of  $0.5\sigma$ ,  $1\sigma$ , and  $1.5\sigma$ .

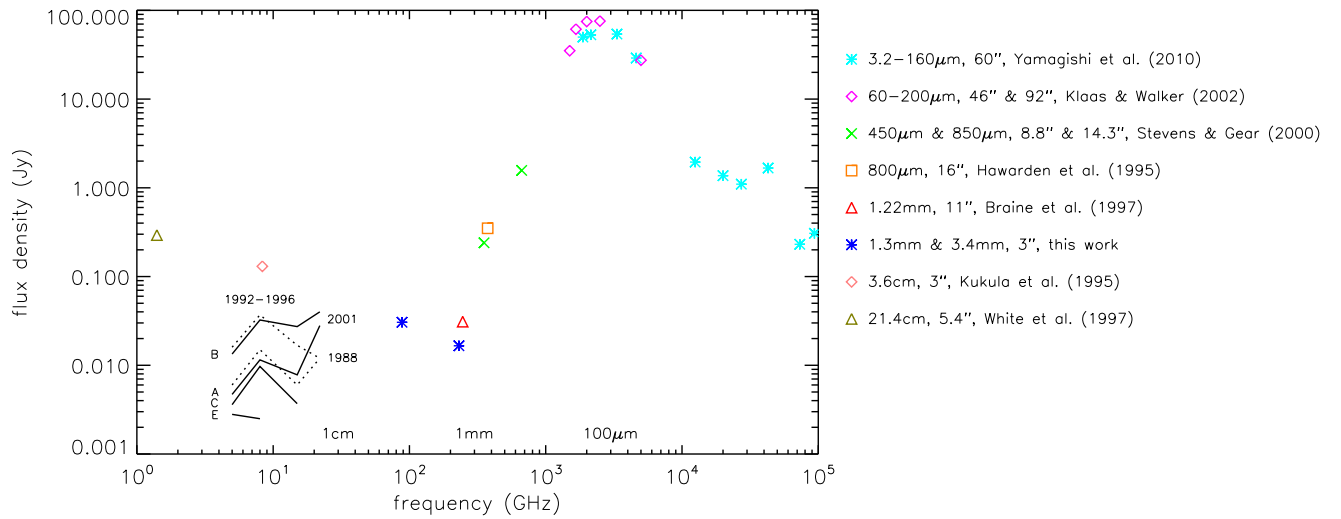


Figure 2.2: Radio to infrared spectral energy distribution (SED) for NGC 3079 as well as the interferometric mm-to-cm SED for the 4 radio emitting knots. Knots A and C are associated with approaching jet to the Southeast (SE) that is in front of the nuclear disk; while knot B is associated with the receding jet to the Northwest (NW) that is behind the disk. The SED shows that the continuum longward of 1 mm is non-thermal, and that the 3 mm continuum in the central few arcsec is likely dominated by the two radio knots A and B. References for photometry: 3.2–160  $\mu\text{m}$  (60'' apertures) from Yamagishi et al. (2010); 60–200  $\mu\text{m}$  (46'' and 92'' apertures) from Klaas & Walker (2002); 450  $\mu\text{m}$  (8.8'') and 850  $\mu\text{m}$  (14.3'') from Stevens & Gear (2000); 800  $\mu\text{m}$  (16'') from Hawarden et al. (1995); 1.22 mm (11'') from Braine et al. (1997); 1.3 mm and 3.4 mm (3'' aperture) from this work; 3.6 cm (3'' beam) from Kukula et al. (1995); 21.4 cm (5.4'' beam) from White et al. (1997). The interferometric radio continuum measurements of components A, B, C, and E with beam sizes of 0.3–8 mas are from Trotter et al. (1998) and Kondratko et al. (2005).

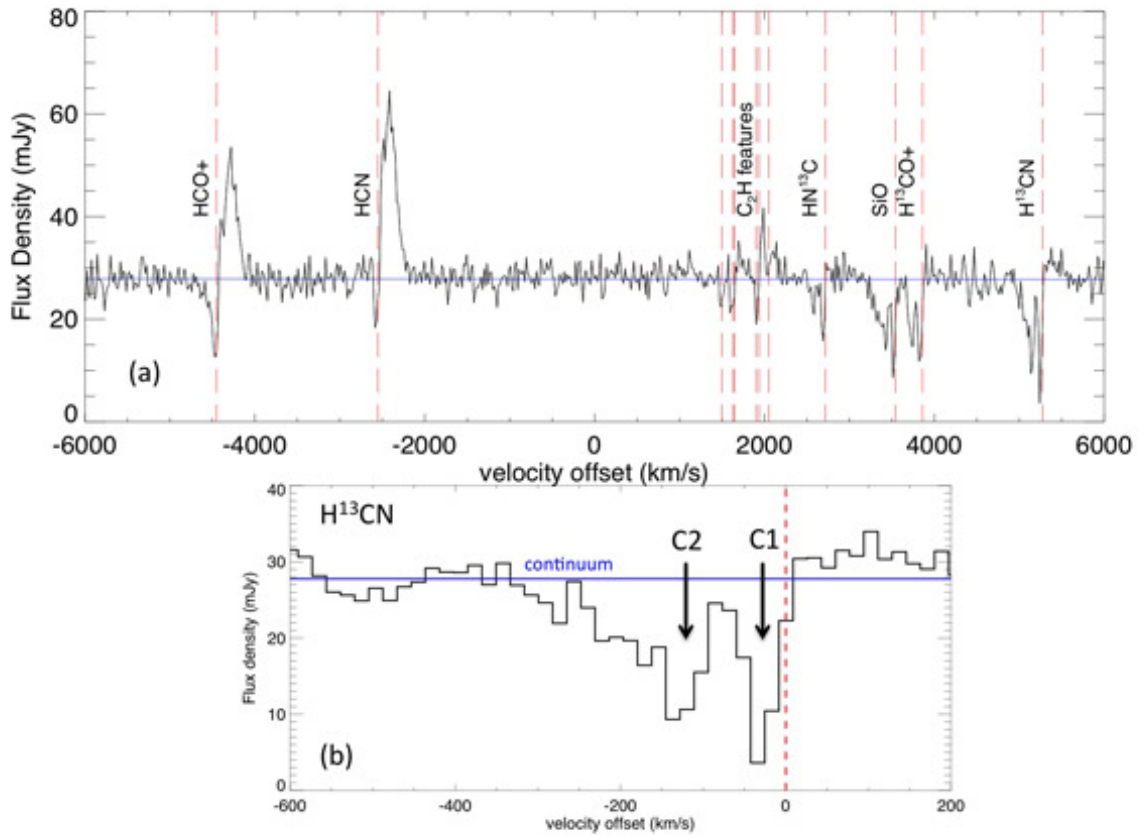


Figure 2.3: Panel (a): the spectrum of NGC 3079 integrated within a  $3''$  aperture (velocity offset is with respect to the band centre). Transitions of  $\text{H}^{12}\text{CO}^+$  (1-0),  $\text{H}^{12}\text{CN}$  (1-0),  $\text{HN}^{13}\text{C}$  (1-0),  $\text{SiO}$  (2-1),  $\text{H}^{13}\text{CO}^+$  (1-0), and  $\text{H}^{13}\text{CN}$  (1-0) are detected, as well as hyperfine transitions of  $\text{C}_2\text{H}$  (1-0). The blue solid line is a constant representing the 3 mm continuum. The red dash lines indicate the velocity offsets of each molecular transition with respect to the galaxy systematic velocity of  $1147 \text{ km s}^{-1}$ . Panel (b): The complex absorption of the  $\text{H}^{13}\text{CN}$  (1-0) transition (in a  $3''$  aperture). Velocity offsets are given with respect to its systemic, denoted by the dashed red line. The deepest absorption is labeled as "C1" and the broader absorption is labeled as "C2". Note that both absorption features are blue-shifted.

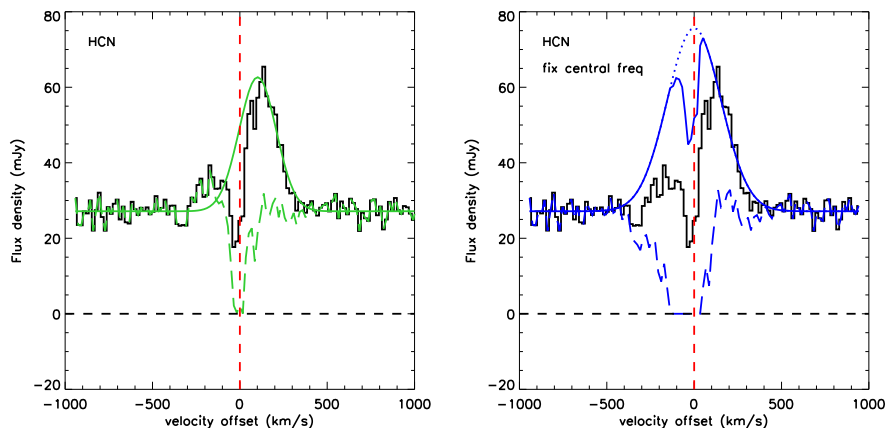


Figure 2.4: Observed and reconstructed HCN(1-0) line profiles in NGC 3079. In both panels the observed profile is drawn as a black line, and the reconstructions assume that this is the sum of continuum absorption (occurring over spatial scales of a few milliarcsec associated with radio knot B) and a Gaussian emission line (originating in the disk on scales of several arcsec). Left: the intrinsic profile has been reconstructed with the requirements that the red side of the observed profile is unabsorbed, and that the continuum absorption (dashed green line) cannot go below zero. The resulting intrinsic emission line (solid green line) is red-shifted with respect to systemic and also under-estimates the weak emission observed on the blue side of the line. In addition the continuum absorption lacks the blue wing seen in the  $\text{H}^{13}\text{CN}$  profile. Right: the additional requirement that the intrinsic line profile must be centered at the systemic velocity has been applied. The continuum absorption (dashed blue line) is now much broader and extends to velocities of  $-400$  km/s consistent with the absorption profile of the  $\text{H}^{13}\text{CN}$ (1-0) line. However, to match the observed line profile, the intrinsic Gaussian emission line (dotted blue line) must be self-absorbed (solid blue line). This is plausible because the disk of NGC 3079 is close to edge-on, so there is considerable gas at large scales in the disk along the line of sight to the nucleus. In addition, the self-absorption is centered roughly at systemic, which would be expected if cool gas within the disk is causing the self-absorption.

and we argue in Section 2.5 that the narrow peak closer to systemic is due to absorption by the nuclear disk, while the more blue-shifted component, as well as its high velocity tail, originates in absorption by outflowing gas clouds. We note also that the absorption profile of the  $\text{H}^{13}\text{CN}$  (1-0) line is very different to that of  $\text{HCN}$  (1-0). This is for two reasons: it is not saturated while, as discussed below, the  $\text{HCN}$  (1-0) absorption is strongly saturated (and as a result one cannot use the  $\text{H}^{13}\text{CN}$  (1-0) profile to correct for the  $\text{HCN}$  (1-0) absorption); and because any associated line emission is very weak, the absorption profile is not partially filled, as is the case for the  $\text{HCN}$  (1-0) line. These issues are discussed in detail below in Section 2.3.1.

There are few reports of  $\text{HCN}$  (1-0) or  $\text{HCO}^+$  (1-0) absorption in the literature. This could be because most mm spectra of galaxies are still from single dish rather than interferometric observations and, as we discuss below in Section 2.3.1, extended low intensity emission will tend to fill in any absorption of a weak continuum. The two cases of which we are aware, blue-shifted  $\text{HCO}^+$  (4-3) absorption in Arp 220 (Sakamoto et al., 2009) and red-shifted  $\text{HCN}$  (3-2) and  $\text{HCO}^+$  (3-2) absorption in IC 860 (Aalto et al., 2015), were both obtained with sub-arcsec resolution interferometric observations.

### Correction for absorption

The observed (i.e. without correcting for the absorption) flux of  $\text{HCN}$  (1-0) is  $8.20 \text{ Jy km s}^{-1}$  and of  $\text{HCO}^+$  (1-0) is  $4.78 \text{ Jy km s}^{-1}$ , both in  $5''$  apertures to cover the full extent of the observed emission. In order to estimate a correction for the absorption, we fit a Gaussian function to the emission profile, including an additional constraint that the intrinsic absorption as measured from the continuum level cannot go below zero. This approach is motivated under the assumption that the absorption and emission are effectively independent: the absorption at any given velocity occurs over a very small area (defined by the size and location of continuum sources) while the emission is integrated over the full extent of that isovelocity contour across the molecular disk (note that we did not require that the centre of the symmetric emission should be exactly at the systemic velocity of molecular line because the line emission may not be symmetric about the centre of the rotating disk), and partially fills the absorption. The best fitting profile is shown as a solid green line in the left panel of Figure 2.4, where the black solid line traces the observed  $\text{HCN}$  (1-0) profile. The difference between these is represented by the dashed green line, which traces the intrinsic absorption profile from the continuum level. Its truncated shape indicates that the  $\text{HCN}$  (1-0) line is strongly saturated. The strong red wing of the observed emission profile, and the constraint on the depth of the intrinsic absorption, result in a fit whose peak is offset by  $\sim 100 \text{ km s}^{-1}$  from systemic and which under-estimates the blue wing of the emission line profile. In addition, the continuum absorption lacks the blue wing seen in the  $\text{H}^{13}\text{CN}$  profile. To avoid these discrepancies we have made a second reconstruction, which is shown in the right panel of Figure 2.4. For this, we have added the requirement that the intrinsic Gaussian line profile (dotted blue line) should be centered at the systemic velocity. We find that, because the continuum absorption (dashed blue line) cannot go below zero, the reconstructed line profile (solid blue line) cannot be Gaussian – noting

that the sum of these two must match the observed profile. Instead, in comparison to the Gaussian, it shows absorption that is roughly symmetric and centered approximately at the systemic velocity. We interpret this to mean that the HCN (1-0) line is self-absorbed. Self-absorption in an HCN (1-0) line has been reported in IC 860 and Arp 220 W by Aalto et al. (2015) in the context of the compact obscured nuclei of luminous and ultraluminous infrared galaxies. It has also been reported in the CO 2-1 and CO 6-5 lines in Arp 220 by Engel et al. (2011) and Rangwala et al. (2015) respectively. In the case of NGC 3079 we suggest that it is occurring because the galaxy is inclined so close to edge on. As such, there is plenty of cool gas in the disk of the galaxy along the line of sight, that could absorb the line emission. From the depth of the self-absorption we estimate that a total column of  $N_{\text{HCN}} = 1.4 \times 10^{14} \text{ cm}^{-2}$  is needed to produce it, corresponding to  $N_{\text{H}} \sim 10^{21} \text{ cm}^{-2}$  if we adopt the same abundance as in Section 2.5 or as much as a few  $\times 10^{22} \text{ cm}^{-2}$  for a more typical lower HCN abundance. The absorption is at the systemic velocity because the disk motion along the line of sight to the nucleus is across the plane of the sky.

Based on our reconstruction, the flux of the self-absorbed HCN (1-0) line is  $16.1 \text{ Jy km s}^{-1}$  (nearly a factor 2 greater than the observed flux) while the total flux of the intrinsic Gaussian is  $18.7 \text{ Jy km s}^{-1}$ . A similar analysis of the  $\text{HCO}^+$  (1-0) line confirms that it does suffer more from absorption: our estimate of the self-absorbed flux is  $13.3 \text{ Jy km s}^{-1}$  (nearly a factor 3 greater than that measured directly) and the intrinsic flux in the Gaussian is  $19.5 \text{ Jy km s}^{-1}$ . The FWHM of the intrinsic Gaussian profile is  $360 \text{ km s}^{-1}$ , which we have included in Table 2.3.

### Comparison with single dish measurements

A spectrum of NGC 3079 including the lines discussed above was presented previously by Costagliola et al. (2011). This was based on data from the IRAM 30 m telescope, with a beam size of  $29''$  at 88 GHz. While the HCN (1-0) and  $\text{HCO}^+$  (1-0) lines both show a double-peaked profile – which can be generally interpreted as disk rotation or be indicative of either continuum absorption or self-absorption in the centre – their fluxes of  $24.6$  and  $27.7 \text{ Jy km s}^{-1}$  are several times greater than observed with our interferometric beam, and the line widths of  $500 \text{ km s}^{-1}$  FWHM are significantly broader. They also detect a strong blend of  $\text{C}_2\text{H}$  emission at about 87 GHz which we detect only weakly. The difference in line fluxes suggests that there is significant, but low intensity, emission from these lines on scales greater than a few arcsec. As is apparent from our data, as one integrates the flux within larger apertures, the absorption below the continuum level is filled in by the additional line emission included in the aperture, and so the line appears broader. It is likely that in the single dish measurement, continuum absorption has only a minor impact, and the double peaked profile is likely to be due to self-absorption (we note that the dip between the peaks is to a similar depth as our reconstructed self-absorbed profile). If one does not correct for this, the line width will be overestimated. For the interferometric spectrum in Figure 2.4, we can estimate the effective FWHM of the self-absorbed profile by fitting a single Gaussian to the double-peak profile. Approximating the profile in this way yields a FWHM of  $450\text{--}470 \text{ km s}^{-1}$ , similar to the  $500 \text{ km s}^{-1}$  width reported by Costagliola et

al. (2011) but significantly more than the intrinsic FWHM of  $360 \text{ km s}^{-1}$ . Similarly, once one corrects for the continuum absorption, the ratio of the HCN (1-0) and  $\text{HCO}^+$  (1-0) line fluxes is similar to that reported by Costagliola et al. (2011). We conclude that while our spectrum looks rather different from the single dish spectrum, all the differences can be understood as a result of extended low intensity emission and the aperture dependent impact of continuum absorption on the observed profile.

### 2.3.2 NGC 6764

The 3 mm continuum map is shown in the bottom left panel of Figure 2.1. Its FWHM of  $1.04'' \times 0.82''$  and PA of  $8^\circ$  indicate it is spatially unresolved. Within a  $3''$  aperture, the continuum flux density is  $0.6 \text{ mJy}$ .

Figure 2.1 also shows the integrated HCN (1-0) and  $\text{HCO}^+$  (1-0) maps in the bottom middle and right panels, and the measurements and the line fluxes are summarised in Table 2.3. The HCN (1-0) emission has an extent of  $1.7'' \times 1.3''$  at PA  $-54^\circ$ , similar to the  $1.7'' \times 1.2''$  at PA  $-66^\circ$  of the  $\text{HCO}^+$  (1-0) line. The red and blue channels of emission (from line centre to  $-435 \text{ km s}^{-1}$  and  $+465 \text{ km s}^{-1}$  for HCN; to  $-335 \text{ km s}^{-1}$  and  $+365 \text{ km s}^{-1}$  for  $\text{HCO}^+$ ) also have the same separation of  $0.82''$  at PA  $-87^\circ$ . Figure 2.5 shows integrated spectra covering the two line profiles including a constant continuum level. Their FWHMs are  $214 \text{ km s}^{-1}$  and  $203 \text{ km s}^{-1}$  respectively. Taken together, these measurements indicate that the distributions and kinematics of the two lines are very similar, and hence that they originate in the same region. This means that when constructing a simple dynamical model, as discussed in Sec. 2.4, we can constrain it using both lines, which provides an additional robustness against limitations of signal-to-noise or line specific peculiarities.

### 2.3.3 NGC 5033

The 3 mm continuum for NGC 5033 is presented in the top left panel of Figure 2.1, and has a flux density within a  $3''$  aperture of  $0.7 \text{ mJy}$ . A Gaussian fit gives a size of  $1.01'' \times 0.79''$  at PA  $41^\circ$ . As for the other 2 galaxies, this is consistent with the continuum being spatially unresolved.

The HCN (1-0) and  $\text{HCO}^+$  (1-0) maps are shown in the top middle and right panels of Figure 2.1 respectively. The measured sizes are  $2.0'' \times 1.1''$  at PA  $-17^\circ$  and  $1.7'' \times 1.2''$  at PA  $52^\circ$  respectively. We note that the latter case,  $\text{HCO}^+$  (1-0) has a large uncertainty which we attribute to the weaker  $\text{HCO}^+$  (1-0) line flux. As before, the blue and red contours represent the line emission from blue and red channels (from line centre to  $-435 \text{ km s}^{-1}$  and  $+465 \text{ km s}^{-1}$  for HCN; to  $-335 \text{ km s}^{-1}$  and  $+365 \text{ km s}^{-1}$  for  $\text{HCO}^+$ ). Their separations are  $1.1''$  and  $1.0''$  respectively. The PA for HCN (1-0) is  $-17^\circ$ ; the PA for  $\text{HCO}^+$  (1-0) differs from this but has a large uncertainty because of the low signal-to-noise in the blue channels, and is still consistent with the HCN (1-0). Figure 2.6 shows spectra extracted within a  $3''$  aperture. The flux of HCN (1-0) is  $1.2 \text{ Jy km s}^{-1}$  and of  $\text{HCO}^+$  (1-0) is  $0.71 \text{ Jy km s}^{-1}$ . The two lines have similar width, with a mean FWHM of  $183 \text{ km s}^{-1}$ . Again, we find that the

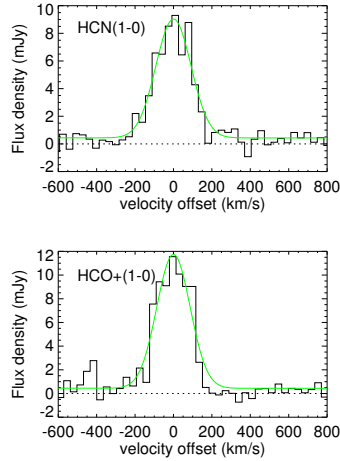


Figure 2.5: Spatially integrated spectrum for NGC 6764 showing the HCN (1-0) (top panel) and HCO<sup>+</sup> (1-0) (bottom panel) emission lines. The continuum has not been subtracted. In each case the best fitting Gaussian function is represented by the green line. The line profiles are very similar, showing a large velocity dispersion with a mean FWHM of 209 km s<sup>-1</sup>.

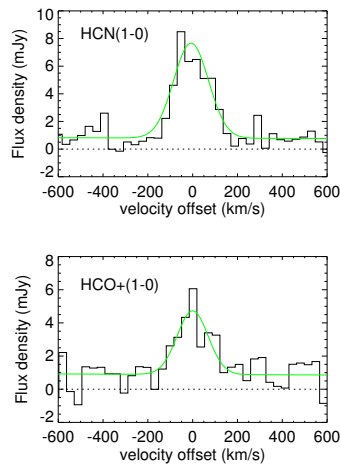


Figure 2.6: Spatially integrated spectrum for NGC 5033 showing the HCN (1-0) (top panel) and HCO<sup>+</sup> (1-0) (bottom panel) emission lines. The continuum has not been subtracted. In each case the best fitting Gaussian function is represented by the green line. And the line profiles are very similar, showing a large velocity dispersion with a mean FWHM of 183 km s<sup>-1</sup>.

distributions and kinematics of the two lines are similar, and hence conclude that they originate from the same region.

## 2.4 Modelling the kinematics

The description above of the observed characteristics shows the FWHM of the line is typically  $200 \text{ km s}^{-1}$ . Comparable line widths for the HCN (1-0) line were reported previously for the central hundred parsecs of several AGN by Sani et al. (2012). Our aim in this Section is to understand whether the line widths can be accounted for by a thin rotating disk, or whether it implies there is a significant intrinsic dispersion associated with the molecular disk of dense gas. To do so we create a simple dynamical model that can match the observed characteristics of the molecular line emission, using the same methodology as Sani et al. (2012).

To constrain our model we use four of the observed molecular gas properties listed in Table 2.3: (1) major axis FWHM, (2) minor axis FWHM, (3) separation between the centers of the blue and red channel maps, and (4) spectral FWHM of the spatially integrated line. The inclination and PA of the disk are fixed input parameters, as described below. We assume that the line traces a rotating disk and model the observed properties by applying the IDL code DYSMAL (Dynamical Simulation and Modelling Algorithm, described in Davies et al. 2011). The main purpose of this code is to quantify the impact of spectral and spatial beam smearing on an axisymmetric rotating disk. In doing so it allows us to infer the intrinsic kinematics of the disk from the observed properties. On the other hand, we include NGC 7469 using data presented in Davies et al. (2004). While the HCN (1-0) observations for that object have not been modelled in this way, the  $0.7''$  resolution 1 mm CO (2-1) and  $0.09''$  resolution  $2.12 \mu\text{m}$  H<sub>2</sub> 1-0 S(1) data enabled those authors to derive a detailed mass distribution based on the combined dynamics at their different resolutions. This object therefore allows us to directly test whether our simple dynamical model based on a single Gaussian mass distribution can be considered a working approximation in the context of disk size scale, dynamical mass, and ability to distinguish between thin and thick geometries.

### 2.4.1 Kinematic modelling procedure

The kinematic modelling procedure we use is the same as described in Sani et al. (2012). However, in addition, we explore the impact of the initial conditions on the convergence of the minimisation routine to ensure that we have reached the global rather than local minimum. To do so we generate a set of random values within broad but restricted ranges for the disk size, disk thickness, and a mass scaling ( $M_{scale}$ , which is simply a way to set the amplitude of the rotation curve, and represents the mass supported by ordered circular orbits in the disk plane). We then run a minimisation starting from these values. At each iteration, it uses DYSMAL to simulate how a disk model with the given properties would appear when convolved with the spatial beam and spectral resolution of our data. The

model is based on a Gaussian distribution, the FWHM of which is equal to the given disk size ( $R$  is half of this FWHM). The shape and amplitude of the rotation curve is derived from this in combination with the mass scaling  $M_{scale}$ . Finally, the vertical profile of the disk is defined by a Gaussian distribution, the FWHM of which is equal to the given disk thickness ( $H$  is half of this FWHM). The thickness has an observational impact both on the spatial distribution if the disk is inclined, and also on the velocity dispersion which we calculate as  $\sigma = vH/R$  and assume is isotropic. The line of sight velocity distribution is derived for each point through the inclined disk model; and, after applying appropriate beam smearing, used to generate an output cube with 2 spatial axes and 1 velocity axis. The output data cube is analysed in the same way as the real data, extracting the four properties listed above and comparing them with those extracted from the observations. The minimisation routine iteratively converges on a set of disk parameters that lead to a best match of the observed properties. After repeating this process 100 times with different initial parameters, we obtain 100 sets of the best-fit model output parameters and their corresponding  $\chi^2$ . We select the 50 sets with the lowest  $\chi^2$  and use these to estimate the mean for each model parameter (note that we use the statistical mean rather than the set of parameters from any single minimisation), and list them in Table 2.4. In a final step, we input the mean values back into DYSMAL one more time and retrieve the simulated output ‘observable’ properties, which are also listed in Table 2.4. Together with these output parameters of the model, we list the input parameters (disk size, disk thickness, and scaling  $M_{scale}$ ). To constrain the input parameter uncertainties, we estimate the input parameter distribution (either side of the best-fit values) that can satisfy the output observable properties within their uncertainties. This is similar in principle to the Markov chain Monte Carlo method, but simplified since we do not require to know the full probability distributions for the input parameters. We list the  $\pm 1\sigma$  uncertainties for input parameters in Table 2.4. We summarise the associated kinematics of the best-fit rotating disk at a radius  $R$  in Table 2.5, together with the enclosed dynamical mass  $M_{dyn}$  which we estimate as  $(v^2 + 3\sigma^2)R/G$  (as discussed in Davies et al. 2007 and Sani et al. 2012).

Table 2.4: Summary of simulated disk models:

(1) Source name; (2) Molecule; (3) Note; (4) Disk FWHM size in the disk plane; (5) Disk FWHM thickness (height); (6) Scaling  $M_{scale}$  (which sets the amplitude of the rotation curve, and represents the mass supported by ordered circular orbits in the disk plane); (7)-(10) are measured with the same method as columns (4), (5), (7), and (9) of Table 2.3; (11) reduced  $\chi^2$  of the fit.

Source	Molecule	Note <sup>(a)</sup>	Mean value of best-fit model parameters			4 simulated properties from DYSMAL				$\chi^2_{red}$
			size (arcsec)	thickness (arcsec)	$\log(M_{scale}) (M_{\odot})$	Maj. axis (arcsec <sup>2</sup> )	$\times$ min. b/r sep. (arcsec)	Line width (km s <sup>-1</sup> )		
NGC 7469	HCN	Complex	$2.41^{+0.01}_{-0.05}$	$0.43^{+0.01}_{-0.03}$	$9.95^{(b)}$	$3.15 \times 2.69$	1.22	242	6.3	
	HCN	Simple	$2.56^{+0.03}_{-0.09}$	$0.62^{+0.03}_{-0.06}$	$9.42^{+0.02}_{-0.02}$	$3.27 \times 2.84$	1.15	235	4.5	
NGC 6764	HCN	-	$1.35^{+0.03}_{-0.10}$	$0.25^{+0.01}_{-0.14}$	$8.66^{+0.05}_{-0.07}$	$1.71 \times 1.21$	0.74	203	2.2	
	HCO <sup>+</sup>	-	$1.43^{+0.03}_{-0.10}$	$0.26^{+0.01}_{-0.15}$	$8.75^{+0.06}_{-0.04}$	$1.77 \times 1.23$	0.79	217	6.6	
NGC 5033	HCN	-	$1.70^{+0.08}_{-0.15}$	$0.01^{+0.06}_{-0.00}$	$8.47^{+0.05}_{-0.15}$	$1.94 \times 1.17$	0.98	182	0.7	
	HCO <sup>+</sup>	-	$1.54^{+0.09}_{-0.14}$	$0.19^{+0.08}_{-0.12}$	$8.37^{+0.05}_{-0.15}$	$1.85 \times 1.18$	0.88	190	0.1	
NGC 3079	HCN	-	$2.66^{+0.02}_{-0.03}$	$0.45^{+0.01}_{-0.05}$	$9.30^{+0.03}_{-0.06}$	$2.92 \times 1.43$	1.51	378	0.9	

Note: the uncertainties given are derived as joint uncertainties and hence implicitly take into account possible partial correlations between parameters.

<sup>(a)</sup>For NGC 7469 'complex' refers to the multi-component dynamical model from Davies et al. (2004), 'simple' to the single Gaussian representation for the mass distribution.

<sup>(b)</sup> Fixed to  $M_{scale} = 9 \times 10^9 M_{\odot}$  as given by Davies et al. (2004).

Table 2.5: Intrinsic kinematics of the modelled rotating disks:

(1) Source name; (2) Molecule; (3) Radius (half of the FWHM given in Table 2.4); (4) Rotational velocity at R; (5) Velocity dispersion at R; (6) Enclosed dynamical mass estimated as  $(v^2+3\sigma^2)R/G$ .

Source	molecule	R (pc)	v (km s <sup>-1</sup> )	$\sigma$ (km s <sup>-1</sup> )	$\log(M_{dyn})$ ( $M_{\odot}$ )
NGC 7469	HCN <sup>(a)</sup>	356	131	47	9.30
	HCN <sup>(b)</sup>	377	128	62	9.39
NGC 6764	HCN	101	102	38	8.54
	HCO <sup>+</sup>	108	110	40	8.63
NGC 5033	HCN	62	104	1.4	8.20
	HCO <sup>+</sup>	56	98	25	8.18
NGC 3079	HCN	112	204	69	9.16

<sup>(a)</sup>Complex model with multiple components; <sup>(b)</sup> Simple model with 1 component.

## 2.4.2 NGC 7469

Although the interferometric beam size at 3 mm is only  $\sim 1''$ , this is still relatively large compared to the scale of the nuclear structures. As a result, models are necessarily very simple and we have used a single Gaussian mass distribution to define the rotation curve and emission distribution. Since we are limited to using a very simple model, we use NGC 7469, which has been already successfully modeled with a complex mass distribution, to assess whether our approach is applicable. Davies et al. (2004) constructed a single axisymmetric mass model for NGC 7469 comprising a broad disk, a ring and an extended nucleus to interpret the observations of CO (2-1) and the K-band H<sub>2</sub> 1-0 S(1) line at different resolutions. The details of this mass model are summarized in their Table 2, and we adopt it for our analysis, calling it the ‘complex model’. While the mass distribution represented by these 3 components is fixed, we represent the HCN (1-0) line emission distribution by a single independent component (i.e. the kinematics of the line are defined by the fixed mass distribution, but the distribution of the line emission does not necessarily follow that of the mass). One additional assumption we make is that all the components share the same thickness. This is a free parameter in the model, as is the size scale of the luminosity distribution, while the mass scale (as before, this represents only the mass supported by ordered circular orbits in the disk plane) is fixed to  $M_{scale} = 9 \times 10^9 M_{\odot}$  as derived by Davies et al. (2004). When applying our kinematics modelling procedure as described above, the best-fit values for the disk size and disk thickness are  $2.41''$  and  $0.43''$  respectively. And, as summarised in Table 2.5, accounting for rotation and dispersion, we estimate the dynamical mass to be  $\log M_{dyn}[M_{\odot}] = 9.30$ . In comparison, when using a single Gaussian profile to define the mass distribution (hereafter called the ‘simple model’), we leave the disk size, disk thickness, and mass scale as three free parameters. We then derive best-fit mean values for disk size and thickness to be  $2.56''$  and  $0.62''$ , and estimate  $\log M_{dyn}[M_{\odot}] = 9.39$ . There are two key results here. The first is that the disk size and thickness are consistent

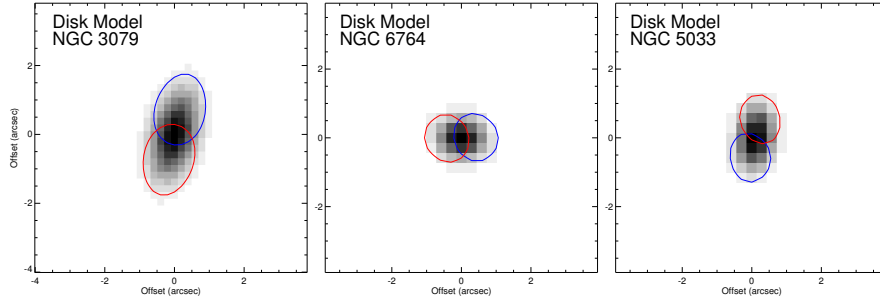


Figure 2.7: Simulated disk models for the 3 sources with new observations, convolved with the appropriate beam. As for Figure 2.1, the greyscale image shows the emission of the modelled disk while the blue and red contours represent the distribution of integrated blue and red channels of the emission lines (at 50% of the peak intensity). We show the model for only one line, but it is a good representation for both HCN (1-0) and HCO<sup>+</sup> (1-0). A PV diagram extracted from the model for NGC 3079 is shown in Figure 2.8.

between the two models, as is  $M_{dyn}$ . The second is that the model implies the disk is thick, with an intrinsic  $\sigma/v \sim 0.4$ . While the dispersion we derive of 50–60 km s<sup>-1</sup> is larger than the 30 km s<sup>-1</sup> seen directly in the higher spatial resolution CO (2-1) data by Davies et al. (2004), both would lead to the same conclusion in the context of distinguishing between a thick disk and a thin disk: that a significant intrinsic dispersion is required, and a thin disk is ruled out.

Thus we can estimate the intrinsic kinematics, and in particular the dispersion (thickening), for the disk using a simple approximation to the mass distribution. In the rest of this Section, we make use of the simple model to derive the intrinsic kinematics also for NGC 6764 and NGC 5033.

### 2.4.3 NGC 6764

When modelling NGC 6764, we assume that the nuclear disk and galactic disk have the same inclination, which we set to 62° (Leon et al., 2007). And we note that the PA of the line emission, as well as its velocity gradient, are approximately perpendicular to the parsec-scale core-jet structure (PA  $\sim$  25°, Kharb et al. 2010). We caution that, while the velocity gradient we see at radii up to 1'' is consistent with that of the CO (2-1) line up to radii of 5'' (Leon et al., 2007), our model focusses on the smaller scale and may not represent the properties of the rotating disk at  $\geq 200$  pc, which might be perturbed by streaming motions associated with the bar.

We perform the kinematics modelling separately on each of the two lines, which independently yield essentially the same solution: a disk with a size of  $\sim 1.4''$  and a thickness of  $\sim 0.25''$ . We conclude that the observational constraints require a thick disk model to explain the line emission distribution and kinematics, and in particular the large velocity width of the molecular lines. In our assumption of hydrostatic equilibrium, the disk thickness of the model corresponds to an intrinsic  $\sigma/v \sim 0.37$ .

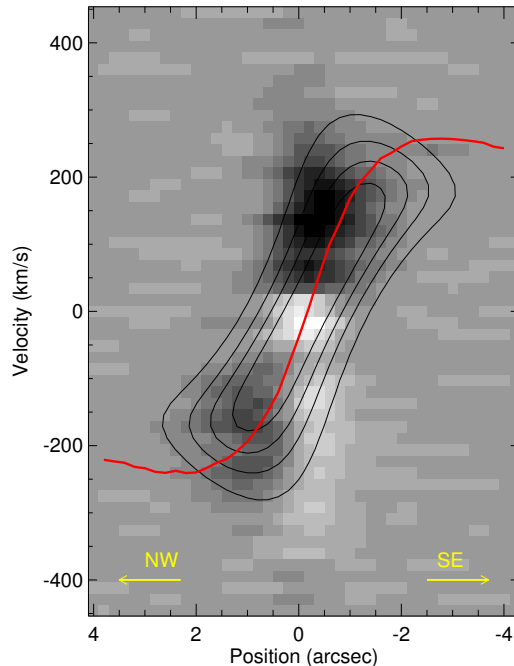


Figure 2.8: The observed PV diagram (grey scale) for the HCN(1-0) line in NGC 3079, extracted along the major axis (slit  $1''$  wide at a PA of  $165^\circ$ ). The beam-convolved PV diagram from our axisymmetric dynamical model is overplotted as black contours (20%, 40%, 60%, and 80% of the peak intensity). The red line traces the rotation curve derived from it using the iteration method (Takamiya & Sofue, 2002). Positive and negative positions indicate the NW and SE direction respectively.

#### 2.4.4 NGC 5033

For NGC 5033, based on the kinematical parameters derived from the CO(1-0) velocity field (Kohno et al., 2003), we fix the inclination to  $66^\circ$ . We note also that the PA on those larger scales matches what we have measured on  $1''$  scales for the HCN(1-0) and HCO<sup>+</sup>(1-0) lines, and is approximately perpendicular to the synchrotron radiation from the core-jet structure, which is oriented east-west (Pérez-Torres & Alberdi, 2007).

Our modelling results differ for the two lines. The characteristics of the HCN(1-0) line are well matched by a very thin disk with a size of  $1.7''$ . In contrast, the HCO<sup>+</sup>(1-0) emission is better matched by a thicker disk with a size of  $1.54''$  and a thickness of  $0.19''$ . However, due to the low signal-to-noise of the HCO<sup>+</sup>(1-0) line emission, the observable properties have large uncertainties and so the model is poorly constrained, as reflected in the very small  $\chi^2$  for this fit. For this object there is no convincing evidence for a thick disk. We conclude that our kinematic analysis favours the thin disk solution, for which the corresponding intrinsic  $\sigma/v$  ratio is  $< 0.1$ .

### 2.4.5 NGC 3079

Despite the absorption in the molecular emission lines, we still apply the kinematics modelling to HCN (1-0); however, we exclude HCO<sup>+</sup> (1-0) since the effect of the absorption is too severe. According to the kinematical parameters derived from the CO (1-0) velocity field (Koda et al., 2002), we fix the nuclear disk inclination to 77° and PA to 165°. In addition, to reduce any bias caused by the impact of the absorption in setting the amplitude of the rotation curve, we also fix  $M_{scale} = 2 \times 10^9 M_{\odot}$  (at 3'') based on the value derived by these authors from their kinematical modelling of the CO (2-1) line of their ‘core’ component, which we identify as the component traced by the HCN (1-0) and HCO<sup>+</sup> (1-0) lines. The best-fit mean values for the disk size and thickness are 2.66'' and 0.45''. The associated dispersion is just under 70 km s<sup>-1</sup>, consistent with the 60 km s<sup>-1</sup> of Koda et al. (2002), and confirms that the dense clouds exhibit significant intrinsic random motions. The observed line emission distributions and kinematics need the thick disk geometrical structure, the corresponding intrinsic  $\sigma/v$  ratio is  $\sim 0.33$ .

Since the emission lines are better spatially resolved in NGC 3079 than the other targets, we plot a position-velocity (PV) diagram in Figure 2.8 extracted along the major axis. The greyscale image shows that emission as darker colours and the absorption in lighter colours. Superimposed are contours tracing our axisymmetric dynamical model. Given the simplicity of this model, it traces the emission very well, although the line emission does show deviations from axisymmetry (in particular, the south eastern side shows indications for red-shifted emission at  $V > 200$  km s<sup>-1</sup> at a radial offset of  $\leq 0.5''$ ). We have used the iteration method (Takamiya & Sofue, 2002; Sofue & Rubin, 2001) to derive the central rotation curve from the beam-convolved model, and overplotted this on the figure. The model compares well with Figure 15 of Koda et al. (2002), where the spatial resolution was slightly poorer than ours, but which was not hampered by absorption.

### 2.4.6 Kinematics summary

For three of the four galaxies we have modelled, the nuclear emission line characteristics require a thick disk with  $\sigma/v \geq 0.3$ . The validity of our results is demonstrated for 2 objects. For NGC 7469, matching the kinematics of higher resolution CO (2-1) and H<sub>2</sub> 1-0S(1) data to a detailed mass model, Davies et al. (2004) noted that the dispersion of the CO (2-1) line had to be a relatively high 30 km s<sup>-1</sup>. For NGC 3079, focussing on the ‘core’ component seen in CO (2-1) data, Koda et al. (2002) required a dispersion of 60 km s<sup>-1</sup> to model the kinematics.

Sani et al. (2012) performed a similar kinematic analysis of the HCN (1-0) line for four other nearby Seyfert galaxies, finding  $\sigma/v$  in the range 0.3–0.5 for all of them. We combine these with our kinematic analysis above and summarize the combined modelling results in Table 2.6. We find that in 7 out of 8 nearby Seyferts,  $\sigma/v \geq 0.3$ . Only for NGC 5033 do we find evidence that the disk is thin, with  $\sigma/v \leq 0.1$ . We conclude that thick molecular disks are a common occurrence in the central  $\sim 100$  pc of Seyfert galaxies.

Table 2.6: Summary of the kinematic modelling for the combined sample which includes the 4 Seyferts analysed here and 4 Seyferts from Sani et al. (2012).

(1) Source name; (2) HCN (1-0) Luminosity (3) Radius; (4) Rotational velocity at  $R$ ; (5) Velocity dispersion at  $R$ ; (6) Enclosed dynamical mass.

Source	$L_{HCN}$	R (pc)	v (km s <sup>-1</sup> )	$\sigma$ (km s <sup>-1</sup> )	$M_{dyn}$ ( $M_{\odot}$ )
NGC 7469 <sup>a</sup>	7.87	356	131	47	9.30
NGC 6764 <sup>b</sup>	6.90	101	102	38	8.54
NGC 5033 <sup>b</sup>	6.36	62	104	1	8.20
NGC 3079	7.49	112	204	69	9.16
NGC 2273	6.86	97	83	33	8.36
NGC 3227	6.52	23	105	42	7.98
NGC 4051	5.88	22	47	19	7.23
NGC 6951	6.36	45	84	34	8.04

<sup>(a)</sup>From the complex model.

<sup>(b)</sup>We have adopted the model based on the HCN (1-0) line: for NGC 6764 it provides a better fit; for NGC 5033 it provides a better constrained fit.

## 2.5 Column density through the inner disk of NGC 3079

In this section, we use the depth of the absorption features in the spectrum of NGC 3079 to make a direct estimate of the gas column density of the disk, and discuss the origin of the absorption features.

We already noted in Section 2.3.1 that the H<sup>12</sup>CN (1-0) absorption is saturated, making it difficult to use reliably to derive column density. Instead, the H<sup>13</sup>CN (1-0) is an ideal transition for this purpose, not only because it is unsaturated but also because its frequency is far enough away from other transitions that it is unblended. The spectral profile of the absorption from this line is shown in panel (c) of Figure 2.3, and the systemic velocity, for which we have adopted 1147 km s<sup>-1</sup> (Koda et al., 2002), is drawn as a dashed red line. The solid blue line represents the continuum flux density within the 3'' aperture. The deeper absorption (the component close to the systemic velocity) is denoted ‘‘C1’’; the broader absorption component (further blue-shifted from the systemic velocity) is denoted as ‘‘C2’’.

### 2.5.1 Column densities

Assuming that local thermal equilibrium (LTE) conditions hold, the velocity integrated optical depth can be used to derive the total column density of molecules (Wiklind & Combes, 1995). For an absorption line  $J \rightarrow J + 1$ :

$$N_{total} = \frac{8\pi}{c^3} \frac{\nu^3}{A_{J+1,J} g_{J+1}} \frac{Q(T_{ex}) \exp(E_J/kT_{ex})}{1 - \exp(-h\nu/kT_{ex})} \int \tau_{\nu} dV \quad (2.1)$$

where  $A_{J+1,J}$  is the Einstein A coefficient,  $g_{J+1} = 2J + 1$  is the statistical weighting of level J,  $E_J$  is the energy of level J,  $Q(T_{ex}) = \sum_{J=0}^{\infty} g_J \exp(-E_J/kT_{ex})$  is the partition function, and  $\int \tau_{\nu} dV$  is the velocity integrated optical depth. In order to calculate this, we have used coefficients from the Leiden Atomic and Molecular Database (Schöier et al., 2005), for which the energy levels and radiation transitions extend up to  $J = 29$ . The excitation temperature,  $T_{ex}$ , is set as 4K which is consistent with a high opacity of the lower transitions and, as concluded for NGC 5128 by Muller & Dinh-V-Trung (2009), is expected for densities up to  $\sim 10^4 \text{ cm}^{-3}$ . We estimate the optical depth over the source as:

$$\tau_{\nu} = -\ln\left(\frac{I_{\nu}^{obs}}{I_{\nu}^{cont}}\right) \quad (2.2)$$

where  $I_{\nu}^{obs}$  is the observed flux density of the absorption feature and  $I_{\nu}^{cont}$  is the continuum flux density transmitted by the background non-thermal radio sources.

The velocity integrated optical depths of C1 and C2 are  $46.13 \text{ km s}^{-1}$  and  $80.88 \text{ km s}^{-1}$ , from which we estimate associated column densities for  $\text{H}^{13}\text{CN}$  of  $1.5 \times 10^{14} \text{ cm}^{-2}$  and  $2.6 \times 10^{14} \text{ cm}^{-2}$  respectively. In order to derive the hydrogen column density  $N_H$ , we need to apply two corrections. The first one is for the  $^{12}\text{C}/^{13}\text{C}$  isotope ratio, which we assume to be 60, similar to the local interstellar medium (Milam et al., 2005). However, we note that this conversion may be underestimated if the circumnuclear region has a high star formation rate, for example M82 and NGC 253 have  $^{12}\text{C}/^{13}\text{C} \sim 100$  (Martín et al., 2010). The second correction is for the  $\text{H}^{12}\text{CN}$  abundance  $X_{\text{HCN}}$ . (Harada et al., 2010) have calculated values in the range  $3 \times 10^{-6}$  to  $9 \times 10^{-9}$  for gas on scales of a few to tens of parsecs around an AGN, depending on timescale. These values are for warm ( $\sim 100\text{--}400 \text{ K}$ ) gas, similar to the molecular gas temperatures found in the central regions of Seyfert galaxies (Davies et al., 2012; Hailey-Dunsheath et al., 2012; Krips et al., 2008; Viti et al., 2014). In the absence of specific constraints, we adopt the geometrical mean of these two values,  $X_{\text{HCN}} \sim 10^{-6.8}$ , which is consistent with the plentiful evidence for X-ray enhanced HCN abundance around AGN. Consequently,  $N_H$  for the C1 and C2 components is  $\sim 5.6 \times 10^{22} \text{ cm}^{-2}$  and  $\sim 9.8 \times 10^{22} \text{ cm}^{-2}$  respectively.

Support for the high column density in the central disk of NGC 3079 comes from the SiO absorption. Numerous observations have shown that SiO is commonly found in massive star forming regions and in shocked clumps related to supernova remnants (e.g. Downes et al. 1982 and Ziurys et al. 1989a). And enhancement of the SiO abundance has been predicted in high temperature chemistry reactions and models which contain shocks or molecular formation in fast molecular outflows (Martin-Pintado et al., 1992; Klaassen & Wilson, 2007).

We estimate SiO column densities for components C1 and C2 in NGC 3079 as  $\sim 2.8 \times 10^{14} \text{ cm}^{-2}$  and  $\sim 3.4 \times 10^{14} \text{ cm}^{-2}$  respectively. For both components the ratio of SiO abundance to HCN is in the range 0.02–0.03. These ratios are significantly higher than found in dark clouds or quiescent regions (where ratios  $\leq 0.003$  are expected), but also significantly less than the range 0.1–1 found in massive star forming regions. They are more comparable to the perturbed clouds associated with supernova remnant IC 443 where

$X_{SiO}/X_{HCN} \sim 0.04\text{--}0.06$  (Ziurys et al., 1989b), and also to the circumnuclear disk of NGC 1068 where  $X_{SiO}/X_{HCN} \sim 0.06\text{--}0.1$  (Usero et al., 2004). Adopting  $X_{SiO} \sim 0.5 - 1 \times 10^{-8}$  as found by Usero et al. (2004) for NGC 1068, we estimate column densities of  $0.3\text{--}1 \times 10^{23} \text{ cm}^{-2}$  for C1 and C2 in NGC 3079.

We note that comparison with  $N_H$  derived from X-ray spectra towards the AGN is difficult. An estimate based on a BeppoSAX observation was  $N_H \sim 10^{25} \text{ cm}^{-2}$  (Iyomoto et al., 2001), while another based on Chandra observations was  $N_H \sim 2 \times 10^{22} \text{ cm}^{-2}$  (Cecil et al., 2002). On the other hand, both X-ray observatories did strongly detect the Fe K $\alpha$  complex at 6.4 keV, which is a fluorescence line produced when nuclear continuum radiation is reprocessed by circumnuclear material, and is consistent with heavy absorption.

### 2.5.2 Origin of the absorption

The central velocities of C1 and C2 are  $29 \text{ km s}^{-1}$  and  $137 \text{ km s}^{-1}$  respectively. This double peaked absorption not only appears in several molecules (e.g.  $\text{H}^{13}\text{CN}$ ,  $\text{H}^{13}\text{CO}^+$ , SiO and  $\text{HN}^{13}\text{C}$ ) in the spectrum in Figure 2.3, but is also present in the OH absorption observed on milli-arcsec scales with the European VLBI Network (EVN) (Hagiwara et al., 2004). Although different observations use distinct molecules, the velocity difference between the two absorption features has a consistent value of  $\sim 100 \text{ km s}^{-1}$ .

#### Component C1

Owing to the alignment of the water maser distribution with the kiloparsec-scale CO molecular structure, Trotter et al. (1998) proposed a highly inclined molecular disk, oriented roughly north-south, as the geometry of the nuclear region in NGC 3079. In addition, Kondratko et al. (2005) measured the water maser kinematics and concluded the presence of a relatively thick and flared disk structure in the centre. We adopt these ideas from the literature and suggest that the deeper absorption C1 originates from the blue-shifted part of the rotating molecular disk, which lies in front of the bright radio jet continuum source B, which we discussed in Section 2.3.1 as also being one of the primary sources of the 3 mm continuum. Adopting a black hole mass  $2 \times 10^6 M_\odot$  (Kondratko et al., 2005), and taking into account the inclination of the rotating disk and the location at which the absorption is occurring, we estimate that the velocity associated with the disk absorption should be  $-47 \text{ km s}^{-1}$ , in good agreement with the observed velocity of component C1. In contrast, the red-shifted part of the rotating molecular disk is located behind the other prominent radio jet continuum source, A; and therefore no equivalent redshifted absorption occurs in the spectrum. This scenario of off-centre absorption in the nuclear region of NGC 3079 is illustrated in the right panel of Figure 2.9. Based on this scheme, we argue that C1 may trace the intrinsic column density of neutral hydrogen in the edge-on rotating molecular disk, which we conclude is therefore  $N_H \sim 6 \times 10^{22} \text{ cm}^{-2}$ .

Despite the size of our 3 mm beam, this column is measured at radial scales of  $\sim 1 \text{ pc}$  because that is the projected location of the continuum against which the absorption is occurring. If it applies throughout the nuclear disk, we can estimate a gas mass that we

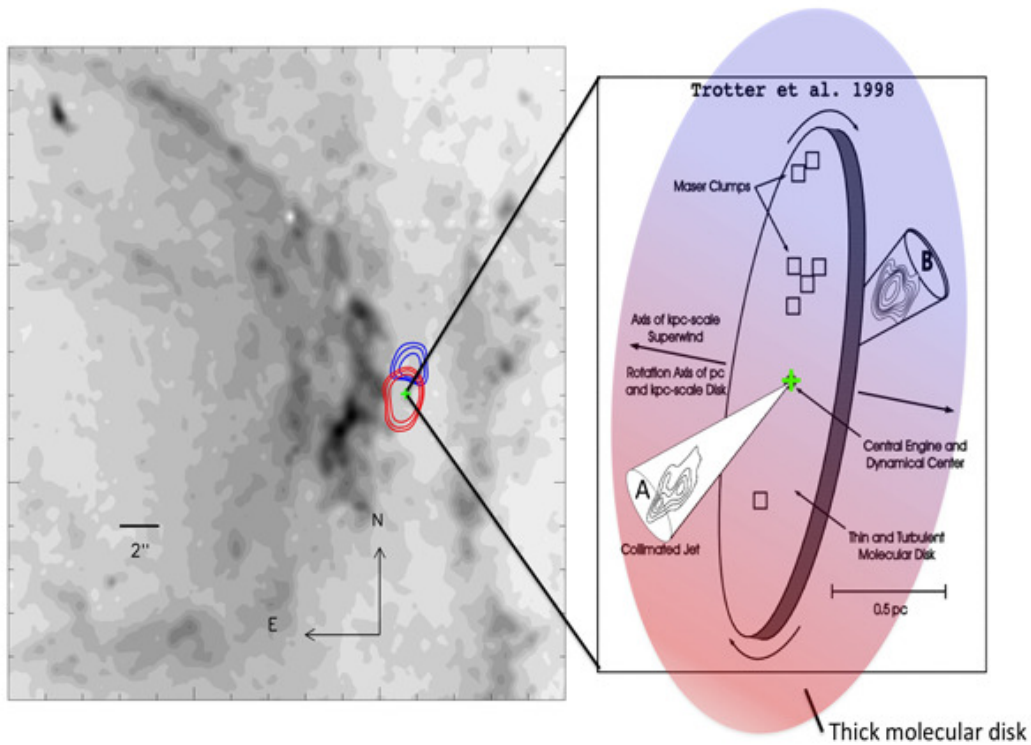


Figure 2.9: Left panel: greyscale image is the  $[\text{N II}] + \text{H}\alpha$  map of the superbubble and ionized filaments observed by HST (Cecil et al., 2001). The blue and red contours are the distribution of integrated blue and red channels of  $\text{H}^{12}\text{CN} (1-0)$  presented in this paper. The central green symbol indicates the position of the nucleus. Right panel: the distribution of maser emitters (open squares) and 22 GHz radio continuum (grey contours) in the nuclear region of NGC 3079, adapted from Trotter et al. (1998) and Kondratko et al. (2005). The pale blue-red colour gradient across the ellipse represents the kinematics we have observed for the rotating molecular disk. The bright radio component B in the collimated jet to the NW lies behind the disk and causes the blue-shifted absorption in the 3 mm continuum. The cone to the SW represents the collimated jet and radio component that lies in front of the disk, and so has been left uncoloured. The green plus symbol marks the dynamical centre adopted by Kondratko et al. (2005) in their maser kinematics model.

can compare with the dynamical mass  $M_{dyn}$  from Section 2.4, and hence estimate a gas fraction. Assuming that the absorption is caused by only 1–2 clouds along the line of sight so that no inclination correction is required, the gas mass within a radius of 112 pc (the same as that used to derive  $M_{dyn}$ ) is  $2 \times 10^7 M_{\odot}$ . For  $\log M_{dyn}[M_{\odot}] = 9.16$  (Table 2.5), we find a gas fraction  $f_{gas} = 1.3\%$ .

These numbers are remarkably similar to the estimates of Hicks et al. (2009). Based on direct CO measurements as well as typical gas fractions for local spirals and star formation galaxies, these authors argued that even with a low gas fraction of 1% the columns exceed  $10^{22} \text{ cm}^{-2}$  on scales out to several tens of parsecs, and values are more typically a few  $10^{23} \text{ cm}^{-2}$ . Their estimates based on extinction to the stellar continuum (assuming the obscuring material is mixed with the stars) suggested slightly lower values with a mean of  $2.4 \times 10^{22} \text{ cm}^{-2}$ . Our independent measurement based on absorption confirms that in NGC 3079, although the gas fraction in the nucleus is low, there is still sufficient material on scales of at least several parsecs to cause significant optical obscuration from some directions.

### Component C2

Absorption component C2 has a broad wing that extends to at least  $200 \text{ km s}^{-1}$  blueward from the central velocity of C2. Component C2 could be associated with OH absorption (Hagiwara et al., 2004). But in contrast to the extended HCN velocity profile, the OH absorption observed with 45-mas resolution ( $\sim 4 \text{ pc}$ ) shows only the deep absorption of C2 without the broad blue-shifted wing. We suggest below that the broad wing could be caused by absorption in outflowing material. The  $\text{H}\alpha$  features resembling outflow in the nuclear region of NGC 3079 are displayed in the left panel of Figure 2.9. The brightest emission shows that the bubble apex is close to the nucleus, and shocks induced in the bubble wall extend out to large-scales tracing the extent of the super wind (Veilleux et al., 1994). An ionized filament with a blue-shifted velocity of  $125 \text{ km s}^{-1}$  relative to systemic lies at a distance of  $\sim 400 \text{ pc}$  (4–5") from the nucleus, and its morphology aligns with the VLBI-scale radio jet (Cecil et al., 2001). We speculate that the broad blue-shifted wing – and hence the whole of component C2 – may trace outflows on projected scales larger than 4 pc but smaller than  $\sim 40 \text{ pc}$  (noting that this corresponds to half the 1" FWHM of the IRAM beam). This would imply a column density in the outflowing material of  $N_H \sim 10^{23} \text{ cm}^{-2}$ , comparable with that of the material in the disk. While this seems remarkably high, outflowing material with a similar high  $N_H \sim 5 \times 10^{22} \text{ cm}^{-2}$  has been reported for the Seyfert 2 galaxy NGC 1433 (Combes et al., 2013).

## 2.6 HCN luminosity and dynamical mass

In this section we explore the relation between HCN luminosity  $L_{HCN}$  and dynamical mass  $M_{dyn}$  in the central  $\sim 100 \text{ pc}$  of Seyfert galaxies, and its implications. We use the combined sample of 8 Seyferts with 1" HCN (1-0) observations and kinematical modelling, as given

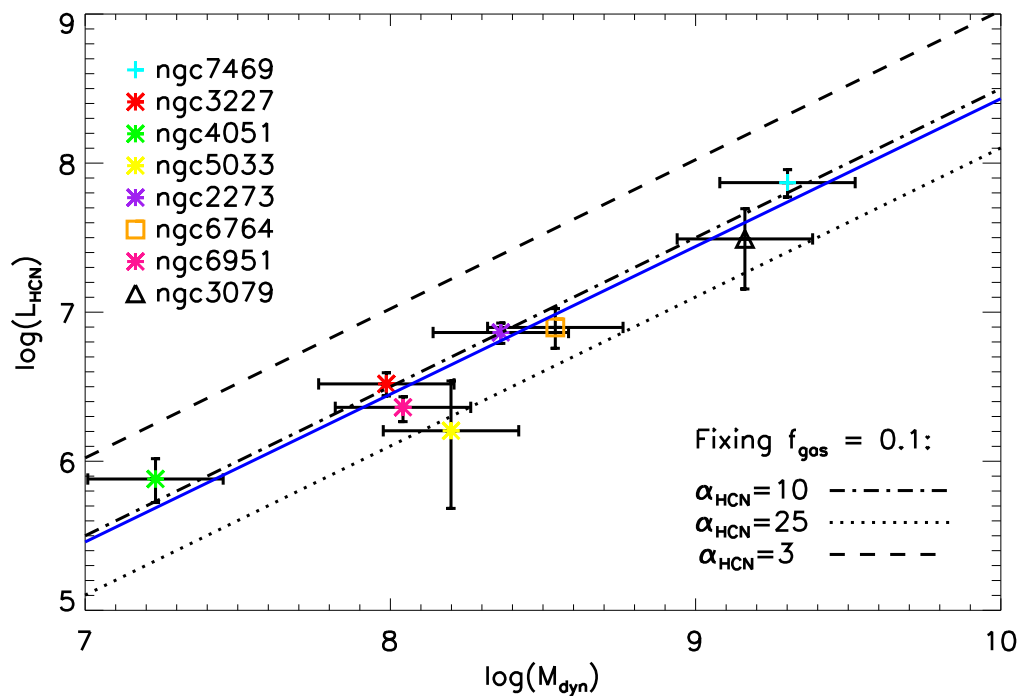


Figure 2.10: HCN luminosity plotted against dynamical mass for AGN analysed here and in Sani et al. (2012). The uncertainty in HCN luminosity includes errors from HCN flux density and distance. We adopt an uncertainty in dynamical mass of 40% (see text in Section 2.6 for details). The solid blue line is the best-fit linear relation for this data set. According to Equation 2.7, and assuming a gas fraction of 10%, the three black lines represent different HCN conversion factors:  $\alpha_{HCN} = 3$  (dashed),  $\alpha_{HCN} = 10$  (dot-dashed), and  $\alpha_{HCN} = 25$  (dotted)

in Table 2.6.

Following Gao et al. (2007), the HCN luminosity is calculated as

$$L_{HCN} = 4.1 \times 10^3 S_{HCN} \Delta v (1+z)^{-1} D_L^2 \quad (2.3)$$

in units of  $\text{K km s}^{-1} \text{pc}^2$ , where  $S_{HCN} \Delta v$  ( $\text{Jy km s}^{-1}$ ) is the velocity integrated HCN flux density and  $D_L$  (Mpc) is the luminosity distance. Since all our objects are in the very local universe, the  $(1+z)^{-1}$  term is approximately unity. The uncertainty in HCN luminosity includes uncertainties from the velocity integrated flux density as well as the distance.

The uncertainties on  $M_{dyn}$  are difficult to quantify robustly because of the assumptions and simplifications in the kinematic model from which  $M_{dyn}$  is derived. For the galaxies they modelled, Sani et al. (2012) state that the random errors are 15–20% excluding the uncertainty for the  $\sigma$  term. From our modelling, which provides a more statistical estimate of the uncertainties based on the distribution of parameters in the best-fitting models, the uncertainties are 30–40%. However, we (and also Sani et al. 2012) adopted fixed inclinations and did not take their uncertainties into account. The inclinations we have used for each galaxy are given in the relevant subsections of Sec. 2.4, and we note that in all of the objects we have modelled as well as all of those modelled by Sani et al. (2012) the PA of the nuclear HCN emission matches rather well the PA of the host galaxy on larger scales. Since a warp is likely to alter the PA (as well as the inclination), the similarity of the PA on large and small scales suggests the impact of any warp on the observed orientation should be modest. We therefore have simply adopted the same inclinations as measured on large scales, noting that for NGC 7469, Davies et al. (2004) report that a  $5^\circ$  change in inclination changes the dynamical mass by 17%. An effect of this size does not increase our uncertainties significantly, and so we adopt a global uncertainty of 40% on all the dynamical mass estimates.

We have plotted  $L_{HCN}$  against  $M_{dyn}$  in Figure 2.10, which shows that the relation between them is essentially linear. The bivariate regression fit (solid blue line on the figure) is given as:

$$\log L_{HCN} = (0.99 \pm 0.1) \log M_{dyn} - (1.48 \pm 0.84) \quad (2.4)$$

We find that Spearman’s rank correlation coefficient  $\rho \sim 0.90$  with 98% significance (noting that  $\rho = 1$  corresponds to two variables being monotonically related). Since we do not know the intrinsic  $L_{HCN}$  for NGC 3079, we adopt the  $S_{HCN} \Delta v$  from the absorption corrected flat-topped profile. Its  $L_{HCN}$  large uncertainty is due to the difference in flux between the observed line and the absorption corrected profile. We also looked at the surface densities for the mass and luminosity, where both axes in Figure 2.10 are divided by the best-fit model disk area. A significant correlation still exists, indicating that disk size may not influence the relation between  $L_{HCN}$  and  $M_{dyn}$ . We discuss below the implication of the mass luminosity relation in terms of the gas fraction  $f_{gas}$  and the conversion factor  $\alpha_{HCN}$  between HCN luminosity and gas mass.

For either a single virialised (gravitationally bound) cloud, or a non-overlapping ensemble of such clouds, the ratio  $\alpha_{HCN}$  between the gas mass  $M_{gas}$  and the HCN luminosity

$L_{HCN}$  (in units of  $\text{K km s}^{-1} \text{pc}^2$ ) can be written as (Solomon et al., 1990; Downes et al., 1993; Krips et al., 2008):

$$\frac{M_{gas}}{L_{HCN}} \equiv \alpha_{HCN} = 2.1 n_{H_2}^{0.5} T_b^{-1} \quad (2.5)$$

where  $n_{H_2}$  ( $\text{cm}^{-3}$ ) is the average  $\text{H}_2$  number density and  $T_b$  (K) is the brightness temperature.

However, as discussed by Downes et al. (1993) and Solomon & Vanden Bout (2005), when the line width traces the potential of a galaxy, i.e.  $\Delta v^2 = G M_{dyn}/R$ , one has to modify Equation 2.5 to account for the mass contributed by stars in addition to the gas. As we have shown in Section 2.4, this is the case for our observations of the HCN (1-0) lines; and in Section 2.7 we show that in at least one galaxy the clouds are not self-gravitating. In addition, we also note that since the HCN (1-0) transition has a critical density of  $\sim 3 \times 10^6 \text{cm}^{-3}$  (e.g. Meijerink et al. 2007), the emission traces preferentially dense gas, whereas there may also be a significant mass of gas in less dense clumps, which might instead be traced by CO (1-0) which has a much lower critical density. Following the argument given in Downes et al. (1993), the relation between dynamical mass and HCN luminosity can be expressed as:

$$\frac{M_{dyn}}{L_{HCN}} = 2.1 n_{eq}^{0.5} T_b^{-1} \quad (2.6)$$

where  $n_{eq}$  is an equivalent  $\text{H}_2$  number density. Then, since  $f_{gas} \equiv M_{gas}/M_{dyn} = n_{H_2}/n_{eq}$ , Equation 2.6 can be rewritten as:

$$\frac{M_{dyn}}{L_{HCN}} = f_{gas}^{-1/2} \alpha_{HCN} \quad (2.7)$$

That there is a relation between  $L_{HCN}$  and  $M_{dyn}$  which is close to linear, as is apparent in Figure 2.10, implies either that there is an intrinsic relation between  $f_{gas}$  and  $\alpha_{HCN}$  or that there are typical values (to within a factor of 2 or so) for both of these quantities.

Based on a variety of sources and methods, Hicks et al. (2009) argued that the typical gas mass fraction lies in the range 4–25%, with a typical value of  $f_{gas} \sim 0.1$ , within the central 200 pc of Seyferts. We adopt this value and, based on Equation 2.7, draw in Figure 2.10 the lines corresponding to  $\alpha_{HCN} = 3$  (long dash line), 10 (dot-dash line), and 25 (dotted line). We find that  $\alpha_{HCN} = 10 \text{M}_\odot (\text{K km s}^{-1} \text{pc}^2)^{-1}$  provides a remarkably good approximation to the data. A similar HCN conversion factor  $\alpha_{HCN} = 10_{-3}^{+10}$  for nearby AGN (albeit with beam sizes ranging from a few arcsec up to  $20''$ ) was found via LVG analysis by Krips et al. (2008). As they noted, it is  $\sim 2$  times smaller than the  $\alpha_{HCN} = 25$  estimated by Gao & Solomon (2004) for nearby spiral, infrared-luminous, and ultraluminous galaxies. However, Figure 2.10 rules out such a high conversion factor for the centers of AGN since it would imply a gas fraction exceeding 50%. The difference may point towards differing excitation conditions and molecular abundances in the environments, and there is plentiful theoretical and observational evidence that X-ray excitation of gas by the AGN does have

a major impact on both of these leading to an increase in the HCN luminosity (Lepp & Dalgarno, 1996; Maloney et al., 1996; Boger & Sternberg, 2005; Meijerink & Spaans, 2005; Meijerink et al., 2007; Kohno et al., 2003; Usero et al., 2004; Krips et al., 2007, 2008; Davies et al., 2012).

## 2.7 Non self-gravitating clouds in NGC 6951

In their high spatial resolution analyses of the Br $\gamma$  hydrogen recombination line in Seyferts, Davies et al. (2007) and Hicks et al. (2013) were able to show that there was no on-going star formation in the central  $\sim 100$  pc. And as part of their analysis of the HCN line kinematics, Sani et al. (2012) found that while there was often star formation occurring in circumnuclear rings at radii  $\geq 100$  pc, on smaller scales the evidence indicates that the star formation rates were much lower. Our aim in this section is to assess whether the clouds in the central region are self-gravitating. If they are not, this could be one reason why star formation appears to be suppressed on these scales.

We focus on NGC 6951 which is one of the Seyfert galaxies in the combined sample summarised in Table 2.6, and for which suitable data are available. Observations reported by Krips et al. (2007) provide the HCN (1-0)/CO (2-1) ratio, which is 2.5 (if units for line fluxes are  $\text{K km s}^{-1}$ ; it is 0.37 if the line flux units are  $\text{Jy km s}^{-1}$ ) as discussed by Davies et al. (2012). These data have similar small beams and so are spatially resolved, which is important since the distributions of the two lines are very different. Here we use the line ratio corresponding to the central component only. In addition, Krips et al. (2008) reported the HCN (3-2)/HCN (1-0) line ratio as 0.4 corrected for beam filling factors. Although the beam for these data is larger (and specifically, the HCN (1-0) measurement used for this line ratio is a single dish measurement rather than the interferometric measurement used for the other line ratio), it is less critical since both lines are from HCN and so are expected to have more similar distributions. Since the beam includes the circumnuclear ring, there is some uncertainty associated with whether the line ratio reflects that in the nucleus. However, a similar measurement by Krips et al. (2008) on NGC 1068 with a smaller beam that probes only regions well within the circumnuclear ring, yielded a HCN (3-2)/HCN (1-0) ratio of 0.21 (as such, given the HCN (1-0)/CO (2-1) ratio from Usero et al. (2004) discussed by Davies et al. 2012, the analysis below could equally apply to NGC 1068); and a ratio of 0.15 has been reported for the nucleus of NGC 1097 by Hsieh et al. (2012). While these two galaxies could also be used for this analysis, we have not included them here. This is partly because they are not part of our combined sample. For NGC 1068 it is also because the nuclear region of NGC 1068 is very complex, having a circumnuclear bar feeding gas in to the nucleus while an outflow from the AGN disrupts the disk (Müller Sánchez et al. 2009; Krips et al. 2011; García-Burillo et al. 2014). For NGC 1097, it is also because the AGN is very weak and cannot really be classified as a Seyfert. As can be seen in Figure 2.11 even a large uncertainty in the HCN (3-2)/HCN (1-0) ratio does not alter the general conclusion that the clouds cannot be self-gravitating.

In order to derive the physical conditions under which these line ratios can arise, we

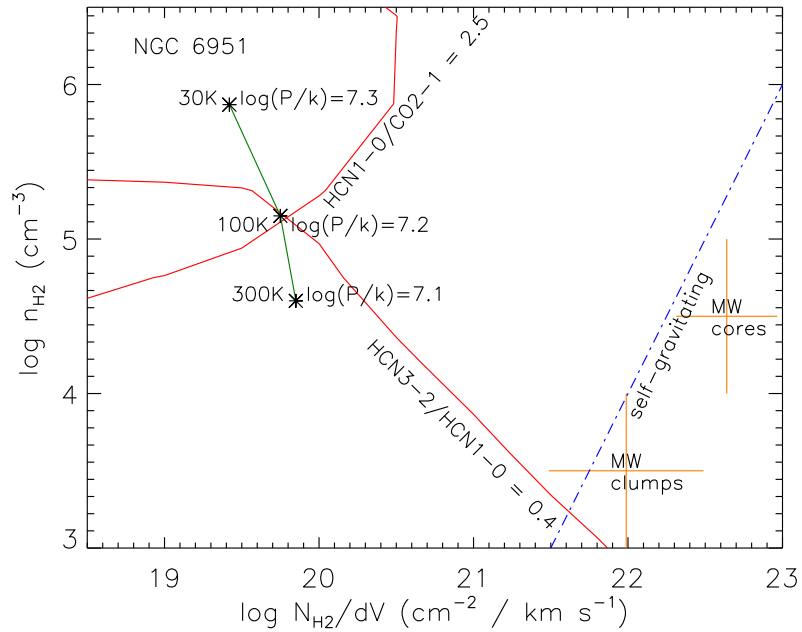


Figure 2.11: Part of the 4-dimensional parameter space for LVG calculations. In this plane, the dot-dash blue line indicates the boundary for self-gravitating clouds; clumps and cores of Milky Way clouds are located to the right of this (Bergin & Tafalla, 2007). Red lines tracing the HCN(1-0)/CO(2-1) and HCN(3-2)/HCN(1-0) ratios in the centre of NGC 6951 have been drawn for  $\log X_{\text{HCN}}/X_{\text{CO}} = -2$  and a temperature of 100 K (see Davies et al. 2012). These lines intersect at a point where the implied pressure in the cloud is  $\log P/k [\text{cm}^{-3}\text{K}] = 7.2$ . Due to the well known degeneracy between density and temperature, these two parameters cannot be fully constrained. But the intersection of lines tracing the two ratios are also shown for temperatures in the range 30–300 K (asterisks joined by solid green lines), and show that the cloud density is likely to be  $\log n [\text{cm}^{-3}] = 4.5\text{--}6$  and that over this range the pressure in the clouds remains high and roughly constant. Since all the intersections (marked by asterisks) are far to the left of the locus for self-gravitating clouds, the clouds in NGC 6951 must be pressure confined rather than self-gravitating.

make use of the Large Velocity Gradient (LVG) approximation (Sobolev, 1957), which has been widely used in the literature to study gas conditions and excitation in normal and active galaxies. It is important to realise that LVG calculations apply to individual clouds. On the other hand, the observations we use are of an ensemble of clouds. However, under the usual assumption that all the clouds in the ensemble are the same, the line ratios will not depend on the number of clouds: they will be the same for a single cloud and for the ensemble. We note, however, that this is not the case for the line width, which is very different for a single cloud and for the ensemble. As such, to interpret the modelled ratio  $N_{H_2}/dV$ , or equivalently  $n_{H_2}/(dV/dr)$ , in the context of the observations would require additional assumptions that one sees all the clouds and that their individual line profiles and relative velocities combine to match the observed line profile. However, our results are not affected by this issue because our comparison of the LVG calculations to observations is based solely on line ratios.

We use the LVG calculations performed by Davies et al. (2012) (we refer to that paper for details of the code and comparison to the commonly used RADEX) and extended them to include the HCN (3-2)/HCN (1-0) line ratio. The calculations cover a wide range of parameters: kinetic temperature  $30 \leq T [K] \leq 300$ , HCN to CO abundance ratio  $10^{-5} \leq X_{HCN}/X_{CO} \leq 10^{-2}$  (with  $X_{CO} = 10^{-4}$  as the CO abundance relative to hydrogen),  $H_2$  volume gas density  $10^3 \leq n_{H_2} [cm^{-3}] \leq 10^7$ , and a ratio of gas-density to velocity-gradient, or equivalently column density to linewidth, of  $5 \times 10^{17} \leq N_{H_2}/dV [cm^{-2} (km s^{-1})^{-1}] \leq 5 \times 10^{23}$ . One plane of this parameter space is shown in Figure 2.11.

For reference, we show the boundary (dot-dash blue line), to the right of which clouds are self-gravitating (see Goldsmith 2001 and Davies et al. 2012). For virialised clouds  $\Delta V/R \sim n^{0.5}$  where  $\Delta V$  is the velocity dispersion,  $R$  is the cloud radius, and  $n$  is the gas volume density. The self-gravitating boundary line is found by treating  $\Delta V/R$  as a velocity gradient, which gives  $dV/dr \propto n_{H_2}^{0.5}$  as shown.

We have also marked the regions where one expects to find Galactic clumps and cores, using the typical properties summarised by Bergin & Tafalla (2007) and estimating  $N_{H_2}/dV$  from their density, size, and velocity width. Galactic clouds, with densities of  $n_{H_2} = 50\text{--}500 cm^{-3}$ , are outside the range of the plot. Their sizes of 2–15 pc and velocity widths of 2–5 km s<sup>-1</sup> indicate they have  $\log N_{H_2}/dV \sim 20.9$  and so lie just left of the extension of the self-gravitating line.

We now discuss how, although the LVG calculation formally has 5 free parameters, we can reach a robust conclusion with only 2 line ratios. The first parameter is the CO abundance  $X_{CO}$ , but because this hardly varies for a wide variety of conditions we fix it at  $X_{CO} = 10^{-4}$ . The HCN abundance  $X_{HCN}$  is also a parameter. But it was already shown by Davies et al. (2012) that the HCN (1-0)/CO (2-1) ratio alone requires an unusually high HCN abundance,  $X_{HCN} \geq 10^{-6}$ . Since this is already much higher than the typical abundance, although still consistent with what one might expect theoretically from calculations of equilibrium abundances in X-ray irradiated gas (Boger & Sternberg, 2005), we fix it at  $X_{HCN} = 10^{-6}$ . The volume density  $n_{H_2}$  and ratio of column density to linewidth  $N_{H_2}/dV$  are the axes of the plot and therefore left as free parameters. Finally, the temperature  $T$  is unconstrained. We have therefore plotted red curves tracing the locus of the line ratios

above for NGC 6951 assuming a temperature of 100 K; and show in addition the location where the two curves intersect for temperatures of 30 K and 300 K (asterisks joined by the green curve), a range that covers the temperatures one might expect to find in the central regions of Seyferts (Krips et al., 2008). This shows the well known degeneracy between temperature and density, but also indicates that, unless the temperature of the molecular gas significantly exceeds 300 K, the gas density must be  $\log n_{H_2} [cm^{-3}] \geq 4.5$ .

One very clear conclusion from the figure is that, independent of temperature and density, the locus of intersections for the line ratios lies far to the left of the region where one finds self-gravitating clouds. Indeed, for the range of temperatures we have considered, the inferred pressure is roughly constant at  $P/k = (1 - 2) \times 10^7 cm^{-3} K$  suggesting that the clouds are likely to be pressure confined. A similar conclusion was reached by Zaragoza-Cardiel et al. (2014) for H II regions and giant molecular clouds in the interacting Antennae galaxy system: self-gravity only bound clouds above a certain mass threshold, and below this they must be bound by external pressure. Intriguingly the pressure we find is comparable to that found by Heckman et al. (1990) in the central few hundred parsecs of galaxies with starburst driven superwinds. As such, the line ratios observed in the centre of NGC 6951 are consistent with an environment dominated by supernovae, perhaps indicative of a young post-starburst.

## 2.8 Conclusion

We have presented 3 mm interferometer data from the IRAM PdBI, which spatially resolves the HCN (1-0) and HCO<sup>+</sup> (1-0) molecular lines in the central few arcsecs of three nearby Seyfert galaxies: NGC 3079, NGC 6764, and NGC 5033. The main results of this study are as follows:

1. For these galaxies, and also NGC 7469, we use a rotating disk model that takes into account beam smearing, to successfully match the observed line distribution and kinematics. The characteristics of NGC 5033 can be fitted by a thin disk having  $\sigma/v < 0.1$ . In contrast NGC 7469, NGC 3079, and NGC 6764 all favour a thick disk with  $\sigma/v > 0.3$ . Combining these results with the earlier study of Sani et al. (2012), we find that in 7 out of 8 Seyferts, the HCN (1-0) line traces thick rather than thin disks in the central  $\sim 100$  pc.
2. The spectrum of NGC 3079 is dominated by numerous absorption lines, which are characterised by a double peak profile. The component closest to systemic is caused by absorption in the approaching side of the inner disk, which lies in front of a radio continuum knot in the north-west jet. Based on the depth of the H<sup>13</sup>CN (1-0) feature (since H<sup>12</sup>CN (1-0) is both saturated and blended with emission), we estimate the hydrogen column density in the disk to be  $N_H \sim 6 \times 10^{22} cm^{-2}$ . The other absorption component, with a broad blue-shifted wing extending to  $-350 km s^{-1}$ , suggests the existence of a dense nuclear outflow. Correcting the HCN (1-0) and HCO<sup>+</sup> (1-0)

lines for continuum absorption indicates that the emission lines are also partially self-absorbed.

3. We find a relation between HCN luminosity and dynamical mass. This implies either a relation between, or typical values for, the gas fraction and the conversion factor  $\alpha_{HCN}$  between HCN luminosity and gas mass. A gas fraction of  $f_{gas} \sim 0.1$  and  $\alpha_{HCN} \sim 10$  (consistent with the conclusion of Krips et al. 2008 from LVG calculations) can account for the observed relation.
4. An analysis of the HCN (1-0)/CO (2-1) and HCN (3-2)/HCN (1-0) line ratios in NGC 6951 indicates that the molecular gas is not in self-gravitating clouds. Instead, the clouds are likely to be pressure confined. The implied pressure of  $P/k \sim 10^7 \text{ cm}^{-3} \text{ K}$  is comparable to that measured in the centers of superwinds, suggesting that the interstellar medium in the centre of NGC 6951 is consistent with an environment dominated by supernova.



# Chapter 3

## Luminous Local AGN with Matched Analogues (LLAMA): Nuclear stellar properties of Swift BAT AGN and matched inactive galaxies

*This chapter is a reprint of*

*Ming-Yi Lin, R.I. Davies, E.K.S. Hicks, L. Burtscher, A. Contursi, R. Genzel, M. Koss, D. Lutz, W. Maciejewski, F. Müller-Sánchez, G. Orban de Xivry, C. Ricci, R. Riffel, R.A. Riffel, D. Rosario, M. Schartmann, A. Schnorr-Müller, T. Shimizu, A. Sternberg, E. Sturm, T. Storchi-Bergmann, L. Tacconi and S. Veilleux*

*MNRAS submitted*

### 3.1 Introduction

It is widely accepted that most galaxies harbor a supermassive black hole (SMBH). The remarkable of BH observations are the ones in our Galaxy; the individual stars can be spatially resolved and followed through their orbits, giving the constraint on the SMBH mass (see a review by Genzel et al., 2010). Beyond the Milky Way, the most compelling evidence is the correlation between the mass of SMBH and stellar velocity dispersion of the bulge component of the host galaxy, which is interpreted as the signature of coevolution and regulation between the SMBH and the bulge (see Kormendy & Ho, 2013 and the reference therein). The SMBH grows via inflowing gas accretion, resulting in active galactic nuclei (AGN), which have been observed across different cosmic times. The host galaxy growth typically follows two plausible modes (Shlosman, 2013): (i) galaxy merger: angular momentum dissipation leads the gas infall forming compact young stars in the host galaxy (Holtzman et al., 1992; Hopkins et al., 2009), and furthermore efficiently drives some amount of gas to feed the central SMBH. Examples of this include the ultra-luminous infrared bright galaxies with disturbed host galaxy morphologies, which are

usually accompanied by a QSO-like luminous AGN (Bennert et al., 2008; Veilleux et al., 2009; Teng & Veilleux, 2010; Ricci et al., 2017). (ii) Secular process of cold gas inflow: gas transfers from outer host galaxy to inner circumnuclear regions through disk and bar instabilities. If a bar drives the gas inflow, the associated inner Lindblad resonance (ILR) may terminate the inflowing gas and redistribute it in a disk inside the ILR radius (see Combes 2001 and references therein). However, Haan et al. (2009) studied gravitational torques and concluded that such dynamical barriers can be easily overcome by gas flows from other non-axisymmetric structures. The direct observations of inflows in an ionized or warm molecular gas phase on  $\sim 100$  pc scales have been confirmed in nearby Seyferts (e.g. Storchi-Bergmann et al. 2007; Müller Sánchez et al. 2009; Davies et al. 2014; Riffel et al. 2013; Storchi-Bergmann 2014; Schnorr-Müller et al. 2017).

The studies above focus on the question of the origin of inflowing gas transport (e.g. ex-situ gas). Once the gas accumulates in the nuclear regions, we further want to know whether any in-situ star formation occurs. Some observations indicate on-going star formation in the nuclear region (Esquej et al., 2014; Riffel et al., 2009) while others point out the galaxies prefer to have post-starburst populations (Cid Fernandes et al., 2004; Davies, 2007; Sani et al., 2012; Lin et al., 2016). Hicks et al. (2013) also find no evidence that on-going star formation is happening in the central 100 pc. Observationally, it is unclear whether nuclear star formation plays a decisive role in triggering nuclear activity. While it is understood that AGN flicker on and off on very rapid timescales, a recent analysis points to  $10^5$  years as one timescale (Schawinski et al., 2015); longer duty cycles of  $10^{7-9}$  years corresponding to the lifetime of a typical AGN phase are superimposed on top of that (Marconi et al., 2004). This means that focussing on the circumnuclear regions of galaxies (e.g. Dumas et al. 2007; Hicks et al. 2013; Davies et al. 2014) where dynamical timescales are of order  $10^6$  years and star formation timescales are  $10^6-10^8$  years, is an appropriate strategy to study the feeding mechanisms of gas flows associated with AGN activity. To address this issue comprehensively, Davies et al. (2015) built a near complete volume limited sample of 20 nearby active galaxies, which was complemented by a matched sample of inactive galaxies, with the aim to obtain high spatial resolution near-infrared observations with SINFONI together with high spectral resolution observations taken with XSHOOTER. This is the LLAMA (Luminous Local AGN with Matched Analogues) survey which has been the focus of several other studies (Schnorr-Müller et al. 2016; Davies et al. 2017, Rosario et al. submitted, Burtscher et al. in prep.).

In this paper, we present the SINFONI H+K observations probing radial scales of  $\sim 150$  parsec for the first half of the AGNs from Davies et al. (2015), and their corresponding inactive galaxies which are matched in stellar mass, morphology, inclination, and the presence of a bar. This contains a total of 13 galaxies, 8 AGNs and 5 inactive galaxies, which provide 8 pairs (since some inactive galaxies can be well matched to more than one AGN). In this study, because the sample number is small, when comparing a difference between active and inactive sample for any physical quantity, we directly compare the mean value and standard deviation rather than giving a statistical test. In Section 3.2, we introduce the observations and data reduction of all the galaxies. Section 3.3 describes the methodology to extract the stellar kinematics and constrain the bulge Sérsic parameters. The nuclear

stellar photometry is in Section 3.4, while the nuclear stellar kinematics is presented in Section 3.5. We summarize our conclusions in Section 3.6. Throughout this paper, we focus the discussion on the overall kinematic and photometric properties of the active and inactive samples. A detailed descriptions of individual objects with special (or extreme) properties will be discussed throughout this paper. We assume a standard  $\Lambda$ CDM model with  $H_0 = 73 \text{ km s}^{-1} \text{ Mpc}^{-1}$ ,  $\Omega_\Lambda = 0.73$  and  $\Omega_M = 0.27$ .

## **3.2 Sample selection, observations and data reduction**

Table 3.1: Galaxy Properties: (1) Pair ID (a – AGN, i – inactive galaxy); (2) galaxy name; (3) AGN classification; (4) Hubble type of host galaxy; (5) Presence of large-scale bar (B indicates a bar, AB a weak bar); (6) Stellar mass estimated from total 2MASS H-band luminosity; (7)  $m_K$ (nucleus), apparent K-band magnitude measured from SINFONI data cube within  $3''$  aperture size; (8) Large scale axis ratio (from NED or Koss et al. 2011); (9) Inclination derived from axis ratio; (10) Distance (the median value of redshift-independent distance measurements from NED); (11) Physical scale of  $1''$  (from NED); (12) Observed 14-195 keV luminosity (70 months average) from *Swift*-BAT catalog (Baumgartner et al., 2013).

(1)	(2)	(3)	(4)	(5)	(6)	(7)	(8)	(9)	(10)	(11)	(12)
Pair ID	Galaxy name	AGN	Hubble type	Bar	$M_*$ ( $M_\odot$ )	$m_K$ (mag)	a/b	Incl. ( $^\circ$ )	Distance (Mpc)	scale (pc $''$ )	$\log(L_{14-195keV})$ (erg s $^{-1}$ )
1a	ESO 137-34	Sey 2	S0/a	AB	10.4	11.9	0.79	40	33	185	42.62 $^\dagger$
6a	NGC 3783	Sey 1.2	Sab	B	10.2	10.2	0.89	27	48	212	43.49
7a	NGC 4593	Sey 1	Sb	B	10.5	11.1	0.74	42	32	200	43.16
4a	NGC 5728	Sey 2	Sb	B	10.5	11.6	0.57	55	30	199	43.21 $^\dagger$
8a	NGC 6814	Sey 1.5	Sbc	AB	10.3	11.0	0.93	22	23	89	42.69
3a	NGC 7172	Sey 2	Sa		10.4	10.1	0.56	60	34	153	43.45
2a	NGC 7213	Sey 1	Sa		10.6	10.2	0.90	26	22	102	42.50
5a	NGC 7582	Sey 2	Sab	B	10.3	9.7	0.42	65	22	88	42.67 $^\dagger$
6i	NGC 718	-	Sa	AB	9.8	11.2	0.87	30	22	96	-
7i	NGC 3351	-	Sb	B	10.0	11.6	0.93	22	10	74	-
3i, 5i	NGC 4224	-	Sa		10.4	11.8	0.35	70	45	193	-
8i	NGC 4254	-	Sc		10.2	12.0	0.87	30	16	75	-
1i, 2i, 4i	NGC 7727	-	Sa	AB	10.4	10.8	0.74	42	27	100	-

$^\dagger$ : Heavily obscured AGNs with  $N_H$ (column density of neutral hydrogen)  $\geq 10^{24}$  cm $^{-2}$ , which is based on C. Ricci et al. (2017, in preparation) modelling 0.3-150 keV spectrum.

### 3.2.1 Matched Seyfert and inactive galaxy sample

The sample is drawn from the LLAMA (Local Luminous AGN with Matched Analogues) project, the selection details and the scientific rationale for which have been described in Davies et al. (2015). We briefly address and discuss the key aspects of our target strategy:

1. *Select AGNs from the 58-month Swift-BAT catalog:*

The *Swift* Burst Alert Telescope (BAT) all-sky hard X-ray survey is a robust tool for selecting AGN, because it is based on observations in the 14-195 keV band. Emission in this band is generated close to the SMBH and can penetrate through foreground obscuration. In contrast to optical/near-infrared AGN classification techniques, hard X-ray surveys suffer little contamination from non-nuclear emission. However, it is still biased against extremely obscured Compton-thick sources ( $N_H \geq 10^{25} \text{ cm}^{-2}$ , Ricci et al., 2015; Koss et al., 2016) where the hard X-ray photon attenuation is due to Compton scattering on electrons rather than photoelectric absorption. In order to create a complete, volume-limited sample of nearby bright hard X-ray selected AGNs, the selection criteria were solely (i) 14-195 keV luminosities:  $\log L_{14-195} > 42.5$  (using redshift distance), (ii) redshift:  $z < 0.01$  (corresponds to a distance of  $\leq 40$  Mpc), and (iii) observable from the VLT ( $\delta < 15^\circ$ ). The total sample contains 20 AGNs covering Seyfert 1, Seyfert 2, and intermediate Seyfert types. Classifications are based on NED<sup>1</sup>, with additional information from the presence of near-infrared broad lines or polarized broad line emission, as well as the first spectroscopic data from the LLAMA survey itself.

2. *Finding a matched sample of inactive galaxies:*

Studying the difference between Seyferts and inactive galaxies can provide a direct comparison and give clues to understand what mechanisms can fuel central BH and how the gas flows (inflows or outflows) interact with the interstellar medium. However, it is important that the inactive galaxies are well matched. To achieve this, the inactive galaxies in LLAMA are selected as specific pairs to the AGN. The criteria to select an inactive galaxy for each AGN are based on: host galaxy morphology (Hubble type), inclination (axis ratio), and Two Micron All Sky Survey (2MASS) H-band luminosity (the proxy of stellar mass). Figure 3 in Davies et al. (2015) shows that there is no significant difference in the distribution of host galaxy properties between the *Swift*-BAT AGN sample and the matched inactive sample, except the distance distribution, the active galaxies being slightly more distant than the inactive pairs. We also note that the presence of large scale bar is matched if possible, but is not strictly necessary. A large scale bar in the host galaxy is an efficient way to drive some gas into the central region (Buta & Combes, 1996). However, numerous studies have found that the bar fraction in Seyfert and inactive galaxies is similar, suggesting that while large scale bars may assist in fuelling SMBH growth they are

---

<sup>1</sup><https://ned.ipac.caltech.edu/>

unlikely to be the sole mechanism regulating it (Mulchaey & Regan, 1997; Cisternas et al., 2015). Our total sample contains 19 matched inactive galaxies.

This project includes observations from the high resolution spectrograph XSHOOTER covering 0.3-2.3 $\mu$ m (Schnorr-Müller et al. 2016, and Burtscher et al. in prep) and adaptive optics near-infrared integral field spectroscopy covering 1.8-2.4 $\mu$ m taken with SINFONI (this paper and Lin et al. in prep). The two independent sets of observations and analyses allow us to approach, from two different perspectives, one of the primary science goals of the overall project: looking for evidence of young or recent stellar populations (stellar age of a few to a few hundred Myr) related to AGN accretion. The properties of the sample galaxies analysed in this paper are listed in Table 3.1.

### 3.2.2 Observations and standard data reduction

We present the first part of near-infrared IFU data for the LLAMA project. Eight AGNs and five matched inactive galaxies have been observed with SINFONI between 2014 April and 2015 June from programme 093.B-0057. In total, this provides eight Seyfert-inactive galaxy pairs because, by relaxing slightly the matching criteria, some inactive galaxies provide a good match to several AGN. Specifically, NGC 7727 and NGC 4224 are the inactive pair of three and two AGNs respectively. SINFONI, installed at the Cassegrain focus of VLT-UT4, consists of the Spectrometer for Infrared Faint Field Imaging (SPIFFI), a NIR cryogenic integral field spectrometer with a HAWAII 2RG (2k $\times$ 2k) detector and an adaptive optics (AO) module, Multi-Application Curvature Adaptive Optics (MACAO) (Eisenhauer et al., 2003; Bonnet et al., 2004).

We observe each galaxy with the H+K grating at a spectral resolution of  $R \sim 1500$  for each 0".05 $\times$ 0".1 spatial pixel, leading to a total field of view (FOV) on the sky of 3" $\times$ 3". All scientific objects were observed in AO mode, either using a natural guide star (NGS) or an artificial sodium laser guide star (LGS). For our observations to achieve the best correction with a NGS, it should be brighter than  $R \sim 15$  mag and within a distance of 10" from the scientific object. During such observations, the typical Strehl ratio achieved was  $\sim 20\%$ . A standard near-infrared nodding technique with an observation sequence of Object-Sky-Object was applied. In each observing block (OB), a total of three sky and six on-source exposures of 300 sec each were obtained, the on-source frames being dithered by 0.3" and the sky frames offset by 60-100". Data from several OBs were combined to make the data cube. Telluric stars were observed at similar airmass, either before or after each observing block to make sure they sample similar atmospheric conditions. The data were reduced using the SINFONI custom reduction package SPRED (Abuter et al., 2006), which includes the typical reduction steps used for near-infrared spectra with the additional routines to reconstruct the data cube. The standard reduction procedure comprises flat fielding, identifying bad/hot pixels, finding slit position, correcting optical distortion and wavelength calibration. The night-sky OH airglow emission have been removed by using the methods described by Davies (2007). The telluric and flux calibrations for the scientific data were carried out with B-type stars. In our observing strategy, there are at least two

data sets for each standard star. We apply the same data processing procedure to standard star observations, and use these to make a single flux calibration to each science data set. The final flux calibration for both the H-band and K-band is accurate to  $\pm 0.05$  mag.

### 3.2.3 Differential atmospheric refraction

To improve the image quality in SINFONI data cubes, we quantify the displacements induced by differential atmospheric refraction (DAR), which appears as a spatial offset of the observed object as a function of wavelength. The refraction is due to the Earth's atmosphere causing the light to deviate from its original trajectory and appear closer to the zenith by an amount that is dependent on wavelength. The DAR will be more important for observations with larger zenith distance, i.e. higher air mass. In principle, the DAR effect is stronger in the optical and, for seeing limited observations, can usually be ignored in the near-infrared. However, with adaptive optics on large telescopes, the impact of DAR relative to the spatial resolution is more significant. We correct DAR using standard analytical expressions based on a simple model of the atmosphere. And we include a description here of our method because it differs from the empirical method outlined by Menezes et al. (2015).

An object at an actual zenith distance of  $z$ , has an apparent zenith distance  $\zeta$  after the light has passed through the atmosphere. The refraction angle is  $R = z - \zeta$ , and can be written as:

$$R = 206265 \times (n - 1) \times \tan \zeta \quad (3.1)$$

where  $R$  is in arcsec and  $n$  is the refraction index close to Earth's surface.

Assuming standard atmospheric conditions, a temperature  $T = 20^\circ\text{C}$ , an atmospheric pressure  $P = 10^5$  Pa, and  $\text{CO}_2$  fraction of 0.0004 with low humidity, the refraction index  $n_{20,10^5}$  is expressed as a function of wavelength (Bönsch & Potulski, 1998; Filippenko, 1982)

$$(n_{20,10^5}(\lambda) - 1) \times 10^8 = 8091.37 + \frac{2333983}{130 - (\frac{1}{\lambda})^2} + \frac{15518}{38.9 - (\frac{1}{\lambda})^2} \quad (3.2)$$

where  $\lambda$  is wavelength in  $\mu\text{m}$ . To take into account the variation of  $T$  and  $P$  between the various observations, the refraction index  $n_{T,P}(\lambda)$  can be written as

$$(n_{T,P}(\lambda) - 1) = (n_{10^5,20}(\lambda) - 1) \times$$

$$\frac{P \times [1 + (0.5953 - 0.009876 \times T) \times 10^8 \times P]}{93214.6 \times (1 + 0.003661 \times T)} \quad (3.3)$$

If including the vapour pressure of water, the equation above is reduced by a factor of  $f$ :

$$n_{T,P,f}(\lambda) = n_{T,P}(\lambda) - f \times \left(3.8020 - \frac{0.0384}{\lambda^2}\right) \times 10^{-10} \quad (3.4)$$

where  $f$  is measured in Pa (the empirical relation between the change of refractive index and water vapour pressure refer to Figure 4 of Bönsch & Potulski (1998)):

$$f = \exp\left(20.386 - \frac{5132}{273 + T}\right) \times 133.32$$

Combing the equation(3.1) and (3.4) allows one to find the wavelength dependent differential refraction at constant  $\zeta$ :

$$\Delta R = 206265 \times (n_{T,P,f}(\Delta\lambda)) \times \tan \zeta \quad (3.5)$$

In most cases, the observed shift of the image with wavelength was reasonably well approximated by this analytical expression, although there were a few cases where the match was not so good. Figure 2 in Menezes et al. (2015) shows some examples in which there are additional offsets that cannot be interpreted as DAR. The foreground obscurations (dust filaments or dust lanes crossing the nuclear regions) can cause the peak in the H-band image slightly deviated from the nucleus position of K-band image (Mezcua et al., 2016). In order to keep this intrinsic measurement, in this work, we correct only the displacements induced by DAR, the residual offset is typically small, the average offset in K-band being only  $\sim 0.5$  pixels relative to H-band.

## 3.3 Analysis methods

### 3.3.1 Stellar distribution and kinematics

In all 13 galaxies, the first two CO absorption bandheads are well detected. The stellar kinematics is extracted by fitting the first of these, the CO(2-0) absorption at  $2.2935\mu\text{m}$ , which has better signal-to-noise ratio (S/N) and less contamination by other absorption and emission lines. The second CO(3-1) absorption bandhead at  $2.3227\mu\text{m}$  is excluded from the fit since it is contaminated by the coronal line [Ca VIII]  $2.3213\mu\text{m}$  in AGN. In order to ensure that the active and inactive galaxies have a consistent analysis, we fit the kinematics using on the CO(2-0) bandhead. To improve the S/N of the K-band continuum to 50, and simultaneously preserve the two-dimension (2D) kinematics, we have smoothed each slice of the IFU data cube. This is done by convolving with a point spread function (PSF) that has a FWHM of 3 pixels, matching that achieved on the brightest Seyfert nucleus of NGC 3783 in the same run. To fit each galaxy spectrum in our binned data cubes, we use the direct pixel fitting code Penalized Pixel-Fitting (pPXF) developed by Cappellari & Emsellem (2004). We choose the GNIRS sample of Gemini NIR late-type stellar library (Winge et al., 2009), which contains 30 stars with stellar type ranging from F7III to M2III and spectral resolution of  $3.4\text{\AA}$  ( $\sigma \sim 19\text{ km s}^{-1}$ ). To have the same spectral resolution between the stellar library and SINFONI, the stellar templates have been convolved with the instrument's line spread function of  $70\text{ km s}^{-1}$ , which is measured from the OH sky lines in K-band. To obtain the line-of-sight velocity distribution (LOSVD) of each galaxy spectrum, the stellar templates are shifted to the systematic velocity and convolved with a

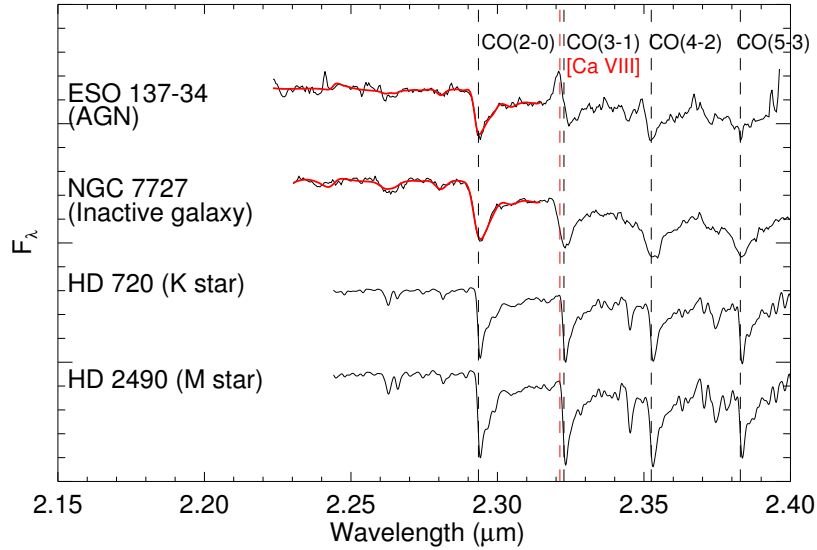


Figure 3.1: The CO absorption features of one active and one inactive galaxy observed with SINFONI/VLT (top two spectra), and stellar templates from GNIRS/Gemini convolved to the resolution of SINFONI (bottom two spectra). Each spectrum has been corrected for systematic velocity and is shown at rest-frame wavelength. The top spectrum is the sum within the AGN-dominated region, and the non-thermal continuum has been removed by a polynomial function. The coronal line [Ca VIII]  $2.3213\mu\text{m}$  is blended with CO(3-1)  $2.3227\mu\text{m}$ . The red solid lines for ESO 137-34 (AGN) and NGC 7727 (inactive galaxy) are the example ppxf kinematic fits of the CO(2-0) absorption.

Gaussian broadening function. A polynomial function of fourth order is added to take into account the power-law continuum from AGN. Unlike the stellar absorption in the optical wavelengths which often have a higher  $S/N \geq 50$  (e.g. Ca II triplet lines measured by Riffel et al. 2015), the CO(2-0) absorption in the near-infrared has lower  $S/N$  of  $\sim 10$  per spatial element. We thus do not fit higher-order moments of the Gauss-Hermite series, the h3 and h4 terms, which indicate asymmetric deviation and peakiness of the profile respectively (van der Marel & Franx, 1993; Bender et al., 1994). Examples of fits and the smoothed stellar templates are shown in Figure 3.1. We apply this fitting procedure to the whole sample across the whole FOV to extract the 2D kinematics. The results will be discussed in Section 3.5.

The resulting maps showing the flux distribution of the stellar continuum, CO(2-0) equivalent width (EW), stellar velocity, and stellar velocity dispersion are shown for the AGNs and inactive galaxies in Figure 3.2-3.3 and Figure 3.4 respectively.

### 3. LLAMA: Nuclear stellar properties of Swift BAT AGN and matched inactive galaxies

62

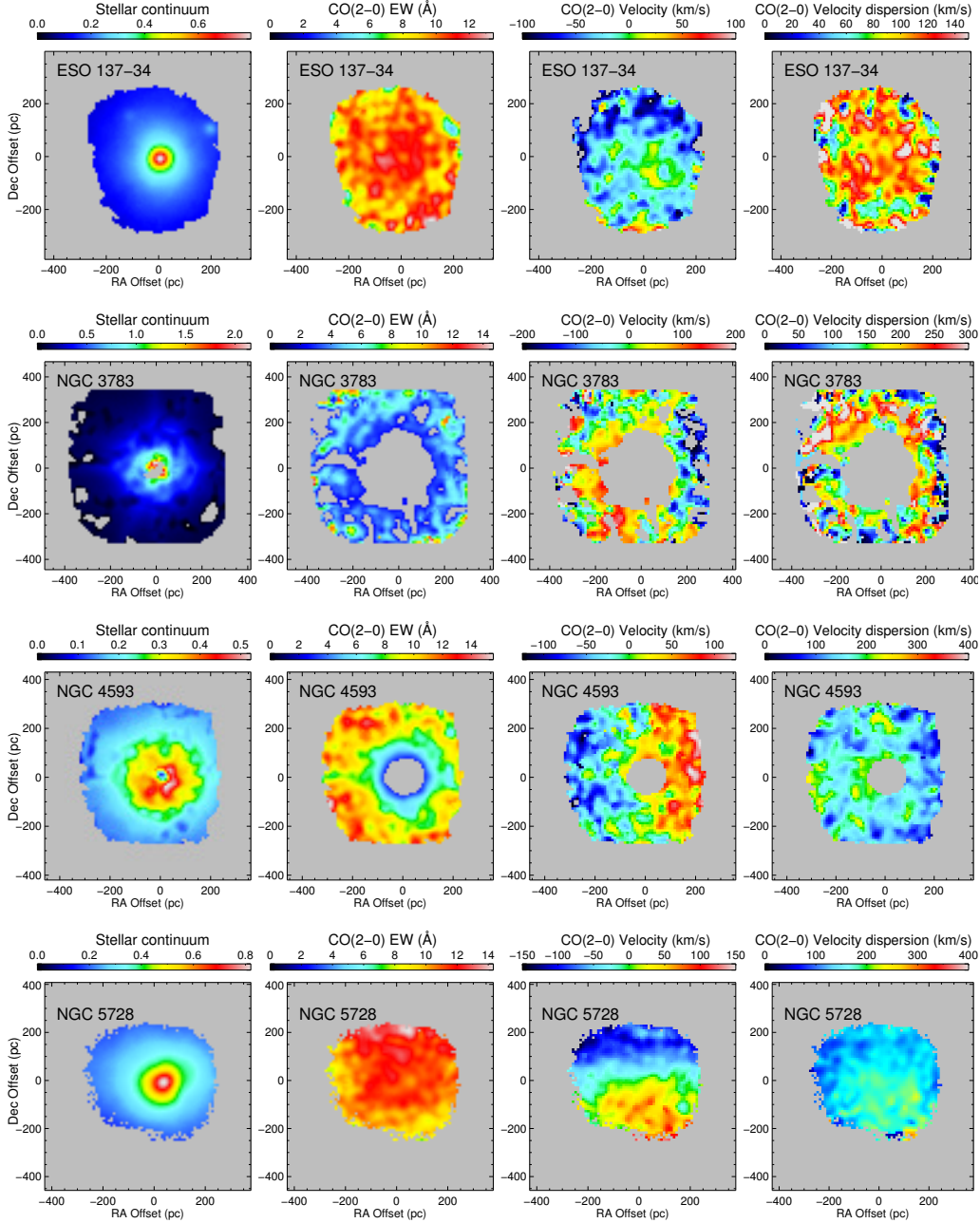


Figure 3.2: Active galaxy sample. Maps are labeled from left to right: stellar continuum flux, CO(2-0) equivalent width (EW), stellar velocity, and stellar velocity dispersion. The stellar continuum flux has been corrected for the contribution from non-stellar emission. In CO EW map, the central vacant hole is the region dominated by non-stellar emission that the ppxf program returns a unreliable kinematic measurement. We truncate it for display purposes. Because there is not non-stellar continuum dilution on stellar features for ESO 137-34 and NGC 5728, we do not outline any vacant hole in the centre. In all maps, north is up and east is to the left, the coordinate offset has been converted into the physical scale in parsec.

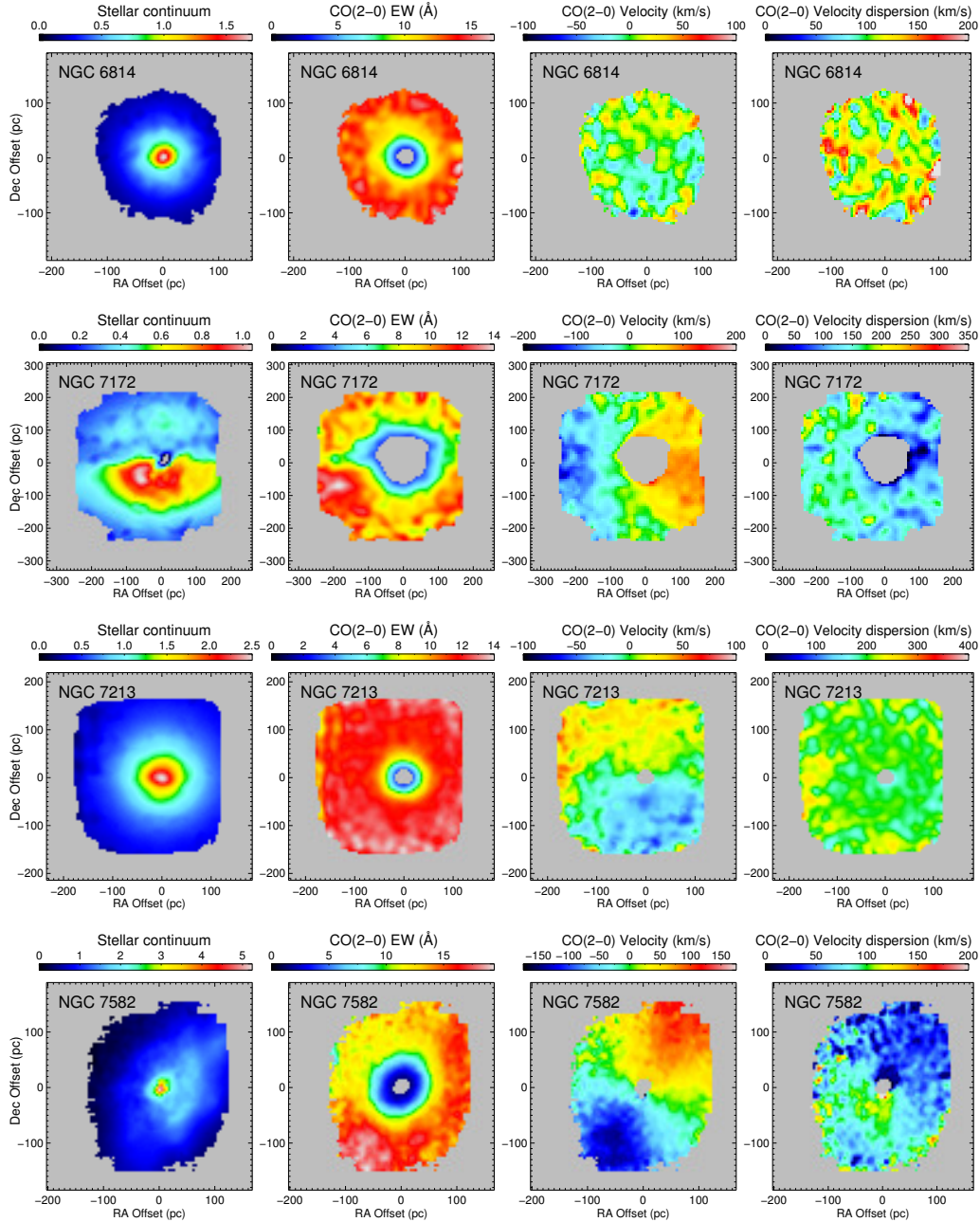


Figure 3.3: *continued*. The extreme irregularity in stellar continuum for NGC 7172 and NGC 7582 is due to the asymmetric reddening induced by dust lane, which passes through their nuclear region. The dust lane extinction does not influence the kinematic measurement. Although NGC 6814 is a face-on system, the weak rotation still is apparent from the map, consistent with the stellar velocity map of Davies et al. (2014).

### 3. LLAMA: Nuclear stellar properties of Swift BAT AGN and matched inactive galaxies

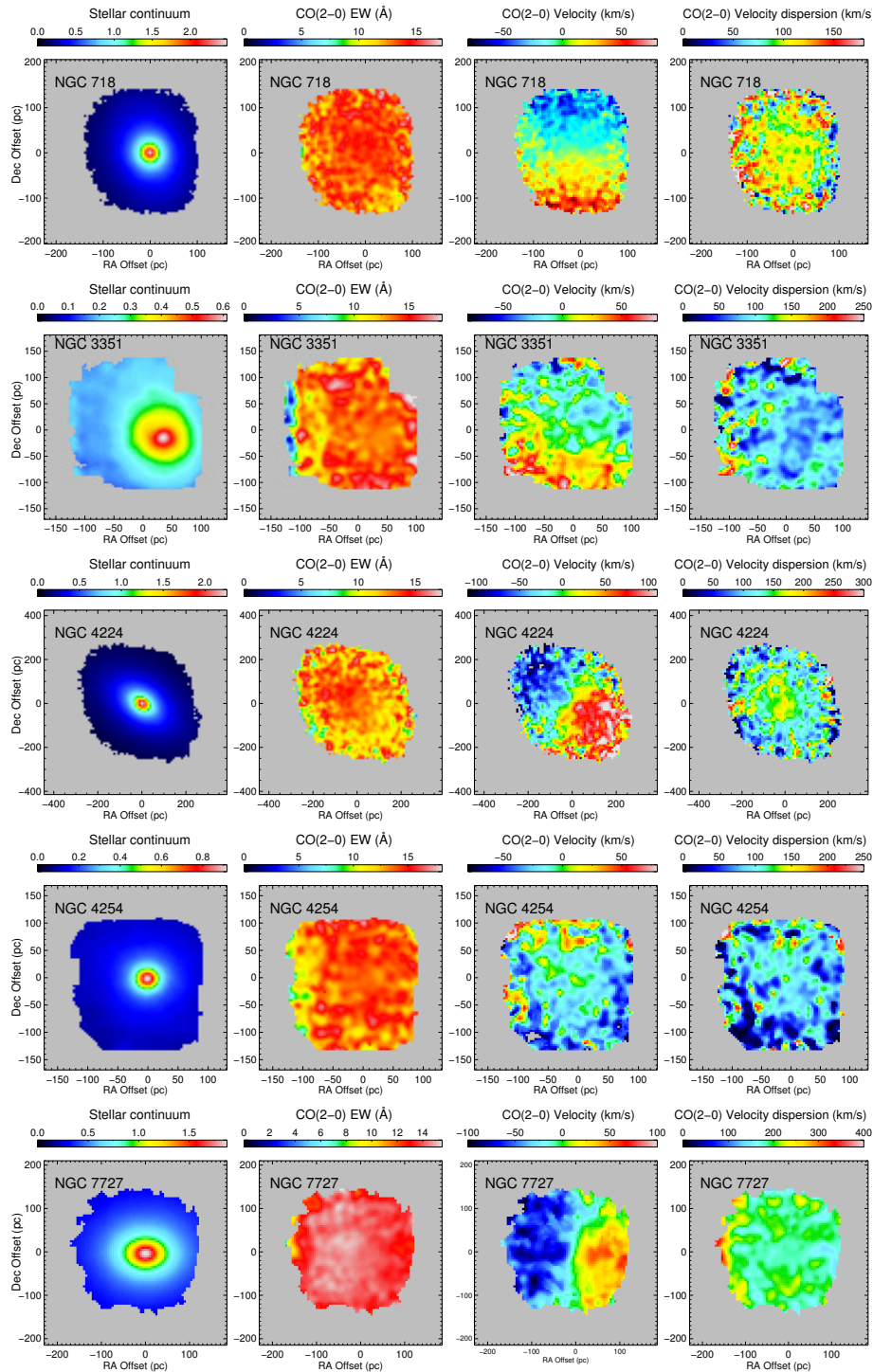


Figure 3.4: Matched inactive galaxy sample. Maps are labeled from left to right: stellar continuum flux, CO(2-0) equivalent width (EW), stellar velocity, and stellar velocity dispersion. There is no non-stellar continuum to dilute stellar absorption features, thus the kinematics can be simply extracted. NGC 4254 has no clear velocity gradient because the system is very close to face-on. In all maps, north is up and east is to the left, the coordinate offset has been converted into the physical scale in parsec.

### 3.3.2 Continuum luminosity profile

The goal of this study is searching for any nuclear excess stellar flux, which could indicate a young stellar population, and may be associated with a stellar velocity dispersion drop. Our FOV is only  $3''$  which, for the nearby galaxies in our sample, is well within the galactic bulge. Thus an important step is to understand the larger scale bulge contribution in which these data reside. Once the bulge Sérsic profile has been derived, then we can check whether all the nuclear stellar flux follows the larger-scale bulge light profile.

To constrain the bulge Sérsic profile properly and systematically, we use the two-dimensional profile fitting algorithm GALFIT to decompose bulge and disk on scales of  $2''$ - $100''$  with 2MASS Ks-band data, which trace the stellar light with less bias to extinction or stellar age than optical data. GALFIT requires the sky background and a PSF image. The sky background is set as a fixed parameter and obtained by measuring the mean value in the blank field of the same image. The PSF, which allows us to correct the seeing, is generated as a Gaussian with FWHM of  $2.5''$ . This provided a better residual map than when we used a bright star obtained from the 2MASS image. Since 2MASS does not provide a pixel noise map, we do not include it in the calculation. Ordered lists of pixel coordinates have been used as a bad pixel mask, if needed to block bright stars close to the galaxy. For each galaxy, we iteratively fit two Sérsic profiles: one with a variable index, and one with the index fixed to an exponential profile. These components aim to model the large scale bulge and the disk respectively. Initial parameters are estimated by visual inspection, e.g. position angle (PA), ellipticity, and effective radius, etc. However, we note that the best fit value derived in the literatures also can be regarded as an initial guess for each parameter. By slightly changing the initial guess of each model component, we find that the choice of initial guesses do not influence the final result significantly. We also note that while the GALFIT output provides a formal  $\chi^2$  showing the difference between model and data, this is a purely quantitative assessment, and does not fully reflect whether a fit is good. It is more important to judge the quality of the fit from the residual maps. There are two steps in our fitting procedure:

(1) Fitting large scale disk and bar: We keep the number of free parameters to a minimum by fixing the Sérsic index  $n_{disk} = 1$  and leaving the effective radius  $r_{e,disk}$  as a free parameter. In addition, if a large scale bar has been identified in the host galaxy, we fit it using an additional Sérsic profile. Initially, we allow  $n_{bar}$  and  $r_{e,bar}$  to be varied; however, if the GALFIT output value for  $n_{bar}$  is too small (i.e.  $n_{bar} \leq 0.1$ ) or is too similar to the disk (i.e.  $n_{bar} \sim 1$ ), we then fix  $n_{bar} = 0.5$ , which remains a fairly constant value across different Hubble type within a limited range of  $M_*$  around  $\sim 10^{10} M_\odot$  (Weinzirl et al., 2009).

(2) Fitting large scale bulge: There is no constraint on  $n_{bulge}$  and  $r_{e,bulge}$  when we fit the bulge component. The PA and ellipticity are set to be in reasonable range of quantitative agreement with the observed image. For the active sample, we also include a central point source to account for the AGN and avoid  $n_{bulge}$  growing unrealistically large. Note that any structures inside the bulge – for example a nuclear disk, circumnuclear ring, or nuclear bar – are not considered during the fitting, since they could be a part of the young stellar

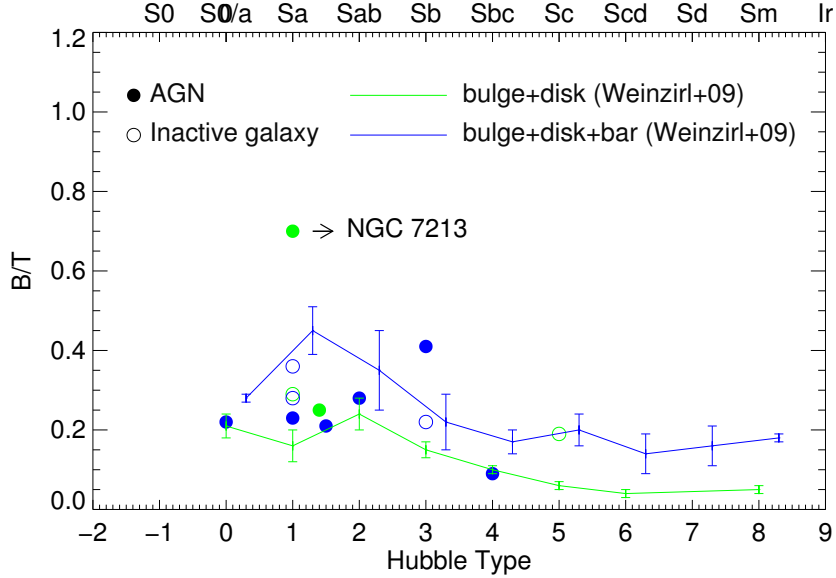


Figure 3.5: Individual bulge to total luminosity ratio ( $B/T$ ) as a function of Hubble type. With and without bar component in the two-dimensional decomposition fitting is shown in blue and green colour labelled both in lines and symbols. The filled circles represent Seyfert galaxies, while the open circles are inactive galaxies. The lines are the mean and standard deviation of  $B/T$  as a function of Hubble type from Weinzirl et al. (2009).

population which we expect to find.

Studies with large samples of galaxies show that the bulge-to-total luminosity ratio ( $B/T$ ) increases from late-type galaxies to early-type galaxies, i.e. as a function of Hubble type (Weinzirl et al., 2009). The results of our fitting show a similar trend in our small sample as presented in Figure 3.5, confirming that the fits are reasonable. We also note that there is no difference in  $B/T$  between AGN and inactive galaxies, consistent with our selection strategy of matching the active galaxies to the AGN based on host galaxy morphology and stellar mass. We find NGC 7213 deviates from the relation between the  $B/T$  and Hubble type. Its bulge parameter coupling problem has been discussed and tested in Section 4.4 of Weinzirl et al. (2009). Given the Sa morphology, a  $B/T$  of  $\sim 0.3$  only occurs when we fix  $n_{bulge} = 1$ , which cannot be distinguish from outer disk, thus we decide to adopt the solution of  $n_{bulge} = 2.57$  with  $r_{e,bulge} = 13.7''$ . The details of the Sérsic parameters for the bulge, bar, and disk are listed in Appendix A. Most galaxies in our sample tend to have small  $n_{bulge} \sim 1-2.5$ , which is likely to be diskly bulge (pseudobulge) instead of classical bulge with  $n = 4$ .

The next step is to match the flux scaling between the 2MASS profile fit and the SINFONI data. In order to compare the radial gradient between the observation scales, we extract the 1-D flux profile along the major-axis direction both from the 2MASS Ks-band image and the SINFONI stellar continuum image. The stellar continuum is measured from the CO(2-0) absorption bandhead after correcting the non-stellar AGN contribution

<sup>2</sup> (Davies et al., 2007; Burtscher et al., 2015). The major-axis PA is the mean value measured from Spitzer near-infrared photometry (Sheth et al., 2010) and SINFONI stellar kinematics. Once the bulge Sérsic index and effective radius have been obtained from the GALFIT decomposition, and assuming the SINFONI outer region  $\sim 1.0''$ - $2.0''$  is bulge dominated, we extrapolate the bulge 1-D flux profile to a radius  $< 1.5''$  and look directly at the residual, to check whether the central few parsecs follow the outer bulge Sérsic profile. If there is an HST F160W archive image on scales of  $0.2''$ - $15''$ , we use it to reinforce the connection between SINFONI and 2MASS. However, the HST data have smaller pixel scales ( $0.075''$  for NICMOS and  $0.038''$  for WFC3) and higher spatial resolution that better resolves the circumnuclear structures, and these can induce a slight inconsistency in the radial gradient between HST and 2MASS. We carefully minimize this effect due to fine structures when matching the profiles by extending the normalised region to include the large scale disk. Near-infrared wavelengths are less sensitive to extinction than the optical (the V-band to Ks-band extinction ratio is 1:0.062, Nishiyama et al. 2008), thus we did not correct for any near-infrared extinction in this study. The results are presented in Section 3.4.

## 3.4 Nuclear Stellar Continuum Excess

In these sections, we present the one-dimensional radial stellar continuum profile for our objects, in order to assess whether there is any photometric difference between the AGN and the matched inactive galaxy sample. We address this issue from two perspectives: the stellar surface luminosity distribution and the central excess light.

### 3.4.1 Radial distribution of stellar luminosity

Figure 3.6 shows the stellar surface brightness of AGNs and inactive galaxies, drawn as red and blue lines respectively. The top left panel of Figure 3.6 is the directly observed stellar surface brightness from VLT-SINFONI. An observational caveat is that there are three AGNs (NGC 3783, NGC 4593 and NGC 7172) with strong non-stellar continuum contribution in the centre; therefore it is difficult to extract the stellar surface brightness towards the radius below 50 pc. Obviously, there are two inactive galaxies, which have lower stellar surface brightness: NGC 3351 and NGC 4254. The reason is that they have about 10 times lower K-band luminosity within our SINFONI field and 2 times closer distance, resulting in  $\sim 1.5$  dex lower surface brightness than other galaxies. Except for these two outliers, the surface brightness for other galaxies which obtained with SINFONI H+K grating are about  $10^{3-4} L_{\odot} \text{pc}^{-2}$  and the radial surface brightness distributions are

---

<sup>2</sup>The non-stellar AGN light is estimated from the equivalent width (EW) of dilution CO(2-0) bandhead with a given intrinsic EW, which is expected to be a constant value over a wide range of star formation histories and ages (i.e.  $L_{AGN} = L_{obs} \times f_{agn}$  where  $f_{agn} = 1 - (EW_{obs,diluted}/EW_{intrinsic})$ ). Note that  $f_{agn}$  close to 1 corresponds to  $\sim 100\%$  AGN contribution.

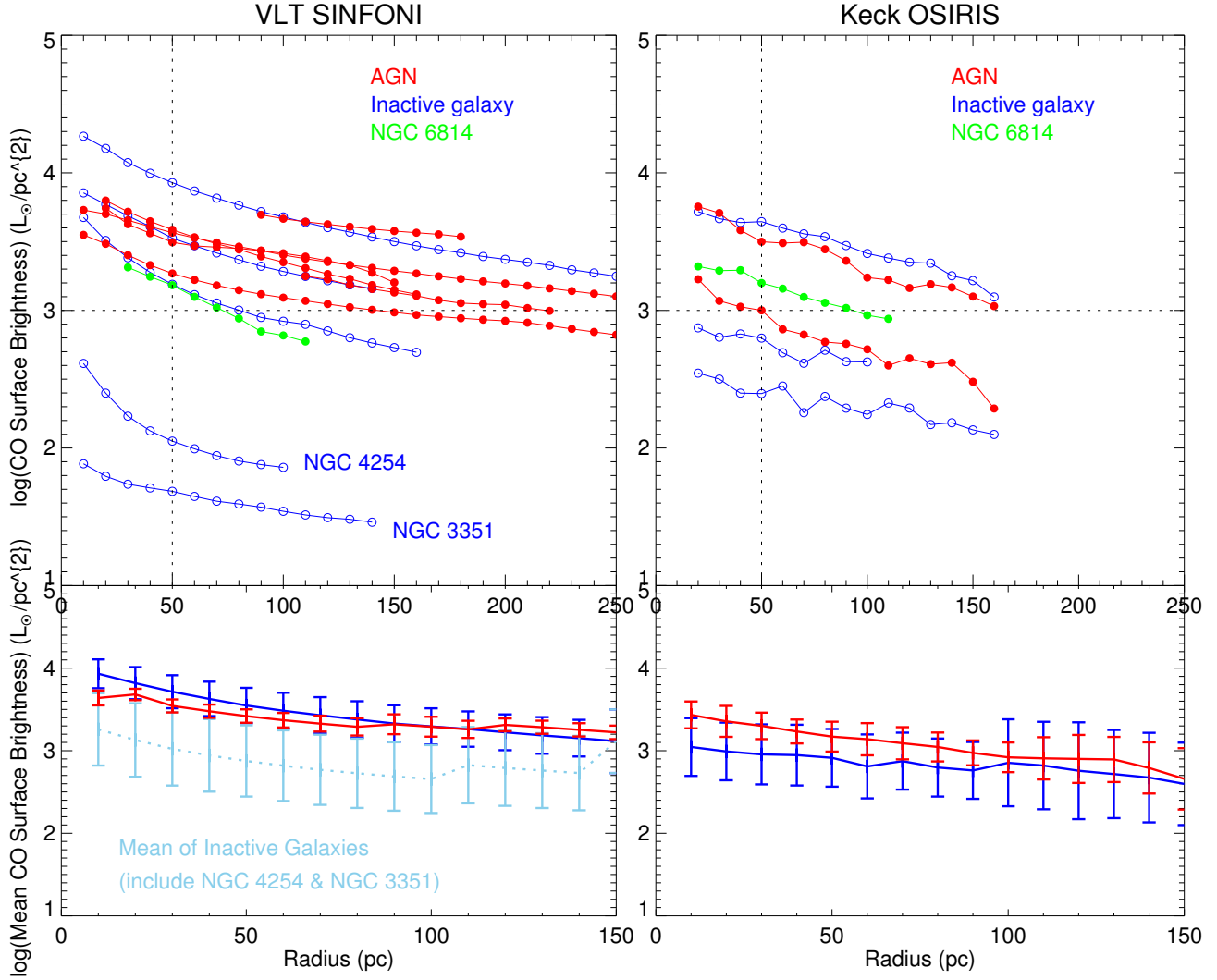


Figure 3.6: The radial stellar light distribution. Top left panel: the stellar surface brightness as a function of radius for LLAMA sample. All of them were observed with VLT-SINFONI. Top Right panel: the stellar surface brightness as a function of radius for three AGNs and three inactive galaxies, where were observed with Keck-OSIRIS. AGNs and inactive galaxies are labelled as red and blue lines respectively. Both observations have covered NGC 6814 (AGN), which we highlight it as green colour. Bottom panels: the mean value at that radius and the radial bin size, the error bars are the standard deviation of measurements within each radial bin. The mean value of AGN and inactive galaxy sample are illustrated as bold red and blue lines. The light blue colour is the mean of all inactive galaxies, while the dark blue colour is the mean of inactive galaxies except for these two outliers (NGC 3351 and NGC 4254).

generally similar for both active and inactive samples (refer to the bottom left panel of Figure 3.6).

A comparison of the stellar surface brightness between AGNs and matched inactive galaxies has been presented in Figure 15 in Hicks et al. (2013). They showed that at radii greater than 150 pc, the Seyferts in their sample had a lower surface brightness than the inactive galaxies. However, the luminosity profile was steeper for the AGN, which led to similar, or in some cases higher, surface brightnesses at small radii. The reason leading to the differing results of our LLAMA sample and Hicks et al. (2013) will be discussed together with kinematic comparison in Section 3.5.3.

In addition, we are well aware that it is difficult to compare our work directly to previous Hicks et al. (2013) study because the spatial pixel scales are different. Unlike Hicks et al. (2013) where observations cover a radial range of 50–250 pc, most of our observations cover a smaller range of 10–150 pc. Thus we compare our work to recent Keck OSIRIS data (Hicks et al. in prep) of a similarly matched sample at spatial scale comparable to VLT SINFONI. The preliminary results have been presented in the right panels of Figure 3.6, where AGN sample is labelled as red colour while a matched inactive sample is plotted in blue colour. NGC 6814 (AGN) has similar surface brightness in both observations, which is highlighted as appearing in green colour. Based on current available data, we find that inactive galaxies cover a wider range of surface brightness in radial range of 10–150 pc. We note that there are some inactive galaxies have stellar surface brightness comparable to that of AGNs, it may suggest that the timescale of AGN switching on and off is shorter than the timescale to form nuclear stars, and the nucleus of those inactive galaxies may be just in quiescent phase. Neither observation shows that any AGN with stellar surface brightness below  $10^3 L_{\odot} \text{pc}^{-2}$  within the central 50 pc, implying the mechanism to trigger AGN only happens more effectively in the galaxy which has higher stellar surface brightness. These conclusions will be revisited once the full sample is available.

### 3.4.2 Central excess of stellar light

In this section we look at whether there is an excess or deficit in the stellar continuum compared to the bulge contribution that was extrapolated from the fit at larger scales. In Section 3.3.2, we described the method we used to measure the Sérsic index and effective radius of the bulge component from large scale 2MASS Ks band data. By inward extrapolation of the fitted bulge Sérsic profile to the SINFONI FOV, we find that the stellar light at  $< 1''$  does not always follow the bulge profile. We classify the central stellar light profile as an excess (i.e. cusp) or deficit (see middle left panel in Appendix B). A similar dichotomy has been found in early-type galaxies in Virgo and Fornax clusters (Côté et al., 2007). Although our study focuses on Seyferts and inactive galaxies, many of which are late-type, we adopt a similar concept to parameterize the inner stellar profile. We introduce a parameter,  $\Delta_L$ , as a ratio of the observed discrepancy in the SINFONI K-band luminosity (i.e. the difference between the stellar luminosity and the extrapolated bulge contribution) to the total SINFONI K-band luminosity. This is estimated from the 1-D flux profile extracted along the major axis PA and then, assuming their radial distribution

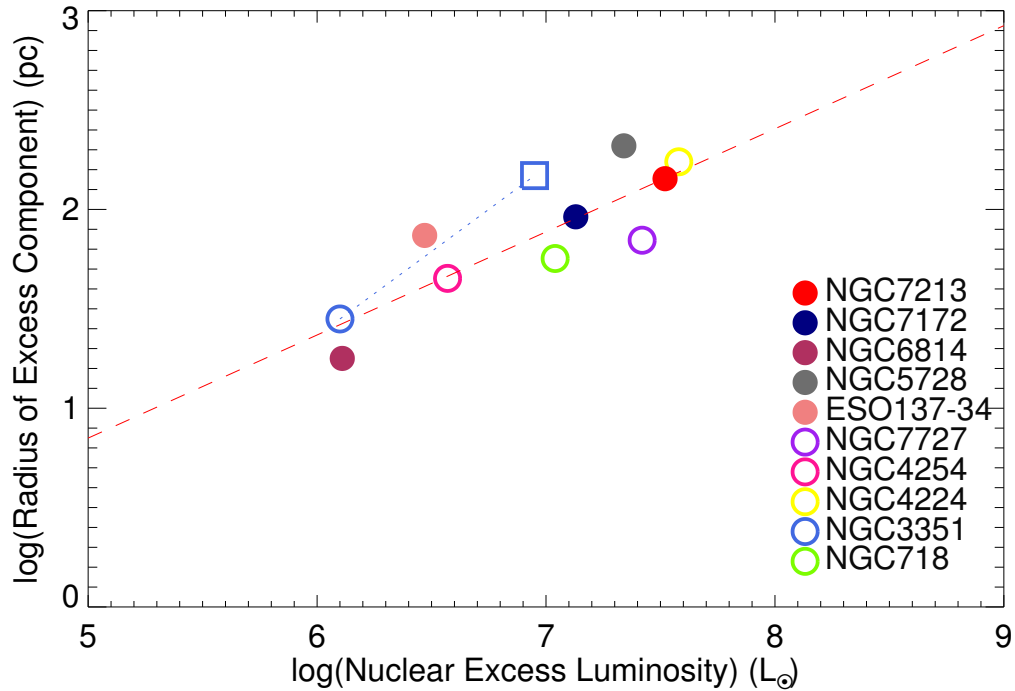


Figure 3.7: The size-luminosity relation of excess nuclear star light (i.e. excluding the objects with central deficit star light). The excess star light is defined as a region, where the radial stellar light distribution does not follow the prediction of outer fitted bulge Sérsic profile. The filled circles represent Seyfert galaxies, while the open circles are inactive galaxies. Circle with different colour is given for each object. NGC 3351 has two measurements, the open square is the entire excess star light within the entire SINFONI FOV, while the open circle is an excess cusp appearing in the innermost region. Since the strong non-stellar dilution surrounds entire SINFONI FOV in NGC 3783, it has been excluded in this plot.

is symmetric,  $\Delta_L$  is a radial integration until the radius where there is no significant excess lights (i.e.  $R_{excess}$  in Table 3.2). Note that this 1-D flux extraction method of the central profile has the advantage that it is less susceptible to the stellar light asymmetry induced by foreground dust lane extinction, which can often create a large discrepancy along the minor axis. Galaxies with a central stellar light deficit then have  $\Delta_L < 0$ , while those with excess have  $\Delta_L > 0$ .

Most galaxies have a central stellar light excess, ranging from 1-12%. Despite the central excess for NGC 6814 is small (1%), we still consider it as a real detection in the following study because its radial slope of the innermost excess component slightly differs from the slope of the 0.4-2'' outermost region. But notably there are two AGNs which have a central stellar light deficit: NGC 4593 and NGC 7582. In order to confirm these light deficit features, we plot the HST/NICMOS/F160W radial flux along the major axis and find that it matches well with our SINFONI radial flux profile. The deficit could be due to either the intrinsic central behaviour or to foreground dust extinction. NGC 7582 is an example of the latter case, where the foreground dust lane across the circumnuclear region causes the stellar light asymmetry. However we cannot rule out that its stellar light deficit is intrinsic. The central stellar light deficit in NGC 4593 is likely to be intrinsic, and is unambiguously observed in both SINFONI and NICMOS radial flux profiles. Furthermore, we try to measure the bulge Sérsic profile solely based on HST/NICMOS/F160W image for these two galaxies by using GALFIT algorithm. NGC 7582 has strong asymmetric photometry that we cannot constrain the bulge Sérsic profile properly. On the other hand, for NGC 4593, although the radial Sérsic profile of bulge component is shallower (i.e. the amount of deficit light decreases), we still do not find any significant stellar excess toward the centre; the detail results are presented in the top right panel of Figure B.7.

For those galaxies with central stellar light excess, we fit a Gaussian function to characterize the size of the excess component (a similar method has been used in dwarf elliptical galaxies by Graham & Guzmán 2003). The radius encloses 99% of Gaussian profile (i.e.  $3\text{-}\sigma$  away from the centre). NGC 3351 is a special case. Within the SINFONI FOV, the nuclear stellar light is entirely above the extrapolated bulge profile, and the integrated luminosity is 32% higher than expected. In addition, to match the radial profile of the excess, we included a second Gaussian to fit the central cusp at a radius  $< 0.5''$ , the slope of which is distinct from that of the 0.5-2'' outermost regions. Interestingly, a similar situation in which there appear to be two components to the nuclear stellar excess was reported for another nearby Seyfert 1 galaxy NGC 3227 by Davies et al. (2006) (their Figure 6 and 7). That work shows there is a clear excess starting at a radius of  $0.5''$ , and the central cusp appears within a radius of  $0.1''$ . In our sample, NGC 3783 is a difficult case because the non-stellar contribution is strong across the whole SINFONI FOV. Thus, while we do measure an excess in the nuclear stellar luminosity, the scale is very uncertain and so we exclude it from our comparison of size versus luminosity. Making use of the 10 objects with central excess stellar light (see Table 3.2), we find the nuclear excess luminosity is proportional to the size of the excess component as shown in Figure 3.7. There is no significant difference in light excess between AGNs and inactive galaxies. This size-luminosity

relation can be written as:

$$\log(R_{excess}) = (0.52 \pm 0.10) \times \log(L_{excess}) - (1.74 \pm 0.73) \quad (3.6)$$

We find that Spearman's rank correlation coefficient is  $\rho \sim 0.80$  indicating a 98% significance for the correlation (noting that  $\rho = 1$  corresponds to two variables being monotonically related).

A central stellar light excess has been found in different types of galaxies, and is usually considered to be a nuclear star cluster (NSC). Böker et al. (2004) investigated the nearby late-type face-on spiral galaxies and found the optical *i*-band luminosity of NSCs (mean  $\sim 10^{6.4} L_{\odot}$ ) strongly correlates to its host galaxy luminosity, but the size-luminosity correlation of NSCs is weak. On the other hand, Côté et al. (2006) studied the compact central nuclei of early-type galaxies in the Virgo cluster in both g-band and z-band images and found that the size-luminosity relation of NSCs is  $r \propto L^{0.5}$ , where the mean luminosity of an NSC is  $\sim 10^{7.7} L_{\odot}$ . Such a relation can be understood in terms of a merger model: the radius of the nucleus increases with increasing total luminosity as globular clusters merge (Antonini, 2013). In our sample, the mean K-band luminosity for nuclear excess stellar light is  $\sim 10^7 L_{\odot}$ , which is comparable to those NSCs found in the nuclei of early-type or late-type galaxies, if we assume NSCs mass of  $\sim 10^7 L_{\odot}$  with  $M/L_H$  of 0.6 (Seth et al., 2010; Antonini, 2013). However the size of the excess nuclear stellar light in our study is not matched to those of NSCs. The typical size of NSCs is 5 pc, although a few of them can extend to 20-30 pc. In contrast, for our sample, we find a mean size of  $\sim 80$  pc, and the size of individual nuclei ranges from 200 pc down to 10 pc. These are more likely to be an extended nuclear stellar disk rather than NSCs (Balcells et al., 2007). The reason that we cannot observe NSCs is due to the distance of our sample and the corresponding physical pixel scale is at least 10 pc, thus the NSCs cannot be spatially resolved. The extended size of the nuclear disks give clues, that such objects might have a different nature and structure than either compact NSCs or the bulge. The size-luminosity relation of the nuclear disks suggests their formation may nevertheless have some similarities to that of NSCs.

Table 3.2: Nuclear properties of each galaxy: (1) Galaxy name, upper rows are AGNs and lower rows are inactive galaxies; (2) Systematic velocity derived from stellar kinematics; (3) Kinematic position angle from stellar velocity field; (4) Mean velocity dispersion of bulge ( $\sigma$  at a radius  $> R_{excess}$ ); (5) The trend of velocity dispersion at a radius  $< R_{excess}$ ; (6) Stellar luminosity from SINFONI data cube within approximately  $3''$  aperture size (depend on how far of good pixels we can achieve); (7) Stellar luminosity of nuclear excess light; (8)  $\Delta_L$ ; (9) Size of the nuclear excess light (without taking into account the PSF of  $0.1''$  radius) <sup>†</sup>.

(1) Galaxy name	(2) $v_{sys}$ ( $\text{km s}^{-1}$ )	(3) $PA_{kin}$ ( $^{\circ}$ )	(4) $\sigma$ ( $\text{km s}^{-1}$ )	(5) $\sigma$ trend	(6) $\log(L_K)$ ( $L_{\odot}$ )	(7) $\log(L_{excess})$ ( $L_{\odot}$ )	(8) $\Delta_L$ (%)	(9) $R_{excess}$ ( $''$ )
ESO 137-34	2791.11	37	$105 \pm 5$	flat	8.19	6.47	1.94	0.40
NGC 3783 <sup>a</sup>	3044.28	137	$154 \pm 4$	drop	8.73	7.82	14.35	0.55
NGC 4593	2553.97	106	$149 \pm 3$	increase	8.15	–	–	–
NGC 5728	2834.28	12	$164 \pm 4$	flat	8.29	7.34	12.15	1.05
NGC 6814	1612.63	37	$115 \pm 2$	flat	8.10	6.11	1.00	0.20
NGC 7172	2591.40	93	$103 \pm 4$	drop	8.52	7.13	4.32	0.60
NGC 7213	1876.60	31	$201 \pm 3$	flat	8.52	7.52	11.00	1.40
NGC 7582	1651.05	155	$68 \pm 4$	flat	8.79	–	–	–
NGC 718	1775.06	13	$100 \pm 2$	flat	8.3	7.04	6.03	0.59
NGC 3351	867.93	174	$84 \pm 2$	drop	7.57	6.95 [6.10] <sup>b</sup>	32.11[4.52]	2 [0.38] <sup>b</sup>
NGC 4224	2651.79	56	$153 \pm 2$	increase	8.76	7.58	6.95	0.91
NGC 4254	2514.77	87	$92 \pm 2$	increase	7.53	6.57	11.55	0.60
NGC 7727	1885.17	50	$187 \pm 3$	flat	8.53	7.42	8.40	0.7

<sup>†</sup>: We assume the nuclear excess light followed the Gaussian profile, the radius encloses 99% of Gaussian profile.

<sup>a</sup>: Strong non-stellar continuum do exist across whole SINFONI FOV that nuclear stellar excess does not take into account in our analysis.

<sup>b</sup>: The luminosity and radius of excess component in the central cusp.

## 3.5 Nuclear stellar kinematics

In terms of stellar kinematics, the inactive galaxy sample is relatively simple to analyze, while the situation for the AGN sample is more complicated. This is because there is non-stellar hot dust contamination in the near-infrared which causes dilution of the stellar features, making it challenging to extract the kinematics. This issue will be discussed in Section 3.5.1. Looking at the stellar continuum maps, there are relatively noisy structures around the nuclear region in the AGN sample. This is because they are not direct measurements, but their K-band continuum includes the non-stellar continuum from AGN and stellar continuum, the latter of which can be extracted via CO EW (note that ESO 137-34 and NGC 5728 do not show any CO dilution and hence have no AGN hot dust). Overall, most galaxies (11/13) in our sample show nearly symmetric stellar continuum maps with regular elliptical isophotes. The two exceptions are NGC 7172 and NGC 7582, for both of which the maps exhibit extreme irregularities coinciding with known dust lanes (Bianchi et al., 2007; Smajić et al., 2012). These pass across their nuclei and are clearly visible in optical HST F606W images (Malkan et al., 1998). It is difficult to quantify the Ks-band extinction and correct it with present data. Fortunately, such extinction does not have a major influence on the extraction of stellar kinematics. Although the stellar continuum asymmetry runs along the minor axis, there is no significant feature in the kinematics along the same direction. NGC 3783 suffers strong dilution from non-stellar light, making it difficult to extract the kinematics and measure the PA. As a result the kinematics maps for this AGN are very noisy. For the galaxies NGC 6814 and NGC 4254 (Pair 8), the observed rotating velocity pattern is weak because they are both nearly face-on. This leads also to larger uncertainties in estimating the kinematic PA on small scales. In the following sections, we discuss CO dilution and present the analysis of the two-dimensional stellar kinematic maps.

### 3.5.1 Nuclear dilution by non-stellar light

For all the inactive galaxies, the stellar CO(2-0) EW has a relatively uniform distribution. In contrast, most AGNs (6/8), with the exception of ESO137-34 and NGC 5728, have a decreasing CO EW toward the centre. The reason for this is that the stellar absorption features are diluted by the strong non-stellar continuum which is linked to hot dust associated with the AGN. Figure 3.8 shows the radial CO EW gradient. The average intrinsic CO EW is 10-15Å, and for the inactive galaxies is slightly higher than typical value of 11Å reported by Burtscher et al. (2015) but within the range expected. We find there are four AGNs, their CO EW at 1.5'' outermost regions are lower than the CO EW of inactive galaxies and other AGNs at same radii. Their name are labeled in Figure 3.8. For NGC 3783, NGC 4593, and NGC 7172, they have higher  $L_{14-195}$  and less obscuration with respect to other AGNs, suggesting, even at 1.5'' outer regions, the strong non-stellar continuum may marginally dilute the stellar absorption features. We note here, in the case of NGC 3783 (the bright Seyfert nucleus in our sample), the CO bandhead appears to be very diluted everywhere within the 3'' field of view. We therefore analyse also a SINFONI

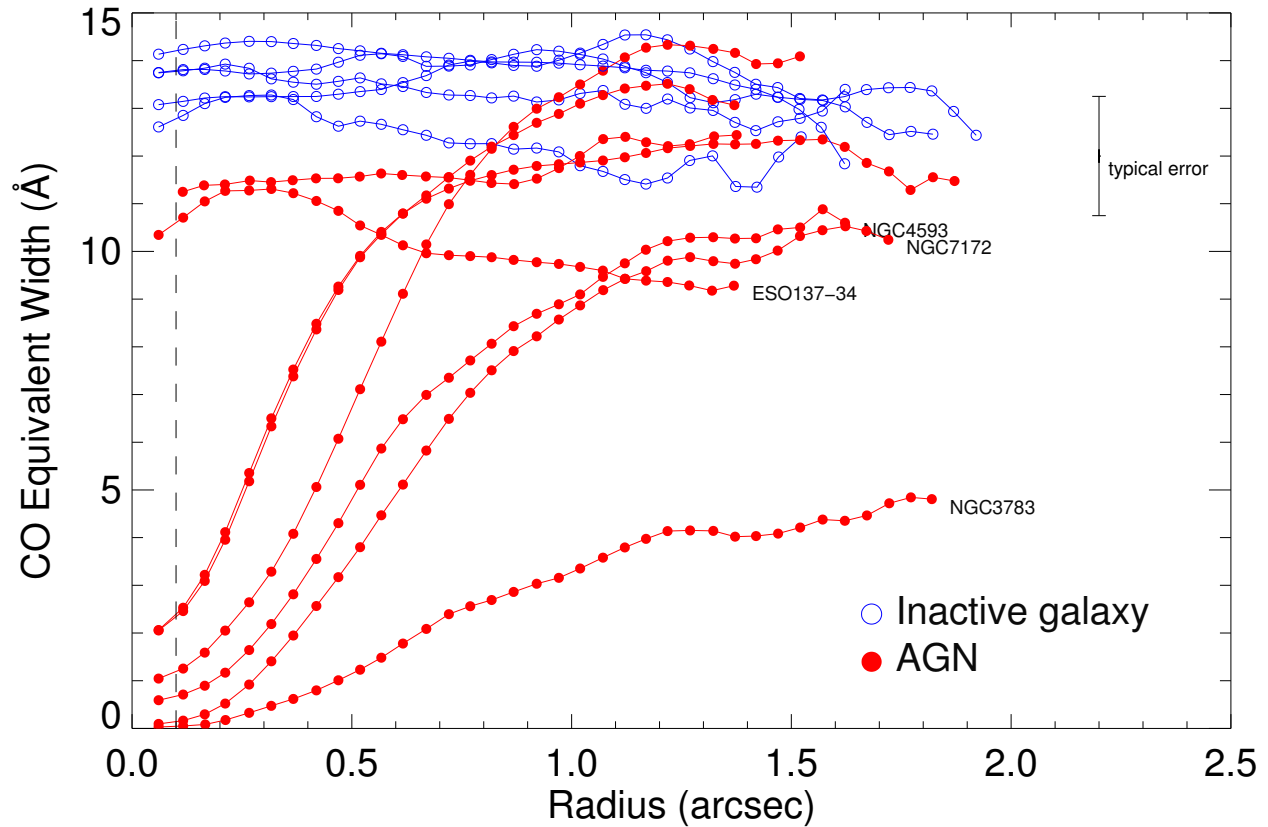


Figure 3.8: Radial averaged CO EW. Red filled circles and blue open circles represent the AGN sample and the matched inactive galaxy sample. The decreased CO EW trends toward the centre in AGNs suggest the increasing contribution of non-stellar continuum. The FWHM radius of AO-corrected PSF is  $0.1''$ , presented in black dashed line.

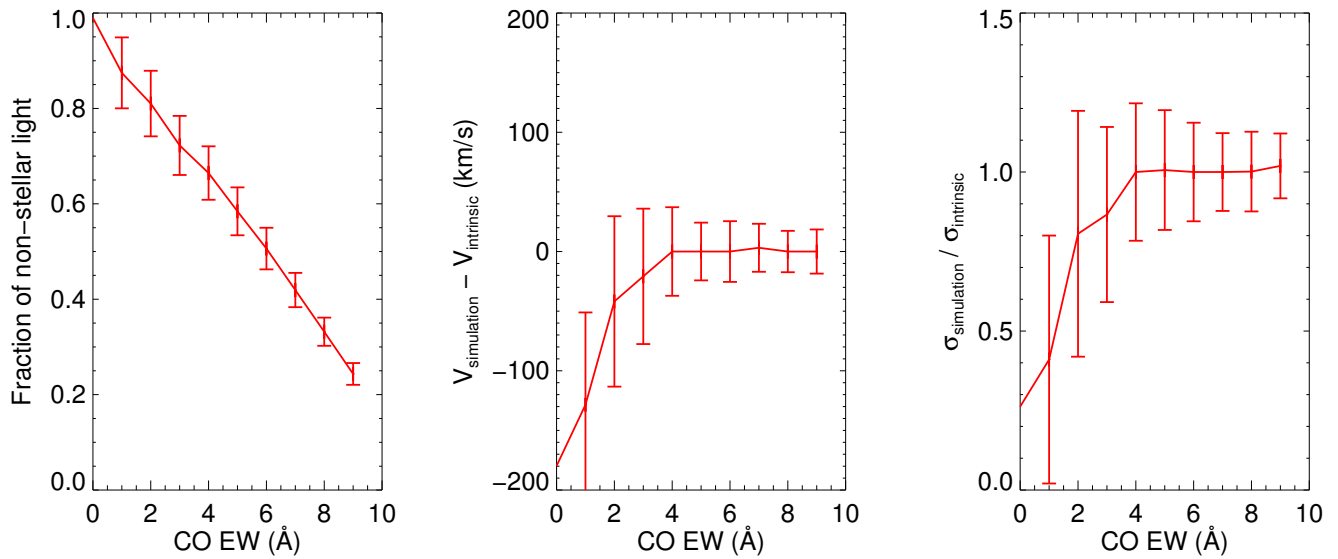


Figure 3.9: Simulation of the impact of non-stellar continuum contribution on CO EW and stellar kinematics from 100 synthetic spectra. Red lines are the median value at each CO EW bin, the red error bars represent the  $1\sigma$  uncertainties. Left panel: The fraction of non-stellar continuum as a function of CO EW. Middle panel: The velocity offset from the intrinsic stellar velocity measurement. Right panel: The velocity dispersion ratio of the simulation to the intrinsic measurement. Stellar velocity and velocity dispersion start to deviate from the intrinsic measurements at CO EW  $\leq 3\text{-}4\text{\AA}$ , suggesting any kinematic measurement below this CO EW range is uncertain.

datacube with a FOV of  $8''$  and find that the CO EW in outer regions is  $\sim 8\text{\AA}$ . We adopt this value as the intrinsic CO EW for this galaxy, despite it being lower than the mean value we found in other galaxies. In contrast, there is no CO dilution in ESO 137-34, the CO EW of  $\sim 10\text{\AA}$  across the whole FOV is likely to be intrinsic, implying the age of stars could be different from those galaxies with CO EW of  $12\text{-}15\text{\AA}$  (Davies et al., 2007). For the purpose of assessing the impact of the non-stellar continuum on the kinematics extraction, we produce a simple test to simulate the observed CO EW dilution. We start with the best-fit template spectrum of NGC 7727 (an inactive galaxy without any non-stellar contamination) and add a pure blackbody emitter with temperature of  $1000\text{K}$ , representing the non-stellar continuum (Riffel et al., 2009; Burtscher et al., 2015):

$$F_{\text{synthetic}} = (F_{\text{template}} \times (1 - c)) + (F_{\text{blackbody}} \times c) \quad (3.7)$$

where  $c$  is the fraction of blackbody emitter, increasing from 0% to 100%, in the steps of 10%: Noise has been included in the synthetic spectrum to ensure that the S/N reaches  $\sim 10$  as the real data. The synthetic spectrum is then treated with the same analysis procedure as for the real data, measuring the kinematics and the CO EW. We repeat this process 100 times in order to make the experiment statistically robust. The results are illustrated in Figure 3.9. The left panel shows how much the non-stellar continuum dilutes the CO EW. Once the CO EW becomes small, it is difficult to extract kinematics reliably because noise overwhelms the stellar absorption features. The middle and right panel of Figure 3.9 show the velocity offsets and the velocity dispersion ratios to the intrinsic stellar kinematic measurement. The velocity offsets and the velocity dispersion ratios deviate significant when  $\text{CO EW} \leq 3\text{-}4\text{\AA}$ . Below this CO EW threshold, the velocity offsets and the velocity dispersion ratios are dominated by the randomly generated noise, indicating that the CO EW threshold is relatively sensitive to the data quality rather than just to the non-stellar continuum contribution fraction. In particular, NGC 7582 has a small CO EW in the centre but the velocity and velocity dispersion can still be measured reliably even close to the AGN. The reason is that it is the brightest galaxy in our sample in the K-band, and the noise in the data is small enough that we can extend the CO EW dilution limit to  $2\text{\AA}$ . For other active galaxies, we are limited to a radius corresponding to a CO EW threshold of  $3\text{-}4\text{\AA}$ , and exclude any kinematic measurement within this radius. We have therefore truncated this region in Figures 3.2-3.3.

### 3.5.2 Kinematic PA versus photometric PA

In this section we compare the PA from the fits to the small scale kinematics ( $\text{PA}_{\text{kin}}$ ) with the large scale photometric data ( $\text{PA}_{\text{photo}}$ ). The kinematic PA is derived from the SINFONI stellar velocity map using the software developed by the SAURON team (Cappellari et al., 2007; Krajnović et al., 2011) <sup>3</sup>. The kinematic PA is listed in Table 3.2. We obtain the photometric PA from the catalog for the Spitzer Survey of Stellar Structure in Galaxies (S4G), which observed numerous nearby galaxies at  $3.6$  and  $4.5 \mu\text{m}$  with the Infrared Array Camera (IRAC). This catalog has the advantages that the seeing has been excluded when

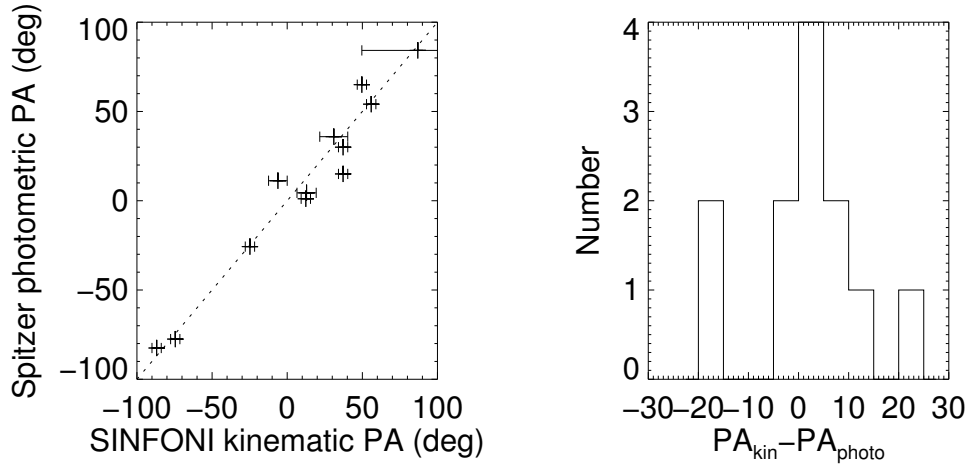


Figure 3.10: Left panel: The Spitzer photometric PA plotted against the SINFONI kinematic PA. The photometric PA is redrawn from S4G catalog. The kinematic PA is measured by SINFONI stellar velocity field (see the third rows in Figure 3.2-3.4). The black dotted line is the 1:1 relation. Right panel: Histogram showing the distribution of PA difference measured with two independent methods.

fitting the photometric ellipses and the observations cover the extension of the large scale disk. NGC 3783 has been excluded in our comparison because there is no  $PA_{photo}$  measurement from the catalog, which may be due to its bright Seyfert 1.5 nucleus preventing a measurement. Figure 3.10 shows that the  $PA_{kin}$  is in good agreement with  $PA_{photo}$ , the differences between two measurements being in the range  $8 \pm 6^\circ$ . In the following study, we simply adopt the mean of these two PAs and set  $\pm 5^\circ$  as the uncertainty. For comparison, the difference between our  $PA_{kin}$  and  $PA_{photo}$  is a factor two larger than Barnes & Sellwood (2003) found, but it is robust enough for our analysis presented below. A similar result has been found in 16 nearby Seyferts with using Gemini NIFS data, both the large-scale photometric and small-scale kinematic axis are well aligned (Riffel et al. 2017 submitted). We note that NGC 4254 has the largest uncertainty when calculating the kinematic PA, and NGC 6814 has the largest inconsistency in the measurements. It is because they are both face-on galaxies.

### 3.5.3 Radial average kinematics

We use the IDL routine *kinometry* to extract radial distributions for the velocity and velocity dispersion from the 2D kinematic maps. The details of the method are described by Krajnović et al. (2006). Here we briefly summarise the key equations, which provide an important insight to quantify the physical meaning. By using Fourier analysis to characterize the periodicity, the observed kinematic moments can be divided into a series of

<sup>3</sup><http://www-astro.physics.ox.ac.uk/~mxc/software/>

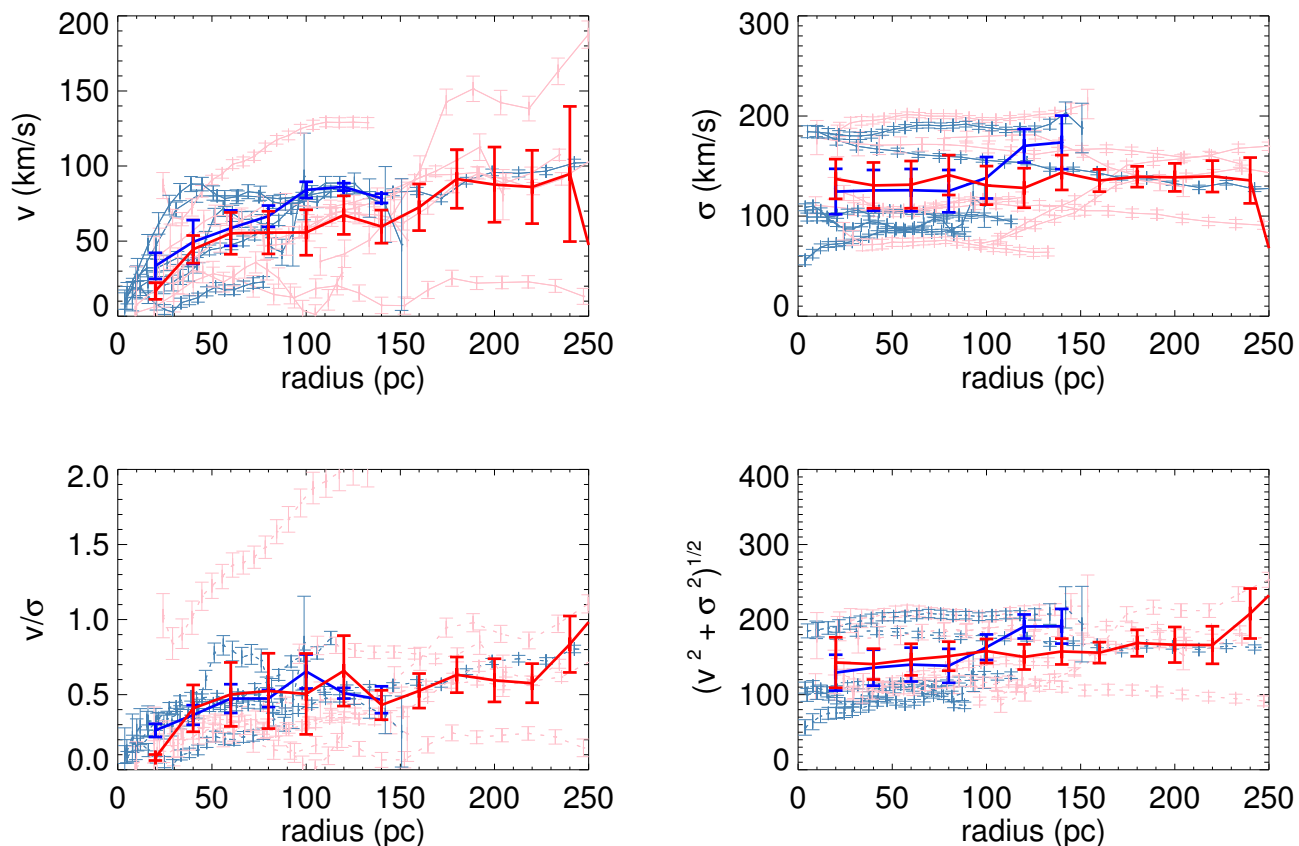


Figure 3.11: Radial average kinematic properties of the CO(2-0) stellar absorption: AGNs and inactive galaxies are represented in pink and navy blue points. The mean value (uniformly weighted) of AGN and inactive galaxy sample are illustrated as bold red and blue lines, respectively. Beyond 150 pc, there is only one inactive galaxy NGC 4224 that has measurements, others inactive galaxies being so close that their outer regions exceed our SINFONI FOV. On the other hand, below 20 pc, there is only two AGNs, ESO 137-34 and NGC 5728, that have measurements, others have non-stellar continuum that prevent us to extract the stellar kinematics. The typical error bars of the lines are the standard deviation at that radius and the radial bin size. We show the stellar kinematic properties with four quantities: inclination-corrected rotational velocity (top left), velocity dispersion (top right),  $v/\sigma$  (bottom left), and  $\sqrt{v^2 + \sigma^2}$  (bottom right). The velocities have been corrected for inclination based on the large-scale host galaxy inclination, which is listed in Table 3.1.

elliptical rings, each of which can be written as a finite sum of harmonic terms:

$$K(a, \psi) = A_0(a) + \sum_{n=1}^N A_n(a) \sin(n\psi) + B_n(a) \cos(n\psi) \quad (3.8)$$

where  $\psi$  is the azimuthal angle measured from the projected major axis in the plane of the galaxy, and  $a$  is the length of semi-major axis of the elliptical ring. The parameters  $A_n$  and  $B_n$  can be represented by the amplitude coefficient  $K_n = \sqrt{A_n^2 + B_n^2}$ . With respect to the shape of elliptical rings for our analysis, the PA is set to be the mean PA obtained in Section 3.5.2, the flattening ( $q$ ) is the axial ratio listed in Table 3.1, and the central position is fixed at the location given by the centre of the brightest continuum. For an ideal rotating disk, the rotational velocity and velocity dispersion fields are dominated by  $K_1$  and  $A_0$ . The rotational velocity has been corrected for the inclination listed in Table 3.1.

For the purpose here, to study the differences in stellar properties between AGNs and inactive galaxies, we plot in Figure 3.11 four quantities related to the stellar kinematics as a function of radius: velocity, velocity dispersion,  $v/\sigma$ , and  $\sqrt{v^2 + \sigma^2}$ . The approximate dynamics of a stellar system can be established by the velocity and velocity dispersion, which reflect the contributions of rotation and random motion. The relative contribution between these two motions is written as  $v/\sigma$  and indicates how disk-like or spheroidal the system is. To access the enclosed dynamical mass in the nuclear region, we use the quantity  $\sqrt{v^2 + \sigma^2}$ . The radius over which we can compare AGNs and inactive galaxies is in the range of 20-150 pc: most AGNs are affected by non-stellar dilution meaning the kinematic information cannot be extracted from the inner 20 pc, and most inactive galaxies are so close to us that the field of view does not extend over regions beyond 150 pc.

In Figure 3.11, we find that all the quantities are comparable between AGNs and inactive galaxies across 20-150 pc, suggesting that the nuclear stellar kinematics of the AGN sample are similar to those of the matched inactive galaxy sample. In an examination of the eight individual pairs, no specific trend toward the AGN or inactive galaxy sample is shown by any of the stellar kinematic quantities. In contrast, within a radius of 200 pc Hicks et al. (2013) found a large difference in  $\sigma$  and a smaller difference in  $\sqrt{v^2 + \sigma^2}$ , both of these quantities being smaller in the AGN sample compared to their inactive sample. The authors interpreted this to indicate there is a dynamical cold nuclear structure composed of a relatively young stellar population in the AGN sample.

There could be several reasons for these differing results. One possibility is the AGN selection method: we use solely the 14-195 keV luminosity to select AGN while Hicks et al. (2013) used Seyfert galaxies that meet the Revised Shapely-Ames (RSA) catalog magnitude requirement ( $B < 13.4$  mag). It is worth noting also that  $\log L_{14-195}$  of the AGNs in our sample is  $43.0 \pm 0.4$ , which is a factor of a few brighter than those in the Hicks et al. (2013) sample where  $\log L_{14-195}$  is  $42.4 \pm 0.4$  (and there is one AGN without a *Swift*-BAT detection). A second possibility is the limited sample size and the selection variation. In this study we use 8 AGN and 5 inactive galaxies while Hicks et al. (2013) use 5 AGN and 4 inactive galaxies in their kinematic comparison. As such, simple scatter in the individual properties at small scales could lead to the discrepancy. If all the objects in the LLAMA

sample are observed, we will be able to resolve this issue. A third possibility is the selection of the matched inactive galaxies. In both cases, this was done on parameters including galaxy integrated luminosity, Hubble type, inclination, bar, and distance. However, a difference is that we selected based on H-band luminosity while Hicks et al. (2013) used matched samples from Martini et al. (2003) that had been selected on B-band luminosity. Due to the reduced impact of extinction and stellar age on the luminosity in the near-infrared, the H-band is a more reliable proxy for stellar mass. Hicks et al. (2013) discussed this issue, and found that the H-band luminosity for their AGN was 24% less than in their inactive sample. If H-band luminosity does linearly trace mass as we expect, this could then lead to a  $\sim 12\%$  difference in kinematic tracers. This would reduce the difference in  $\sqrt{v^2 + \sigma^2}$  to a level where it is insignificant, but could not account for all the difference in  $\sigma$ . Nevertheless, it underlines the importance of careful matching of the control sample.

### 3.5.4 Central velocity dispersion

When looking at the nuclear stellar kinematics, some AGNs show a significant velocity dispersion drop, suggesting the presence of a dynamically cold nuclear component (Emmellem et al., 2001; Greene et al., 2014). Self-consistent  $N$ -body simulations interpret these stellar velocity dispersion drops in the nuclear region as a consequence of young stars born from the dynamically cold gas reservoir coming in from larger scales. As such, nuclear disk formation requires in-situ star formation, and it is kinematically cooler than the surroundings (Cole et al., 2014). The simulations further suggest the young stellar population (less than 0.9 Gyr) should be brighter than the old underlying population at near-infrared wavelengths (Wozniak et al., 2003). Adaptive optics observations with SINFONI have shown two AGN where this is seen (NGC 1097 and NGC 1068, Davies et al. 2007). And our new SINFONI observations can be used to test this interpretation further, as well as to assess whether a young stellar population commonly occurs in AGNs.

The nuclear stellar light excesses we have discussed in Section 3.4 exhibit an extended structure and a velocity field that indicates rotation, suggesting that they are nuclear disks. In particular, our data for the inactive galaxy NGC 3351 are consistent with the above mentioned simulations: it exhibits significant excess stellar light across the whole field of view, which is accompanied by an obvious central velocity dispersion drop to about  $\sim 50 \text{ km s}^{-1}$ . We can compare this to recent hydrodynamic simulations of the evolution of star formation as a result of gravitational instabilities in a nuclear gas disk (Schartmann et al. in prep.). These show that, because of the large number of interactions between gas clumps and as a result of scattering between stars and gas clumps, the stellar disk undergoes significant gravitational heating before it relaxes in the global potential of the bulge. These authors show that, in their simulation, the velocity dispersion can attain a constant value of  $\sim 40 \text{ km s}^{-1}$ .

In contrast to the case of NGC 3351, looking at the overall results of our sample, we surprisingly find the excess stellar light is not generally accompanied by the drop of stellar velocity dispersion toward the centre. These phenomena do not appear to correlate with each other, and the stellar velocity dispersion across the observable FOV is generally

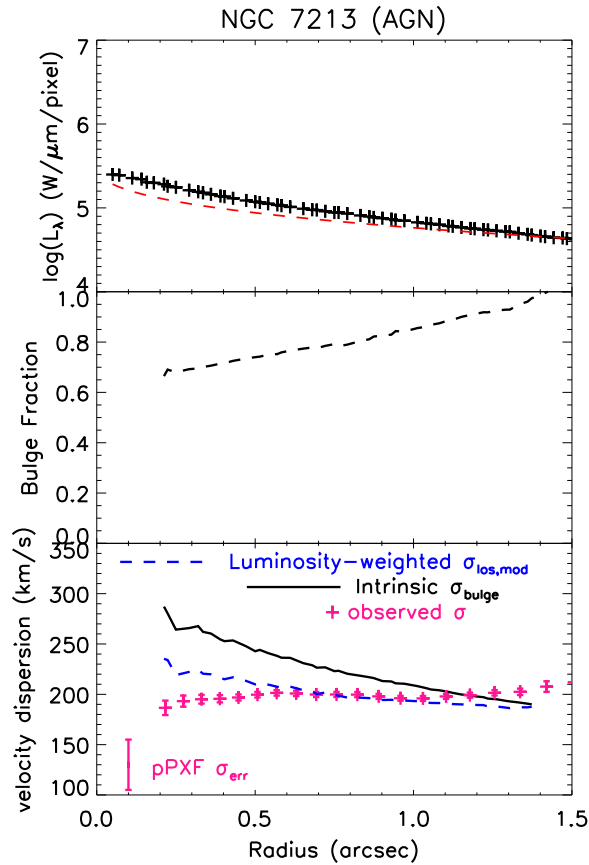


Figure 3.12: The best sample of simple toy model to explain the trend of radial stellar velocity dispersion. Top panel: The radial luminosity for observed data point (black pluses) and bulge component (red dashed line). Middle panel: The bulge fraction as a function of radius. Bottom panel: The radial stellar velocity dispersion with radius. The black solid line represents the intrinsic bulge velocity dispersion, which is calculated based on the bulge surface brightness profile. Considering the contributions come from both a dynamically hot bulge population (typical is several hundred  $\text{km s}^{-1}$ ) and a dynamically cold young star population (we assume  $40\text{-}50 \text{ km s}^{-1}$ ), the luminosity-weighted velocity dispersion is presented in blue dashed line. Pink pluses are the observed data with the error bar representing the  $1\text{-}\sigma$  error with respect to the velocity dispersion inside the 2-D elliptical rings at specific radius. We attached the pPXF return mean stellar velocity dispersion error ( $25 \text{ km s}^{-1}$  in average) in the bottom left corner.

rather uniform. This observational evidence is quite distinct from the Wozniak et al. (2003) simulations, Figure 9 and 10 of their paper present that the stellar velocity dispersion drops with the increasing contribution of young (dynamically cold) stellar population. Once the mass density of the young population significantly overtakes the old population, the drops of stellar velocity dispersion can be easily seen. Looking at our data, the reason why we do not see the clear velocity dispersion drops in the central hundred pc scales, is probably because the contribution of old stars dominates over the young stars. To test this scenario, we describe a simple toy model to interpret the LOS velocity dispersion.

Based on the hydrodynamical disk models,  $\sigma_{los}$  (line-of-sight velocity dispersion) can be projected into  $\sigma_R$  (azimuthally average radial dispersion),  $\sigma_\theta$  (tangential average radial dispersion), and  $\sigma_z$  (vertical average radial dispersion) in cylindrical coordinates. The  $\sigma_R$  and  $\sigma_\theta$  are parallel to the disk plane, their contribution is marginal when the disk close to face-on (inclination  $\sim 0^\circ$ , i.e. the angle between line-of-sight and the disk is  $90^\circ$ ; see Equations (28) and (29), and Figures (7) and (8) in Tempel & Tenjes 2006). For simplicity, we assume that the simple toy models are all close to face-on. Then  $\sigma_{los}^2$  can be seen as  $\sim \sigma_z^2$ , in which the vertical velocity dispersion ( $\sigma_z(r)$ ) can be derived from the surface density  $\Sigma(r)$  in the disk:

$$\sigma_z^2(r) = 2\pi G \Sigma(r) h_z \quad (3.9)$$

where  $h_z$  is the scale-height of the disk. Although this may vary with radius, we assume the disk models have a constant  $h_z$  because in Section 3.3.2, we find that the bulges in our galaxies typically have  $n_{bulge} \sim 2$ , and hence are likely to be pseudo-bulges instead of classical bulges with  $n = 4$ . The bulge decomposition provides the bulge surface density profile which allows us to calculate the intrinsic velocity dispersion of bulge ( $\sigma_{bulge}$ ). In addition, we set a second velocity dispersion ( $\sigma_{new}$ ) to represent the young stellar population with a lower velocity dispersion of 40-50 km s<sup>-1</sup>. Adopting Equation (1) from Wozniak et al. (2003), the line-of-sight velocity dispersion predicted by the toy model is weighted by the luminosity of two components (i.e. bulge and nuclear excess). It can be expressed as:

$$\sigma_{los,mod}^2(r) = \sigma_{z,bulge}^2(r) \times \left( \frac{L_{bulge}(r)}{L_{total}(r)} \right) + \sigma_{z,new}^2(r) \times \left( 1 - \frac{L_{bulge}(r)}{L_{total}(r)} \right) \quad (3.10)$$

We apply this toy model to all objects and find that in its simplest form above, it can already explain the observed trend of velocity dispersion for NGC 7213 (AGN), which is presented Figure 3.12. This galaxy has strong nuclear excess stellar luminosity. By checking its galactic plane inclination, we find NGC 7213 is close to face-on ( $26^\circ$ ), which is consistent with one of the assumptions in our simple toy model. Inspection of Figure 3.12 shows that the bulge contribution still dominates among the whole FOV, with the result that the kinematic signature of the young stars is dominated by that of the old stars, and hence the lower velocity dispersion from the young population is hidden by the dynamically hot galactic bulge. Thus we can argue that we would not expect to see a clear stellar velocity dispersion drop in the centre. But, because we do not know the true intrinsic radial dispersion profile of the (pseudo-)bulge, we also cannot claim that the excess stellar luminosity must be associated with a dynamically cooler stellar population.

There is another explanation that most of the stars embedded in nuclear disk have not formed recently, and this stellar component is not dynamically cold anymore. Sarzi et al. (2016) find that the age of hot nuclear stellar disk in elliptical galaxy NGC 4458 is at least 6 Gyr old, while Corsini et al. (2016) measured the age of the nuclear stellar disk in the SB0 galaxy NGC 1023 is about 2 Gyr. On the other hand, spectral synthesis fits to the detailed XSHOOTER spectra of the LLAMA sample (Burtscher et al. in prep.) show that while an old population dominates the optical continuum, a younger component with an age of 0.1–1 Gyr is nearly always present at a level of a few to 20%.

Besides the question of whether the young stellar population is dynamically cold, a second issue concerns whether there is a difference between active and inactive galaxies. In this study, while we find there is not any significant difference in stellar surface brightness and stellar kinematics between AGNs and most inactive galaxies. Neither VLT SINFONI observations nor Keck OSIRIS observations show any AGN with stellar surface brightness below  $10^3 L_{\odot} \text{pc}^{-2}$  in the central 50 pc, which is unlike inactive galaxy covering a wider range of surface brightness. Indistinguishable features between AGNs and inactive galaxies in photometric and kinematic characteristics suggest that the nuclear stellar properties are generally comparable. This suggests that the timescale of switching AGN activity on and off, especially X-ray activity, is shorter than the timescale to form nuclear stars. On the other hand, from the perspective of individual galaxies, we find that NGC 3351 has two components of nuclear stellar excesses, together with a significant velocity dispersion drop toward the centre, indicating recent star formation around the galactic nucleus. These properties are similar to those reported in previous studies about recent star formation around AGN in Seyfert galaxies (e.g. NGC 3227 in Davies et al. 2006). It implies that, although they may be indications of gas inflow which triggers star formation and then feeds the AGN, there could still be a discrepancy between the timescales of these phenomena, with the AGN switching on and off multiple times during the period in which the nuclear stars can still be seen.

### 3.6 Conclusions

We use SINFONI data of a complete volume limited sample of bright local Seyferts, selected from the 14-195 keV *Swift*-BAT catalog. These AGNs have been assigned a matched sample of inactive galaxies, in which the host galaxy properties (stellar mass, Hubble type, inclination, presence of a bar) share a similar distribution. In this paper, we present an analysis of the spatially resolved stellar luminosity and kinematics for a sample of 8 pairs of matched active and inactive galaxies, covering their central few hundred parsecs. Observations on this scale enable us to approach the galactic nucleus and search for a young stellar population, which simulations suggest should be brighter at near-infrared wavelengths and dynamically colder than the old population in the large-scale bulge. The main findings from the kinematic and photometric perspectives are as follows:

1. An apparent bimodality has been observed in the nuclear equivalent width of the stellar CO feature (CO EW) in nearby galaxies. Inactive galaxies show almost a constant

CO EW across the entire SINFONI 3'' field of view, while most AGNs suffer from a strong non-stellar continuum contribution toward the centre, that dilutes the stellar light. For two AGNs (ESO 137-34 & NGC 5728) the CO EW is nearly constant across the whole field, suggesting there is no non-stellar contamination in the nuclear region.

2. We find that the central (within the inner 1.5'' radius) stellar light distribution typically does not follow the Sérsic profile fitted to the larger scale bulge, and this difference can be classified as excess or deficit behaviour. Most of our galaxies show an excess corresponding to a few percent of the total stellar luminosity within approximately a 3'' aperture; and the excess components show a clear relation of  $L \sim R^{0.5}$  which suggests surface brightness is constant across different galaxies.
3. The nuclear stellar photometry indicates that, except for the NGC 4254 and NGC 3351, the mean stellar surface luminosity of AGN is generally similar to the matched sample of inactive galaxies. We do not see any AGN with stellar surface brightness below  $10^3 L_{\odot} \text{pc}^{-2}$  in the central 50 pc, while in contrast the inactive galaxies cover a wider range of surface brightness.
4. The stellar kinematics of the AGN and inactive galaxy samples show regular rotation patterns like typical disk-like systems, with a kinematic position angle that is in agreement with the photometric one fitted from large-scale near-infrared images. There is no direct evidence of a dynamically cold component (which can be seen as the young stellar population) in the stellar population; but we also show that one would not necessarily expect to see a central drop in the velocity dispersion. There is no indication, either when looking at the whole sample or individual pairs, for any difference in stellar kinematics between the AGN sample and the matched sample of inactive galaxies within a radius of 150 pc.



# Chapter 4

## Asymmetric velocity dispersion

*This chapter presents results that have not yet been published.*

### 4.1 Motivation

Chapter 3 presented the 2D kinematics analysis based on the stellar CO(2-0) absorption feature, we found no evidence for a difference in the stellar kinematics and stellar surface brightness between AGN and inactive galaxies, suggesting the timescale of switching AGN activity on and off, especially X-ray activity, is shorter than the timescale to form nuclear stars. After carefully examining the stellar kinematics maps, an asymmetry in the velocity dispersion field is found in a few AGNs. This can be clearly seen in the left panel of Figure 3.2-3.3, where a lopsidedness in the stellar velocity dispersion along the major axis for NGC 5728, NGC 7172, and NGC 7582. A similar phenomenon has been discovered, however without any further discussion and analysis. We show the asymmetry signature is real and not a weird effect related to CO (2-0) absorption bandhead fitting or a by-product of the data reduction process. In the following, we report on the peculiar stellar velocity dispersion gradient from our SINFONI observations as well as summarize independent observations from the literature (4 AGNs in total with 3 of them in the LLAMA sample, the basic properties of the host galaxies and the AGN classification have been presented in Table 3.1).

1. NGC 5728: The bottom right panel of Figure 3.2 shows the peculiar gradient in the 2D stellar velocity dispersion field along the major axis PA of  $\sim 10^\circ$ , where the stellar dispersion changes from  $\sim 130 \text{ km s}^{-1}$  in the North(N) side to  $\sim 170 \text{ km s}^{-1}$  in the South(S) side. The regions of high stellar velocity dispersion match the red-shifted portion of the rotating nuclear stellar disk. Emsellem et al. (2001) first discovered the kinematical asymmetries along the major axis PA of  $\sim 10^\circ$  using the CO(2-0) absorption feature with the ISAAC/VLT spectrograph. In contrast to the small scale SINFONI data cube, Emsellem et al. (2001) found that the velocity dispersion reaches  $\sim 220 \text{ km s}^{-1}$  in the N side at a distance of 450 pc from the centre, coinciding with the blue-shifted side of the rotating nuclear stellar disk.

2. NGC 7172: The 2D stellar velocity dispersion field (right panel, second row of Figure 3.3) shows a peculiar gradient along the major axis PA of  $\sim 90^\circ$ . The stellar dispersion changes from  $\sim 110 \text{ km s}^{-1}$  in the West(W) side to  $\sim 180 \text{ km s}^{-1}$  in the East(E) side. The regions of high stellar velocity dispersion match to the blue-shifted part of the rotating nuclear stellar disk.
3. NGC 7582: The bottom right panel of Figure 3.3 shows the peculiar gradient in the 2D stellar velocity field along the major axis PA of  $\sim 155^\circ$ , where the stellar dispersion changes from  $\sim 45 \text{ km s}^{-1}$  in the Northwest(NW) area to  $\sim 115 \text{ km s}^{-1}$  in the Southeast (SE) corner. The regions of high stellar velocity dispersion match the blue-shifted side of the rotating nuclear stellar disk. Note that these high velocity dispersion components in the SE corner have been detected in the  $\text{H}_2$  emission as well. In addition, the low stellar velocity dispersion components can be seen in the West side on the top right panel of Figure 4 in Riffel et al. (2009) where they analyzed the CO(2-0) absorption feature with GNIRS/Gemini (because the GNIRS FOV is rectangular, it does not cover the high stellar velocity dispersion regions).
4. NGC 4501: A nearby Seyfert 2 galaxy (inclination =  $63^\circ$ ), its host galaxy is classified as Sab (de Vaucouleurs et al., 1991) and it is one of the largest spiral galaxies in Virgo cluster, with good evidence it is undergoing a current ram pressure stripping event leading to the truncation of the outer gas disk near the optical radius ( $R_{25}$ ) (Vollmer, 2009). Mazzalay et al. (2014) studied the kinematics of the  $\text{H}_2$  emission line and the stellar absorption features, based on AO-assisted integral-field observations obtained in the K band with SINFONI/VLT. The lower-right panel of Figure 12 in Mazzalay et al. (2014) shows that there is a peculiar gradient in the 2D stellar velocity dispersion field along the major axis of  $\sim 140^\circ$ , where the stellar velocity dispersion changes from  $\sim 80 \text{ km s}^{-1}$  in the SE area to  $\sim 130 \text{ km s}^{-1}$  in the NW corner. The regions of high stellar velocity dispersion coincide with the blue-shifted side of the rotating nuclear stellar disk.

In this chapter, we present the techniques to quantify the asymmetry of the stellar velocity dispersion along the major axis and assess the difference in stellar velocity dispersion between the AGN and the matched inactive galaxy sample (Section 4.2). Furthermore, we discuss various physical interpretations for the observed asymmetry in the stellar velocity dispersion field (Section 4.3).

## 4.2 Methods to quantify the asymmetries

In these Sections, we use two different methods to quantify the velocity dispersion asymmetry along the major axis. The first method is searching for an overall kinematic asymmetry within a given elliptical ring at a certain radius. This method quantitatively evaluates the dynamical state of a system and, consequently, reflects the dynamic complexity of a system. Since we already know there is a significant asymmetry in the 2D stellar velocity dispersion

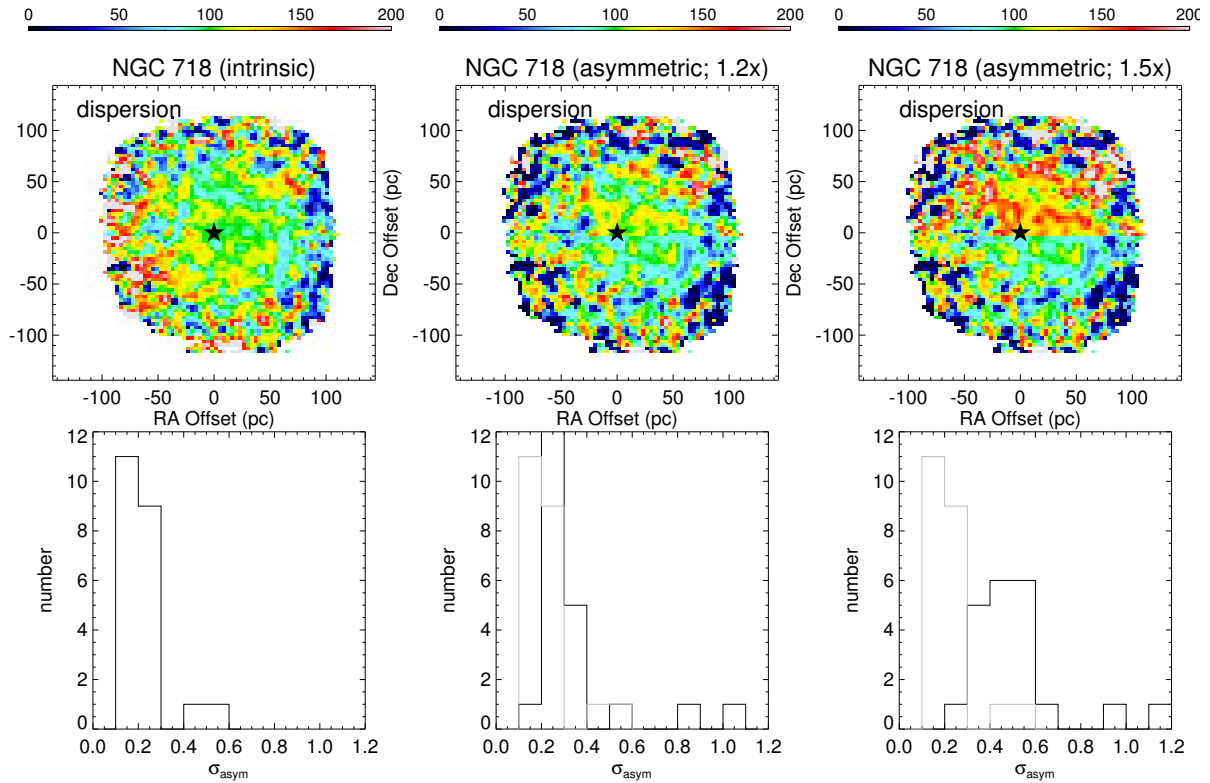


Figure 4.1: Testing the impact of the simulated velocity dispersion asymmetry on  $\sigma_{asym}$ . The upper row is the 2D stellar velocity dispersion maps. The right-hand panel is the intrinsic data, while the middle and the left-hand panels are the magnified data where the dispersion in the North side has been increased by a factor of 1.2 and 1.5, respectively. The peak position of stellar continuum is marked as a black star. The lower row is the histogram of measured  $\sigma_{asym}$  from *kinemetry* output coefficients. Higher values mean more asymmetric. In order to compare easily, the intrinsic  $\sigma_{asym}$  distribution is overplotted in grey colour in lower middle and lower right panels.

field in NGC 5728, NGC 7172, and NGC 7582, the second method is determined by counting a two-sided asymmetry along the major axis. In addition, we assess asymmetries and compare the difference between AGN sample and the matched sample of inactive galaxies.

### 4.2.1 Quantifying asymmetries with *kinemetry*

In Section 3.5.3, we used the IDL routine *kinemetry* to extract radial distributions for the velocity and velocity dispersion from the 2D kinematic maps. The line of sight velocity and velocity dispersion can be divided into several elliptical rings, which can be described as an expansion of a series of harmonic terms (refer to equation 3.8). The rotational velocity and velocity dispersion are dominated by  $K_1$  and  $A_0$  if we assume it is an ideal disk, while the higher order kinematic coefficients ( $K_{2,v}$ – $K_{5,v}$  and  $K_{1,\sigma}$ – $K_{4,\sigma}$ ) may be caused by the noise

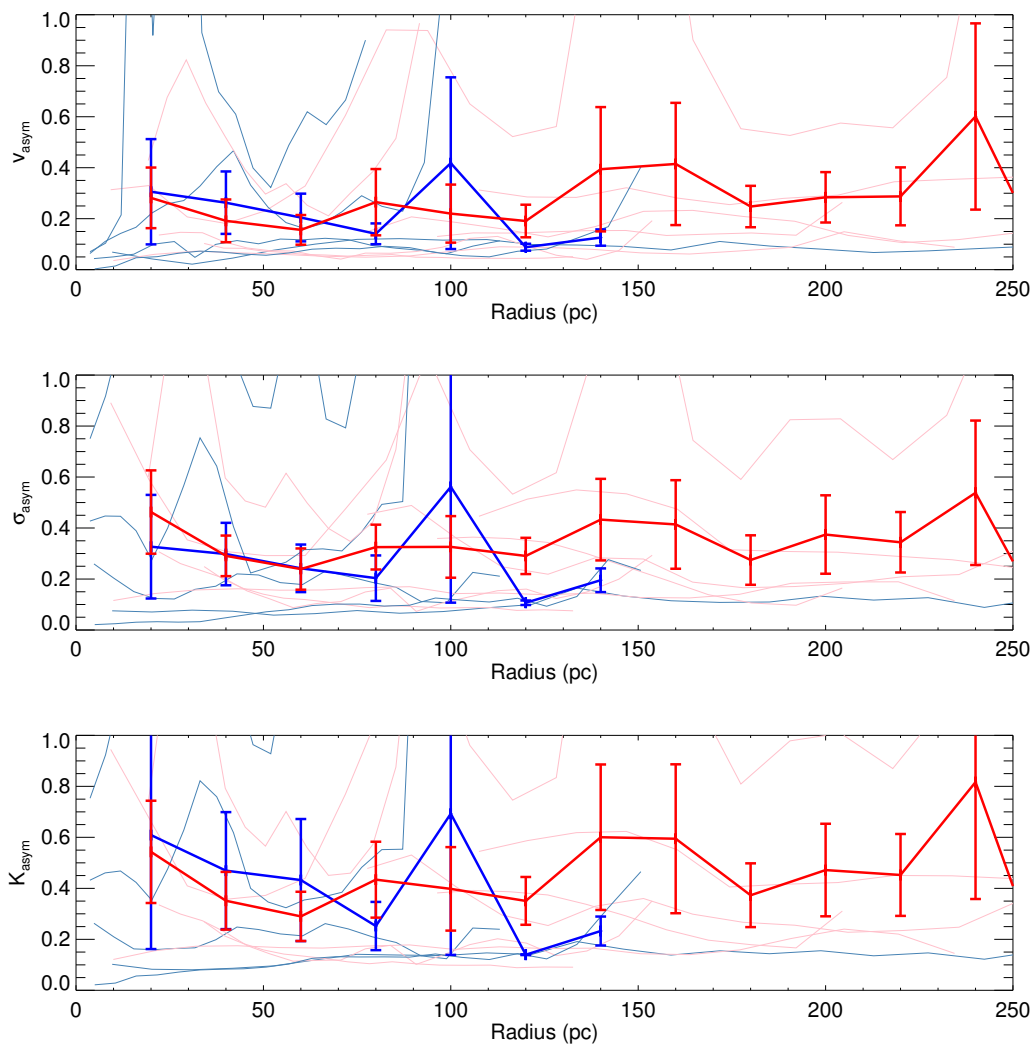


Figure 4.2: The  $v_{asym}$ ,  $\sigma_{asym}$ , and  $K_{asym}$  as a function of radius. Red and blue lines represent the AGN sample and the matched inactive galaxy sample. The mean value (uniformly weighted) of AGN and inactive galaxy sample are illustrated as bold red and blue lines, respectively. No evidence for any difference between AGNs and inactive galaxies. Most inactive galaxies are so close to us that there is only one inactive galaxy NGC 4224 has measurements beyond 150 pc.

as well as additional asymmetries (Shapiro et al., 2008).

Based on the definition of asymmetry in Shapiro et al. (2008), the level of deviation from an ideal disk in the velocity field can be written as:

$$v_{asym} = \left\langle \frac{k_{avg,v}}{B_{1,v}} \right\rangle \quad (4.1)$$

where  $k_{avg,v} = (k_{2,v} + k_{3,v} + k_{4,v} + k_{5,v})/4$ . By normalizing  $k_{avg,v}$  to  $B_1$ , then a system will roughly retain the same amount of detectable asymmetry regardless of the radial content of the data. The level of deviation from an ideal disk in the velocity dispersion field can be expressed as:

$$\sigma_{asym} = \left\langle \frac{k_{avg,\sigma}}{B_{1,v}} \right\rangle \quad (4.2)$$

where the  $k_{avg,\sigma} = (k_{1,\sigma} + k_{2,\sigma} + k_{3,\sigma} + k_{4,\sigma} + k_{5,\sigma})/5$ . A proper way to systematically quantify the asymmetry in velocity dispersion is to normalize the  $k_{avg,\sigma}$  to  $B_1$ , which is a reliable measurement of the system's mass. The total kinematic asymmetry  $K_{asym} = (v_{asym}^2 + \sigma_{asym}^2)^{1/2}$  has been appropriately applied to separate disk galaxies and interacting systems using several empirical thresholds (e.g. Shapiro et al. 2008; Bellocchi et al. 2012; Hung et al. 2015).

To assess the impact of the velocity dispersion asymmetry on  $\sigma_{asym}$ , we produced a simple test to simulate  $\sigma_{asym}$  for the velocity dispersion asymmetry along the major axis. We start with NGC 718, an inactive galaxy with a uniform stellar velocity dispersion field and slightly magnify one-side of the dispersion by a factor of 1.2 and 1.5, corresponding to an additional dispersion of  $\sim 20 \text{ km s}^{-1}$  and  $50 \text{ km s}^{-1}$ . The magnified data is then treated with the same procedure as for the intrinsic data, calculating  $\sigma_{asym}$  along a *kinemetry* ellipse in the dispersion map at different radii. The results are presented in Figure 4.1. The left-hand side is the intrinsic data, while the middle and the right-hand side are the magnified data. The upper panels show the 2D velocity dispersion maps and the lower panels present the histogram of  $\sigma_{asym}$ . When one-side of the velocity dispersion field is increased, the asymmetry becomes more visible in 2D maps and consequently  $\sigma_{asym}$  is distributed towards higher values.

We measure the  $v_{asym}$ ,  $\sigma_{asym}$ , and  $K_{asym}$  as a function of radius for the LLAMA sample in Figure 4.2. There is no obvious difference in the asymmetry quantities between AGNs (red bold line) and matched inactive galaxies (blue bold line), suggesting this method cannot properly select an AGN sample based on asymmetry in the stellar velocity dispersion field. The reason leading to this result is that, although lopsidedness can be recorded in  $\sigma_{asym}$ , other structures such as a bar, radial flows, warped disk, and other multi-components also can generate additional deviations in the higher order coefficients, and increase  $\sigma_{asym}$ . Both AGNs and inactive galaxies have nuclear regions (below 150 pc) with total kinematic asymmetry  $K_{asym} \sim 0.5$ , which falls between that of a disk galaxy and merging system (Shapiro et al., 2008). This implies the dynamical state in the nuclear regions of AGNs and inactive galaxies are more complex than a disk galaxy, but unlikely similar to an extreme case of a merging system (i.e. major mergers).

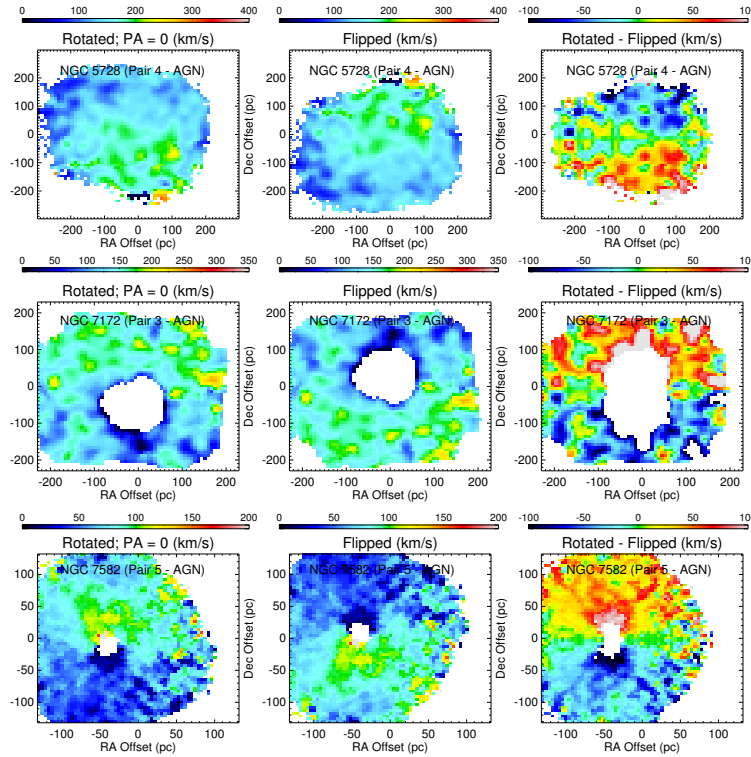


Figure 4.3: Examples of quantifying the velocity dispersion asymmetry for the AGNs with the flip-subtract technique. We rotate the major axis of velocity dispersion map to  $PA = 0^\circ$  for a better display purpose (left-hand side panels). The middle panels are the left panels flipped over the horizontal axis (i.e. the flipped velocity dispersion maps). The residual maps are presented in the right-hand side panels, which are the intrinsic dispersion maps subtracted by the flipped ones. Same as Figure 3.2, we truncate the central regions in which are dominated by the non-thermal continuum. Inside this regions, any kinematic measurement by CO(2-0) stellar absorption is unreliable.

#### 4.2.2 Quantifying asymmetries with a flip-subtracted image

Ho et al. (2016) developed the flip-subtract technique to quantify the velocity asymmetry across a galaxy's minor axis to trace galactic winds and disk-halo interactions. We follow a similar idea but slightly revise the method in order to fit our purpose, looking for a velocity dispersion asymmetry along the major axis. Here are the two steps:

1. Flip the pixel to pixel velocity dispersion map along the minor axis.
2. Subtract the flipped velocity dispersion map from the original velocity dispersion map and measure the residuals as a function of radius.

Figure 4.3 illustrates the methodology applied to the AGN sample. We use 3 AGNs (NGC 5728, NGC 7172, and NGC 7582) in which the velocity dispersion asymmetries are

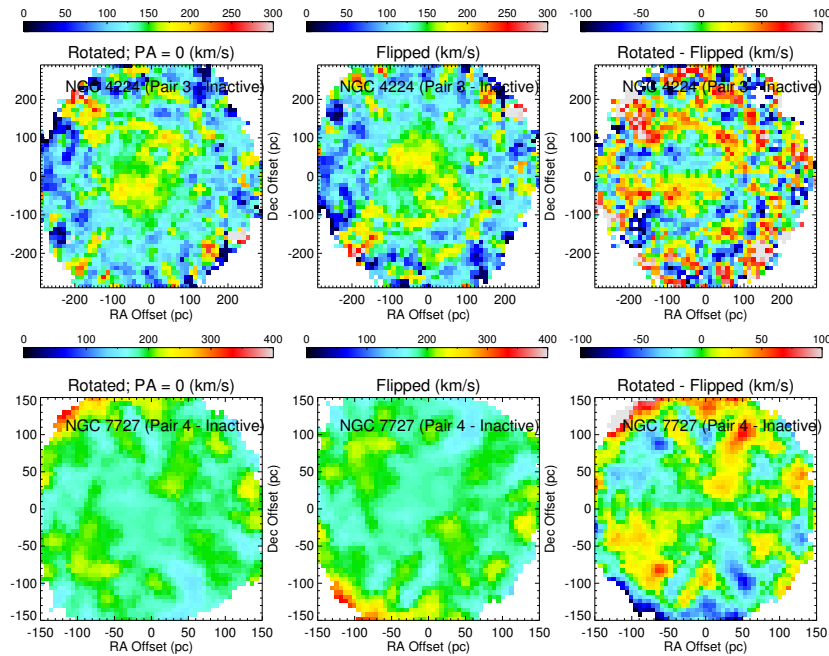


Figure 4.4: Same as Figure 4.3 but for the matched inactive galaxies. There is no non-stellar continuum to dilute CO(2-0) stellar absorption, thus the kinematics can be simply extracted toward the centre.

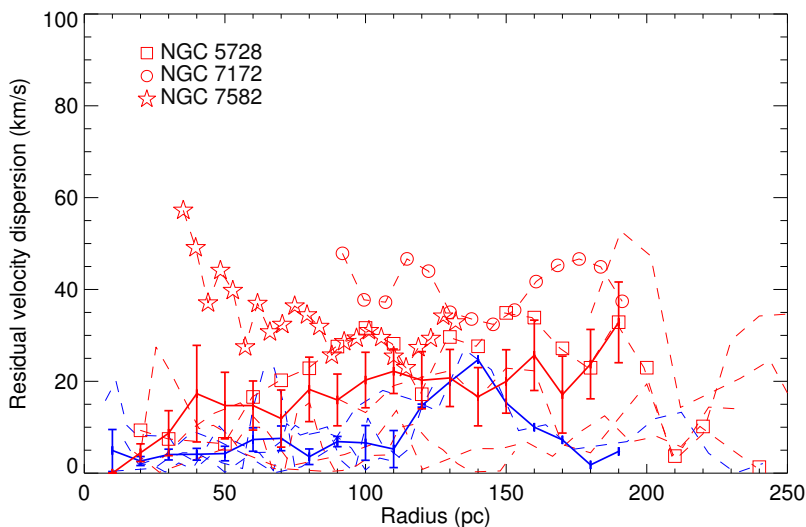


Figure 4.5: The residual velocity dispersion as a function of radius. The AGN sample and the matched inactive galaxy sample are presented as red and blue colour, respectively. Each dashed line indicates the individual galaxy, while the bold lines are the uniformly weighted mean values. NGC 5728, NGC 7172, and NGC 7582 are labelled, in which their asymmetry is directly visible in 2D velocity dispersion map.

clearly visible in the 2D maps. We also applied the same procedure to those matched inactive galaxies, NGC 4224 and NGC 7727, and show them in Figure 4.4. This method can directly reflect the asymmetric velocity dispersion gradient along the galaxy major axis. We measured the asymmetric residual as a function of radius for all samples and presented them in Figure 4.5. Although we do not use the full LLAMA sample (20 AGNs and 19 matched inactive galaxies), with the current available data (8 AGNs and 5 matched inactive galaxies), we see a strong asymmetric residuals only occur in the AGN sample. In contrast, the matched inactive galaxy sample shows a relatively uniform distribution. These conclusions will be revisited once the full sample is available.

### 4.3 Discussion: the plausible origin of the asymmetries

Several effects can produce such an apparent asymmetry in the stellar velocity dispersion along the galaxy major axis. An explanation of variable extinction, as suggested by Wagner et al. (1989), seems unlikely because that would require the dust lane to be parallel to the direction of the dispersion gradient. In NGC 7172 and NGC 7582, we observed a dust lane across the major axis which induces asymmetric stellar continuum light along the minor axis, but such asymmetry along the minor axis does not appear in any kinematic maps.

A more plausible scenario is that the radial stream motion of gas from one side of the galaxy is more efficiently moving inward to the centre, which could result in distinct dynamical friction on the two sides of the galaxy. Such different dynamical friction causes different gravitational drag on each star behind the gas and implies an increasing anisotropy in the stellar velocity dispersion field. We also find that the velocity dispersion asymmetry usually occurs in those AGNs in which their host galaxy is highly inclined. This may be evidence to support the radial stream motions scenario. Comparing to face-on (low-inclination) systems, we can easily observe radial flows in edge-on (high-inclination) systems because they are superimposed on our line of sight. In the following, we investigate the nuclear environment of individual galaxies which may be associated with radial inflow:

1. Nuclear ring structures: NGC 5728 and NGC 7582 both have a nuclear ring, which is the manifestation of the inner Lindblad resonance and formed by inflowing gas accumulation. Riffel et al. (2009) spatially and spectrally resolved the nuclear ring of NGC 7582, which contains active star formation producing strong Br $\gamma$  emission at a projected radius of 1.7'' from the nucleus. The equivalent width of Br $\gamma$  indicates an age of  $\sim 5$  Myr. We present the distribution of H $_2$  2.12 $\mu$ m and Br $\gamma$  2.16 $\mu$ m emission lines in Figure 4.6. The ring structures are better traced by the H $_2$  emission, while the Br $\gamma$  clumps are composed of young stars located in the nuclear ring structure. For NGC 5728, Son et al. (2009) found the prominent nuclear ring structure has active star formation evidenced by H $\alpha$  emission at a projected radius of 5.4'' from the nucleus.

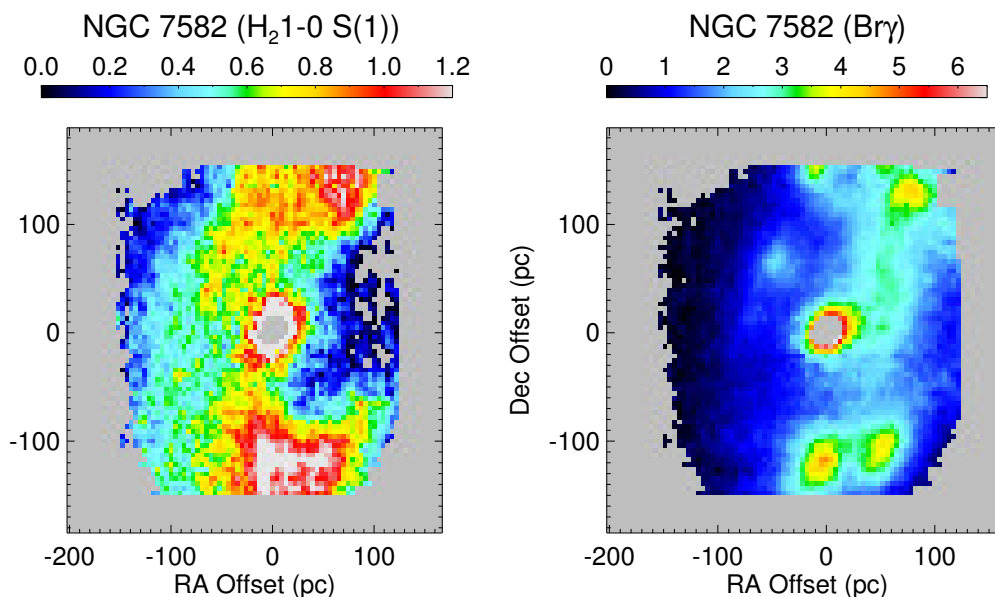


Figure 4.6:  $\text{H}_2$  2.12 $\mu\text{m}$  (left panel) and  $\text{Br}\gamma$  2.16 $\mu\text{m}$  (right panel) maps for NGC 7582. The bulk ring structures can be traced by  $\text{H}_2$  emission. The  $\text{Br}\gamma$  map presents the several clumps, which are composed of gas, and after star formation, of young stars.

2. Merging between intruder and target: NGC 5728 shows a double peak in  $\text{H}\alpha$ ,  $\text{H}\beta$ ,  $[\text{O III}]$ , and  $[\text{N II}]$  (Son et al., 2009), and these two peaks are classified as Seyfert nuclei based on optical emission line diagnostics (Ho et al., 1997b). The line profiles of  $[\text{O III}]5007$  show that the two cores both present underlying broad wings (one blue-shifted and one red-shifted), suggesting the presence of inflows (Figure 22 in Son et al. (2009)). Double Seyfert nuclei may indicate a merging event in the past. Once galaxies interact, the gas loses angular momentum anisotropically and moves toward the centre, resulting in asymmetric dynamical friction.
3. On the other hand, we cannot rule out a local supernova (SN) explosion, in which the SN rate well correlates with the velocity dispersion of the ISM. The galactic SN corresponds to a total gas velocity dispersion of  $\sim 8.5 \text{ km s}^{-1}$ , if the SN rate increases by a factor of 10, then the velocity dispersion will reach  $\sim 15 \text{ km s}^{-1}$  (Dib et al., 2006). This value is similar to the mean residual velocity dispersion of our AGN sample.

## 4.4 Conclusions

We find a stellar velocity dispersion asymmetry along the galaxy major axis, which frequently occurs in our AGN sample, rather than the matched sample of inactive galaxies. The asymmetry can be quantified through the flip-subtracted technique, showing there is

an additional stellar velocity dispersion of  $\sim 20 \text{ km s}^{-1}$  on one-side of the host galaxy. We argue that a stellar asymmetric velocity dispersion is induced by radial flows inward to the centre. Furthermore, we find there are several nuclear environments (e.g. nuclear ring structures and merging events) which may be associated with inflowing gas accumulation.

# Chapter 5

## Summary & Outlook

In this thesis, we have studied the nuclear environments of nearby Seyfert galaxies that can give essential insights into the co-evolution of the SMBH and the host galaxy. The state-of-the-art observational techniques available for creating high-resolution images, allow us to approach the nuclear regions for inside the host spheroidal bulge component. In addition to investigating what are the main mechanisms providing the gas reservoir to fuel the SMBH, we find the AGN-associated feedback acts on the nuclear regions of host galaxy.

### The nuclear environment traced by the dense molecular gas - Chapter 2

In the first part of this work, we focus on the molecular gas geometrical structure and its physical properties in the central  $\sim 100$  pc around AGN. We present 3mm interferometer data from the IRAM PdBI, which has spatially resolved the HCN(1-0) and HCO+(1-0) dense molecular lines of three nearby Seyfert galaxies: NGC 3079, NGC 6764, and NGC 5033. The observed kinematics of Seyfert galaxies have been reconstructed by modelling a rotating disk in which the spectral and spatial smearing effects are taken into account. After combing our kinematic analysis with archive data, we find that in 7 out of 8 Seyfert galaxies have geometrically thick molecular disks,  $\sigma/v \geq 0.3$ . This result suggests that there may have powerful sources that can provide additional energy to maintain the disk thickness. A analysis of the HCN(1-0)/CO(2-1) and HCN(3-2)/HCN(1-0) line ratios in archive data NGC 6951 shows that the dense molecular gas is not in self-gravitating molecular clouds. The implied pressures of  $P/k \sim 10^7$  cm<sup>-3</sup> K is comparable to that measured in an environment dominated by supernovae. In addition, the spectrum of NGC 3079 has numerous absorption lines, which are characterized by a double peak profile. One close to the systemic velocity is caused by a absorption in the blue-shifted side of the inner disk, which lies in front of a milliarcsec-scale radio jet. Another absorption with a broad blue-shifted wing extending to 350 km s<sup>-1</sup> implies the existence of a nuclear outflow. The SiO(2-1)/HCN(1-0) line ratio in NGC 3079 is similar to those values found in the perturbed clouds associated with supernova remnant. The above results suggest that the nuclear regions of nearby Seyferts tend to have post-starburst populations, whether star formation is still ongoing or has cease. We also find an unexpected relation between HCN

luminosity and dynamical mass, which implies a correlation of the gas fraction and  $\alpha_{HCN}$  (the conversion factor from HCN luminosity to gas mass). The observed relation can be explained by a gas fraction of 10% and  $\alpha_{HCN} \sim 10$ .

### Future Work

Radiation, outflows, and jets from AGN result a considerable feedback of energy and momentum into interstellar medium(ISM), by quenching star formation the host galaxy becomes red and gas-poor. The direct observational feedback can be classified as two mechanisms: radiative (quasar mode) or kinematic (radio mode) (Fabian, 2012). The radiative mechanism occurs in the luminous AGN with its supermassive black hole (SMBH) with high accretion rate. In contrast, the kinematic mechanism happens when the SMBH accretes at a lower accretion rate, and is associated with powerful radio jets that can efficiently heat the circumgalactic and halo gas. However, the kinematic mechanism also has positive feedback to the host galaxies, by compressing ISM, AGN outflows can trigger host galaxy star formation. Recent hydrodynamic simulations of interaction between AGN jets and a dense ISM support this idea, showing that compared to high power radio jets launch strong outflows, low power radio jets are less efficiency at accelerating ISM clouds but play a significant role in affecting the evolution of the ISM and the star formation in the host galaxy (Mukherjee et al., 2016).

NGC 3079 has been observed in the CO(2-1) molecule at 230GHz on February 2011. However the 1 hr telescope time is not sufficient to cover a whole uv-coverage for the source, thus the dirty image shows a severe fringe pattern. After preliminary analysis, the final image shows at least two structures, differing from what we have seen with HCN(1-0) observations. One has the same position angle as the milliarcsec-scale water maser disk (P.A.  $\sim 0$  deg), while another is likely to be the nuclear outflows, an outcome of jet-ISM interactions, which is aligned to the ionized [N II] filament (P.A.  $\sim 35$  deg). I have had a proposal accepted to spatially and spectrally resolve the nuclear outflows along the AGN radio jet, with direct implication on our understanding of how the nuclear ISM and the low power radio jets interact with each other.

- *To clarify the connection between nuclear jet-ISM interactions and kpc-scale starburst driven super bubble (Figure 2.9 for detail sketch).* Combining the molecular gas mass traced by CO luminosity with spectrally resolved outward velocity, we can robustly measure the kinematic energy and compare the nuclear outflows to those at different scales across the host galaxy: from kpc-scale super bubble (H $\alpha$  emission) - few hundred pc scale ionized filament ([N II] emission) - less than 100pc scale HCN broad absorptions (partly spatially resolved in the south-east side) - low power radio jet (two continuum peaks at 22 GHz, separated by few milli-arcsec).

- *To determine whether the interactions between outward radio jets and ISM can puff up the thickness of dense molecular disk.* Current simulations show the geometrical thick molecular disk can be produced by the turbulence injected via supernova, suggesting recent star formation events may occur in the nuclear region. Without this, the short free fall

time of  $\sim 10^5$  yr leads the dense molecular gas to collapse into a geometrically thin disk. Some observations in the nuclear region do support the ongoing star formation (Riffel et al. 2009), others point out it is more likely to be post-starburst population (Davies et al. 2007). The high resolution afforded by NOEMA is key to answer why such geometrically thick structure can be found in the galaxy without any ongoing star forming. The nuclear outflows resulting from the interactions between outward radio jets and the ISM can be an alternative to current popular simulations involving star formation.

---

**The connection between nuclear star formation and AGN from the stellar perspectives** - *Chapter 3 & 4*

---

In the second part of this work. We focus on the stellar kinematics in the nuclear regions for a sample of local 14-195 keV selected AGNs and inactive galaxies, matched by their host galaxy properties. The sample of inactive galaxies is used as a scientific control in comparison to the AGN sample. Our aim here is to understand whether there is any evidence of the nuclear star formation associated with AGN fuelling process. According to the simulations, the nuclear star formation (young stellar component) is expected to have additional stellar light and lower velocity dispersion inside the galaxy bulge. We reconstruct the near-infrared IFU data cube from the SINFONI instrument with AO mode on the VLT and measure the stellar kinematics and photometry based on the CO(2-0) absorption bandhead. The angular coverage corresponds to the physical radius in a range of 10-150 pc, with a spatial resolution of  $\sim 10$  pc. An apparent bimodality has been observed in the nuclear equivalent width of the stellar CO feature (CO EW) in nearby galaxies. Inactive galaxies show a generally constant CO EW over the entire SINFONI field of view, while most AGN suffer from a strong non-stellar contribution toward the centre that dilutes the stellar continuum. After correcting the non-stellar AGN contribution from the observed nuclear stellar photometry and except the two outliers (NGC 4254 and NGC 3351), we find that the mean stellar surface luminosity of AGN is generally similar to the matched sample of inactive galaxies. In addition, we do not find any AGN with the stellar surface luminosity below  $10^3 L_{\odot} \text{pc}^{-2}$  in the central 50 pc, implying the mechanism to trigger AGN only happens effectively in the galaxy which has higher stellar surface luminosity. After removal of the large-scale bulge contribution from the stellar continuum within the SINFONI field of view, we find that a nuclear stellar light excess with an extended nuclear disk structure, and which exhibits a size-luminosity relation. We expect the stellar light excess to be associated with a dynamically cooler young stellar population, however we do not see any significant stellar velocity dispersion drops. A reasonable explanation is that the fraction of new forming stars is too small to dominate over the old stars of the bulge component, for which the intrinsic stellar velocity dispersion increased toward the centre. To summarize the results above, we find the nuclear star formation is weak, or it has been stopped. There is no evidence for a difference in the stellar kinematics and stellar surface brightness between active and inactive galaxies. All suggest that the timescale of switching AGN fuelling process on and off, is shorter than the timescale for the nuclear star formation. Finally, we find an asymmetry in stellar velocity dispersion field along the

galaxy major axis. We interpret it as a result of asymmetric inflowing gas accumulation.

### Future Work

The SINFONI observations for the rest half of AGN and their matched inactive galaxies have been scheduled. In addition to completing the data reduction for coming SINFONI data, we also plan to reconstruct dynamical models using the Jeans Anisotropic Models (JAM) method (Cappellari et al., 2010). The measured dynamical mass will help us to constrain the  $M/L_K$  ratio, which is an age indicator of the stellar population. This result compares to the XSHOOTER nuclear stellar population, two independent methods enable us to have a complete picture of recent star formation history in the nuclear regions of nearby Seyfert galaxies and the matched sample of inactive galaxies. The black hole mass can also be constrained through the JAM dynamics modelling. The spectrally and spatially resolved stellar kinematics is one of the most reliable ways to determine the SMBH mass (Cappellari et al., 2010). The most compelling evidence for SMBH-host galaxy coevolution is the  $M-\sigma$  relation. The scatter in the  $M-\sigma$  relation is remarkably small for the spheroidal component of the elliptical galaxy, but the scatter for spiral galaxies is significant larger. There are some suggestions that this can be attributed to the fact that the bulge component in spiral galaxies does not always follow a classical bulge Sérsic profile. The vast majority of spiral galaxies have SMBH mass in the mass range of  $10^5-10^8 M_\odot$  quantitatively tend to have disk-like flat pseudo-bulges. The options for directly measuring the SMBH mass of pseudo-bulge spiral galaxies are quite limited, mostly they are based on water maser dynamics or emission-line widths in AGNs (e.g. reverberation mapping). Although the water maser dynamics is the most reliable measurement, it is only useful for galaxies which are gas-rich, star forming, and often with AGN emission. The reverberation mapping method measures the size of the BLR, and then determines the SMBH mass. However, when calibrating the reverberation-based SMBH mass, it requires a scaling factor, which is set by assuming AGNs follow the same  $M-\sigma$  relation. Our JAM dynamical modelling can constrain the SMBH mass from the observed stellar kinematics field, both for AGNs and inactive galaxies. It will provide important insights into the current SMBH-host galaxy co-evolution research.

# Appendix A

## *Chapter 3* - Disk, bar, and bulge decomposition

We present the GALFIT 2-dimensional decomposition results of bulge, bar, and disk from 2MASS Ks band image. The disk Sérsic index has been fixed to an exponential profile (e.g.  $n_{disk} = 1$ ). The detailed fitting procedure refers to Section 3.3.2.

Table A.1: (1) Galaxy name, upper rows are AGNs and lower rows are inactive galaxies; (2) Bulge Sérsic index; (3) Bulge effective radius; (4) Bulge position angle; (5) Bulge axis ratio; (6) Bulge to total ratio; (7) Disk effective radius; (8) Disk position angle; (9) Disk axis ratio; (10) Bar Sérsic index; (11) Bar effective radius; (12) Bar position angle; (13) Bar axis ratio.

(1) Galaxy name	(2) $n_{bulge}$	(3) $r_{e;bulge}$ (")	(4) $PA_{bulge}$ (°)	(5) $\epsilon_{bulge}$	(6) B/T	(7) $r_{e;disk}$ (")	(8) $PA_{disk}$ (°)	(9) $\epsilon_{disk}$	(10) $n_{bar}$	(11) $r_{e;bar}$ (")	(12) $PA_{bar}$ (°)	(13) $\epsilon_{bar}$
ESO 137-34	2.13	6.94	-45.0	0.75	0.22	27.15	[35.0]	0.91	0.31	8.02	[-16.0]	[0.3]
NGC 3783 <sup>a</sup>	1.24	1.45	[-20.0]	0.95	0.21	19.53	-21.0	0.80	0.5	12.27	[-20.0]	0.26
NGC 4593 (2MASS)	2.73	3.66	-85.0	0.83	0.41	38.64	71.0	0.57	[0.5]	37.65	55.0	0.29
NGC 4594 (HST)	1.67	8.1	[-85.0]	0.80	-	-	-	-	-	-	-	-
NGC 5728	1.1	4.02	3.7	0.92	0.23	48.85	32.0	0.37	[0.5]	42.5	34.0	[0.1]
NGC 6814	1.08	1.07	27.0	0.94	0.09	30.53	56.0	0.96	[0.5]	5.43	26.0	0.66
NGC 7172	1.16	3.55	-89.0	0.64	0.25	27.21	-84.0	0.50	-	-	-	-
NGC 7213	2.57	13.7	-16.0	0.96	0.7	39.72	80.0	0.86	-	-	-	-
NGC 7582	2.72	1.99	-35.0	0.68	0.28	50.21	-25.0	0.38	0.27	54.71	[-22.0]	[0.15]
NGC 718	1.32	2.09	-5.0	0.92	0.28	16.25	0.0	1.0	0.73	15.73	-27.0	0.42
NGC 3351	0.8	6.95	12.0	0.77	0.22	61.64	0.0	0.89	[0.5]	38.42	[-70.0]	0.3
NGC 4224	2.53	5.01	[55.0]	0.72	0.29	28.42	[55.0]	0.43	-	-	-	-
NGC 4254	1.99	12.79	65.0	0.74	0.19	41.44	69.0	0.88	-	-	-	-
NGC 7727	1.68	5.07	-80.0	0.72	0.36	22.86	10.0	0.95	[0.5]	12.73	[-90.0]	0.15

<sup>a</sup>: Adding PSF to take into account the central bright nucleus.

Brackets: We hold the components fixed to the values in order to optimally perform galaxy fitting.

# Appendix B

## *Chapter 3* - Radial flux and kinematics of individual galaxy

We show the radial flux along the major-axis PA (top and middle rows) and the average kinematics (bottom row) for each galaxy. Following is the description for each Appendix figures:

- *Top left panel:* The radial flux profile along the major axis of 2MASS Ks band image (black asterisk signs). The decomposed disk, bar, and bulge component are presented in blue dashed line, green dashed line, and red dashed line, respectively. The yellow solid line indicates the integrated radial flux profile. This plot together with 2MASS radial residual enables us to identify the non-fitted structures (e.g. spiral arms). The horizontal black dotted line represents a residual value equal to zero.

- *Top right panel:* The combined radial flux profiles along the major axis from the large scale 2MASS Ks image (black asterisk signs; at a radius  $\geq 2''$ ) and small scale SINFONI stellar continuum image (black plus signs; at a radius  $\leq 1.5''$ ). The HST F160W radial flux profile (orange plus signs) is added to reinforce the scaling factor between two different scales. The red dashed line represents the bulge Sérsic profile. The vertical black dotted line is the SINFONI AO mode PSF, FWHM radius of  $\sim 0.1''$ . This plot together with SINFONI (and HST) radial residual enables us to identify whether there is an excess toward the centre. The horizontal black dotted line represents a residual value equal to zero.

- *Middle left panel:* The radial flux profile of SINFONI stellar lights (black plus signs). The red dashed line indicates the inward extrapolation of the fitted bulge Sérsic profile to SINFONI FOV. The dashed line encloses the extended radius of nuclear stellar excess component.

- *Middle right panel:* The radial flux profile of nuclear stellar excess (the inward extrapolation of the fitted bulge Sérsic profile has been subtracted) and fit a simple gaussian profile that is plotted as purple solid line.

- *Bottom left panel:* The circular velocity of stars as a function of radius to the SINFONI FOV, which is extracted by using the IDL routine *kinemetry*. The inclination has been corrected based on the large-scale host galaxy inclination. Black dashed line is the size of nuclear excess component.

- *Bottom right panel:* The LOS velocity dispersion of stars as a function of radius to the SINFONI FOV, which is extracted by using the IDL routine *kinemetry*. Black dashed line is the size of nuclear excess component. Pink solid line is the mean LOS stellar velocity dispersion at the radius larger than black dashed line, pink dashed lines are the  $\pm 3\sigma$  errors of mean LOS stellar velocity dispersion, which can be a criterion to check whether there is a significant variation in the centre (refer to column (5) in Table 3.2).

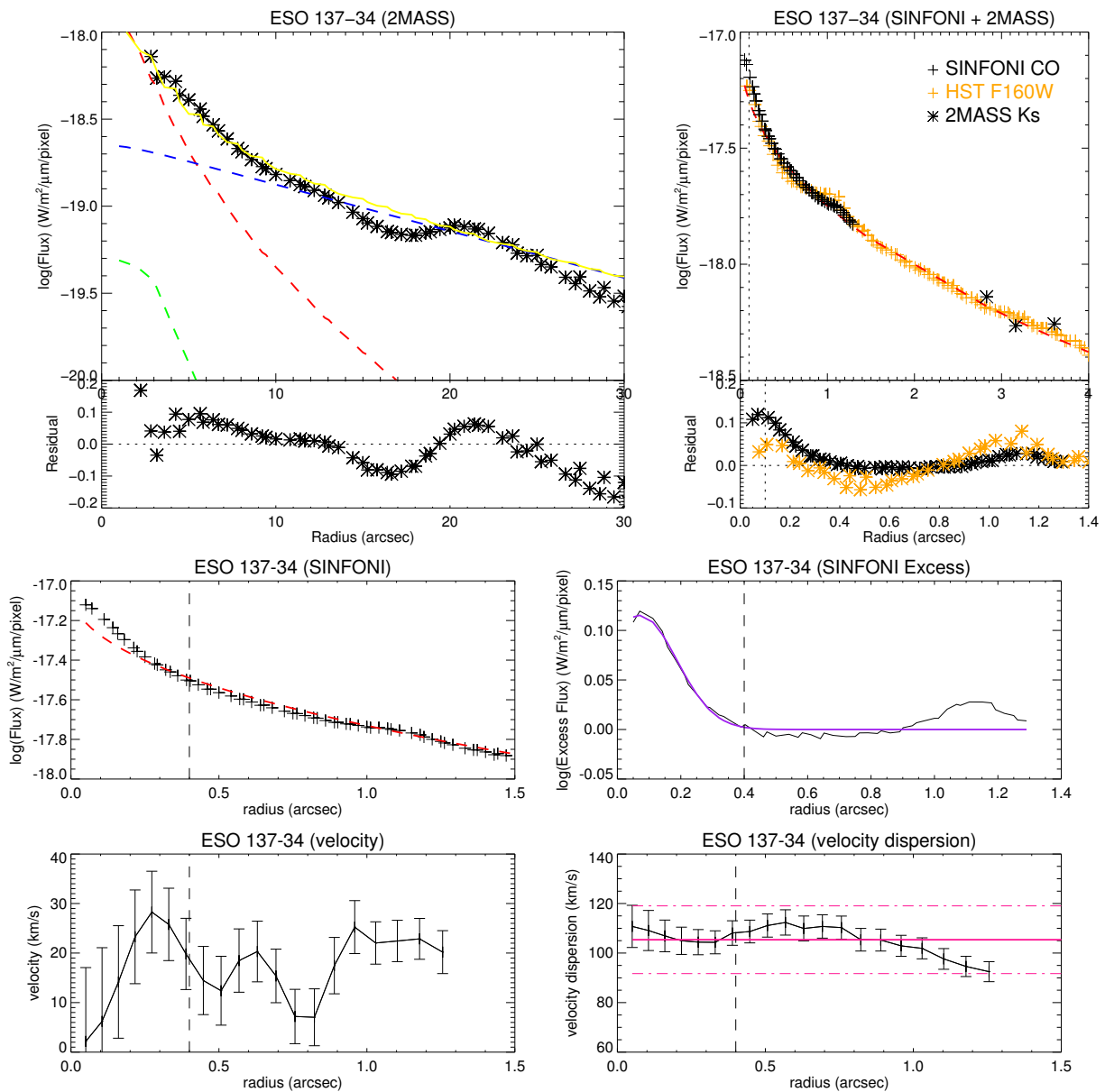


Figure B.1: ESO 137-34 (Active galaxy in Pair 1).

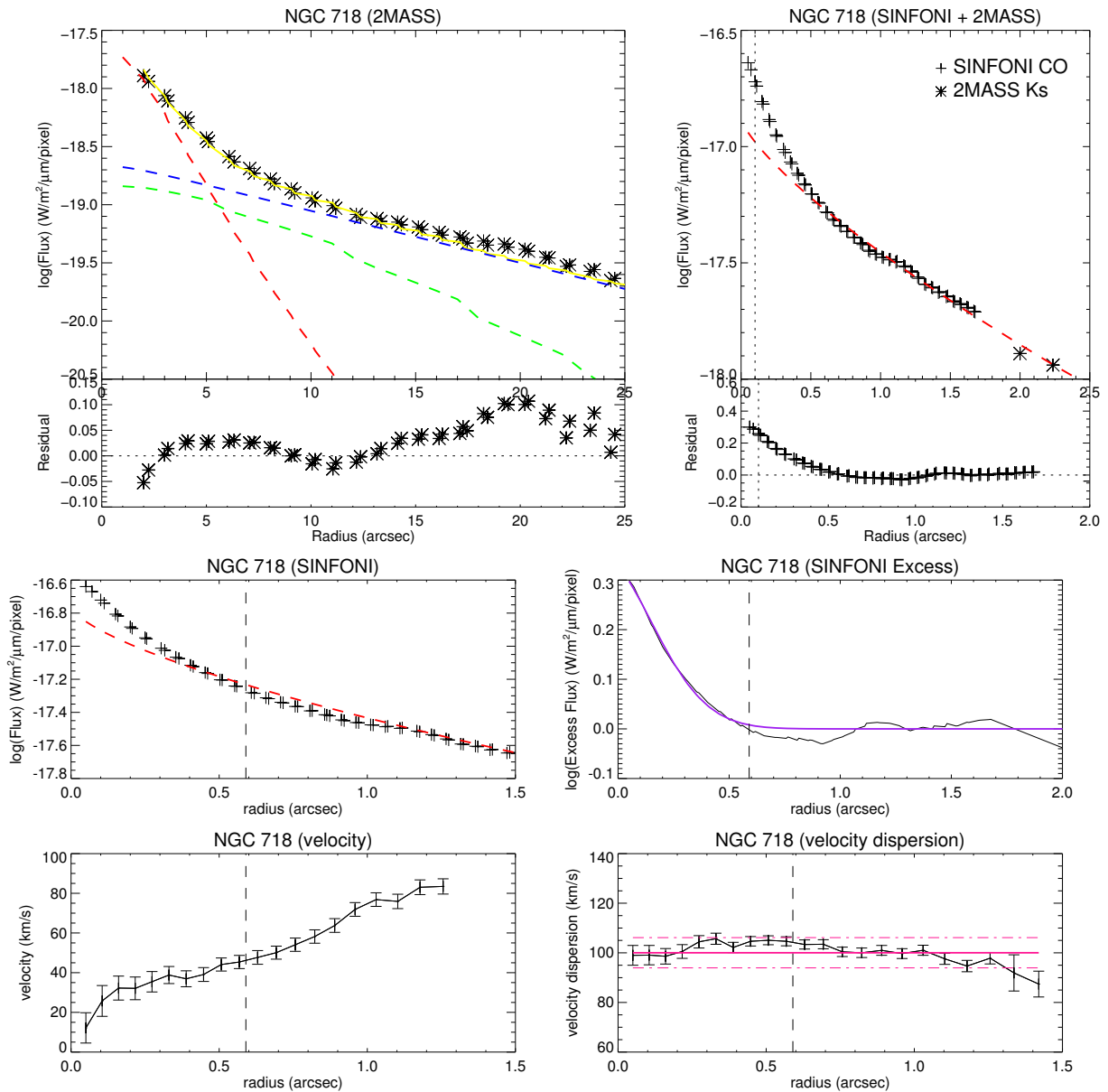


Figure B.2: NGC 718 (Inactive galaxy in Pair 6).

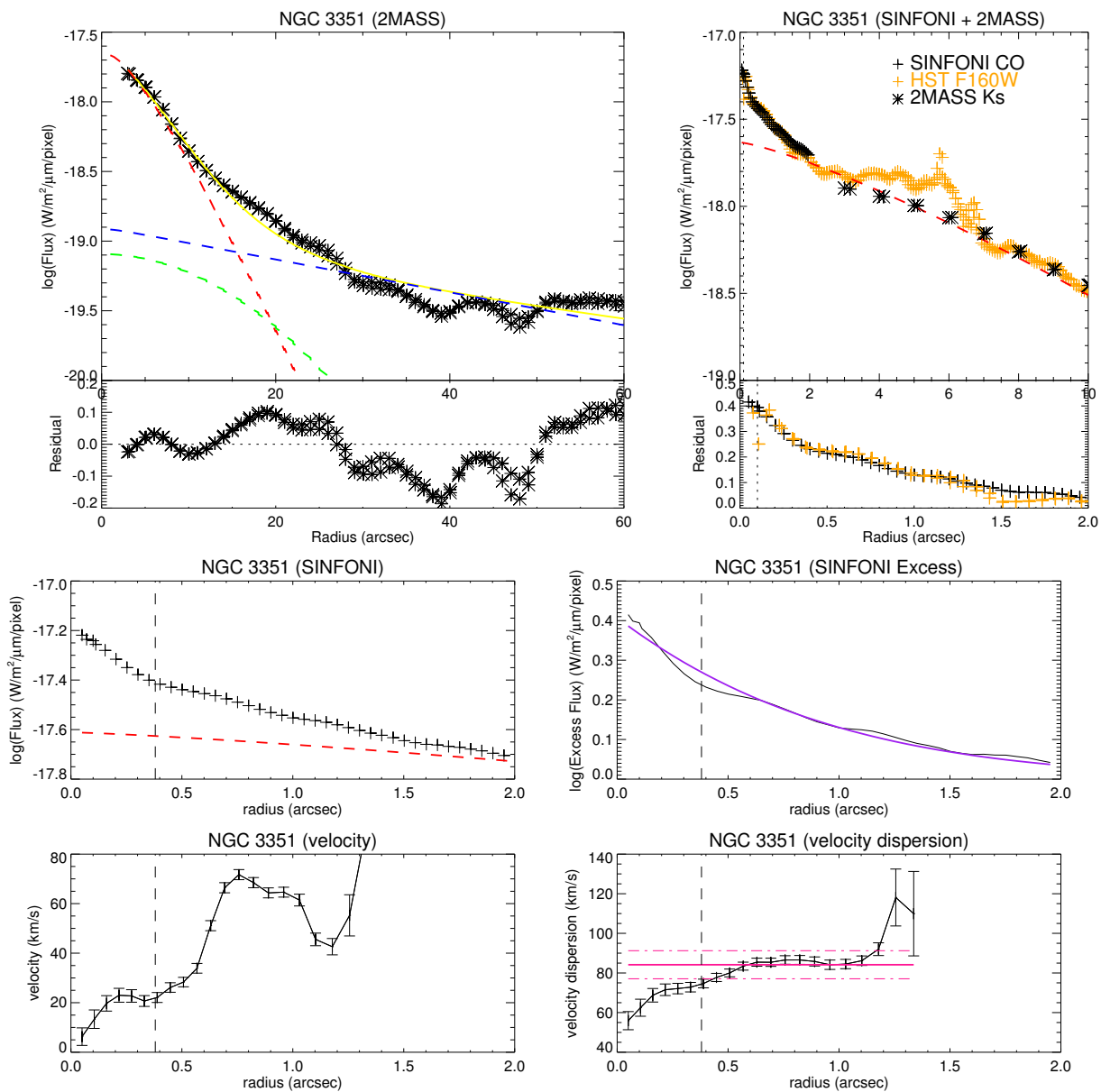


Figure B.3: NGC 3351 (Inactive galaxy in Pair 7). The excess flux distributes entire SINFONI FOV, the black dashed lines in the middle and bottom rows present the size of nuclear cusp. Furthermore, the velocity dispersion drops can be obviously seen inside the nuclear cusp.

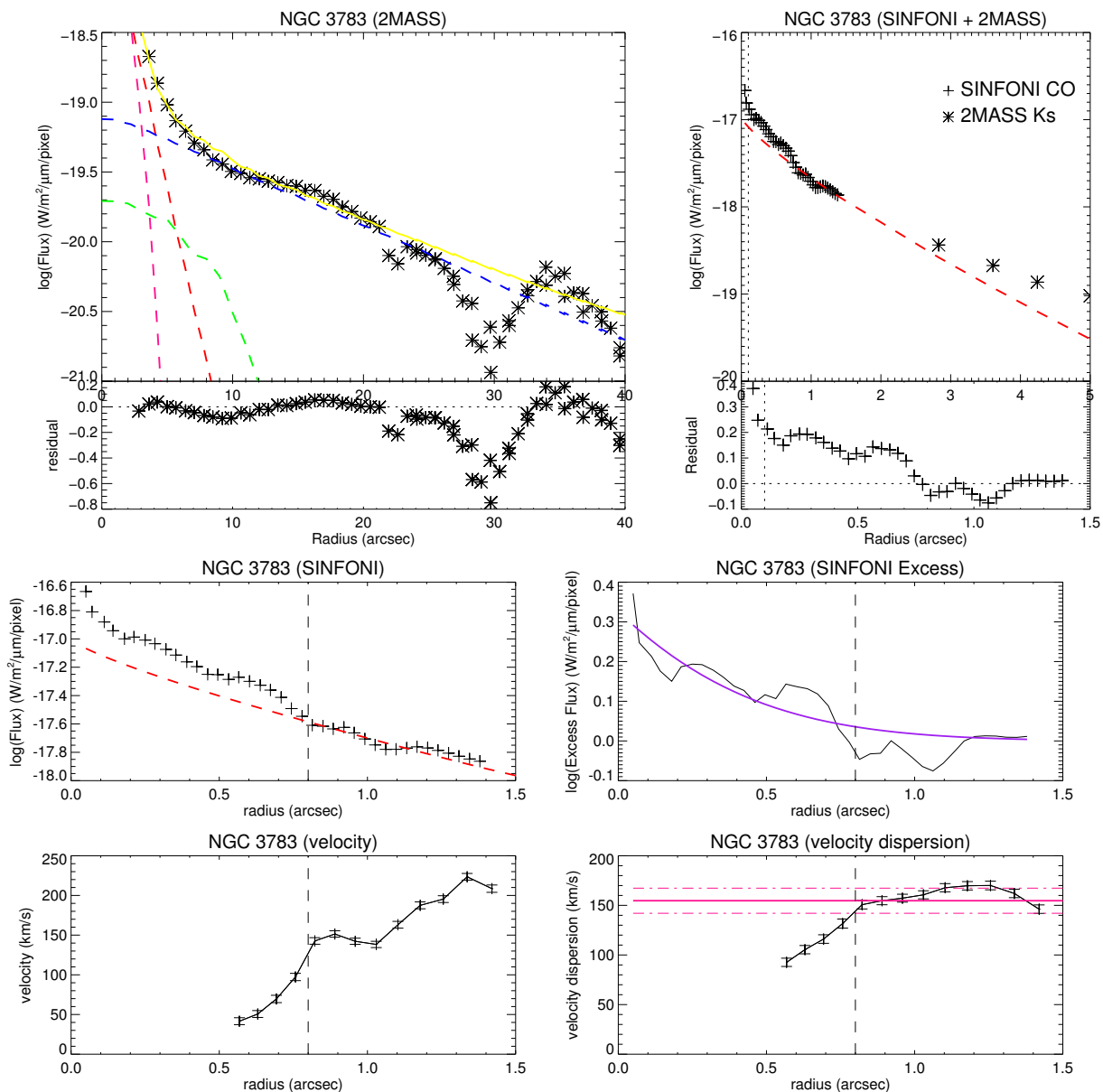


Figure B.4: NGC 3783 (Active galaxy in Pair 6). Because its nucleus is bright in 2MASS Ks image, we add additional PSF during two-dimension fitting and plot it as deep pink dashed line in the top left panel.

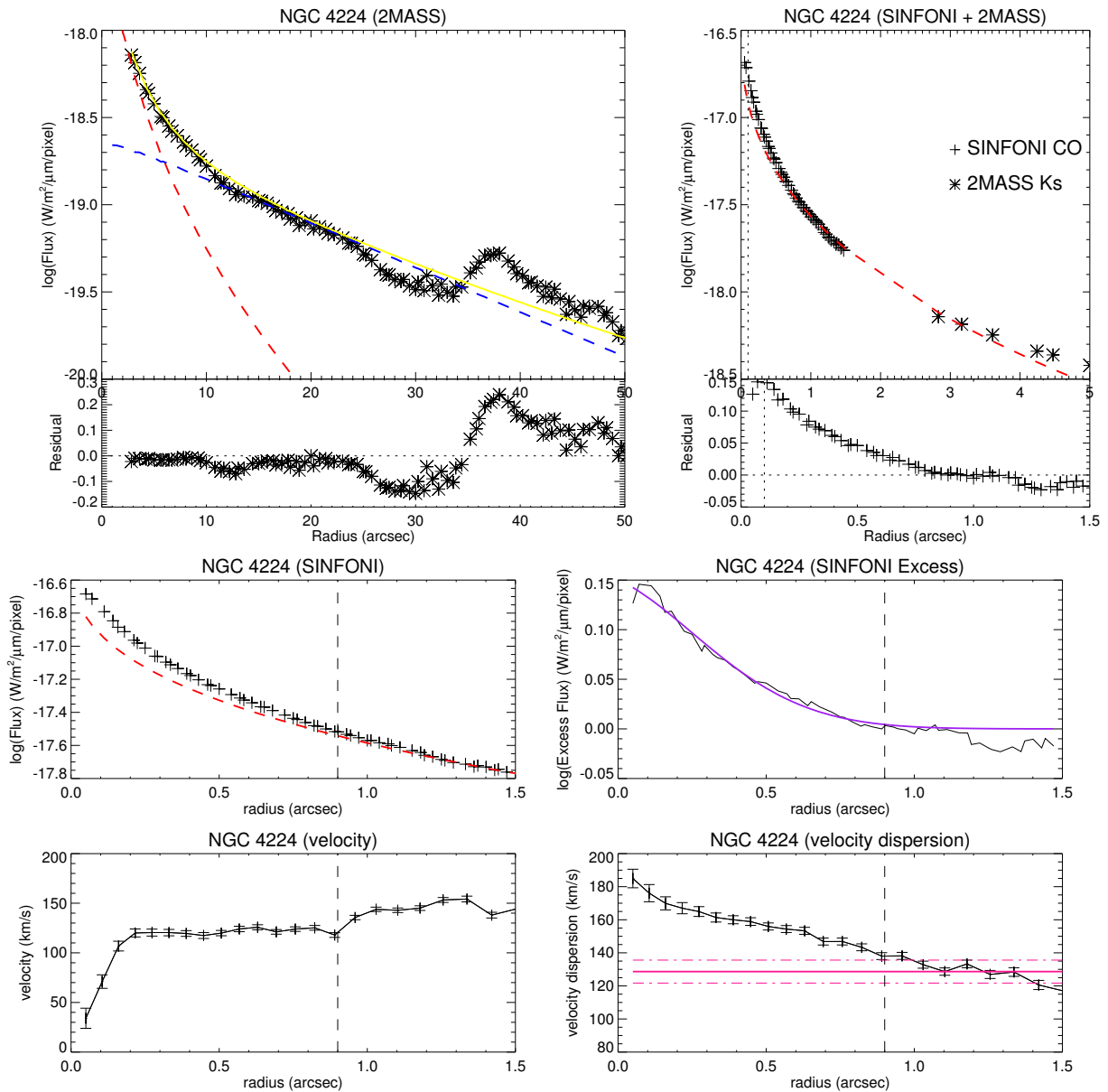


Figure B.5: NGC 4224 (Inactive galaxy in Pair 3 and Pair 5).

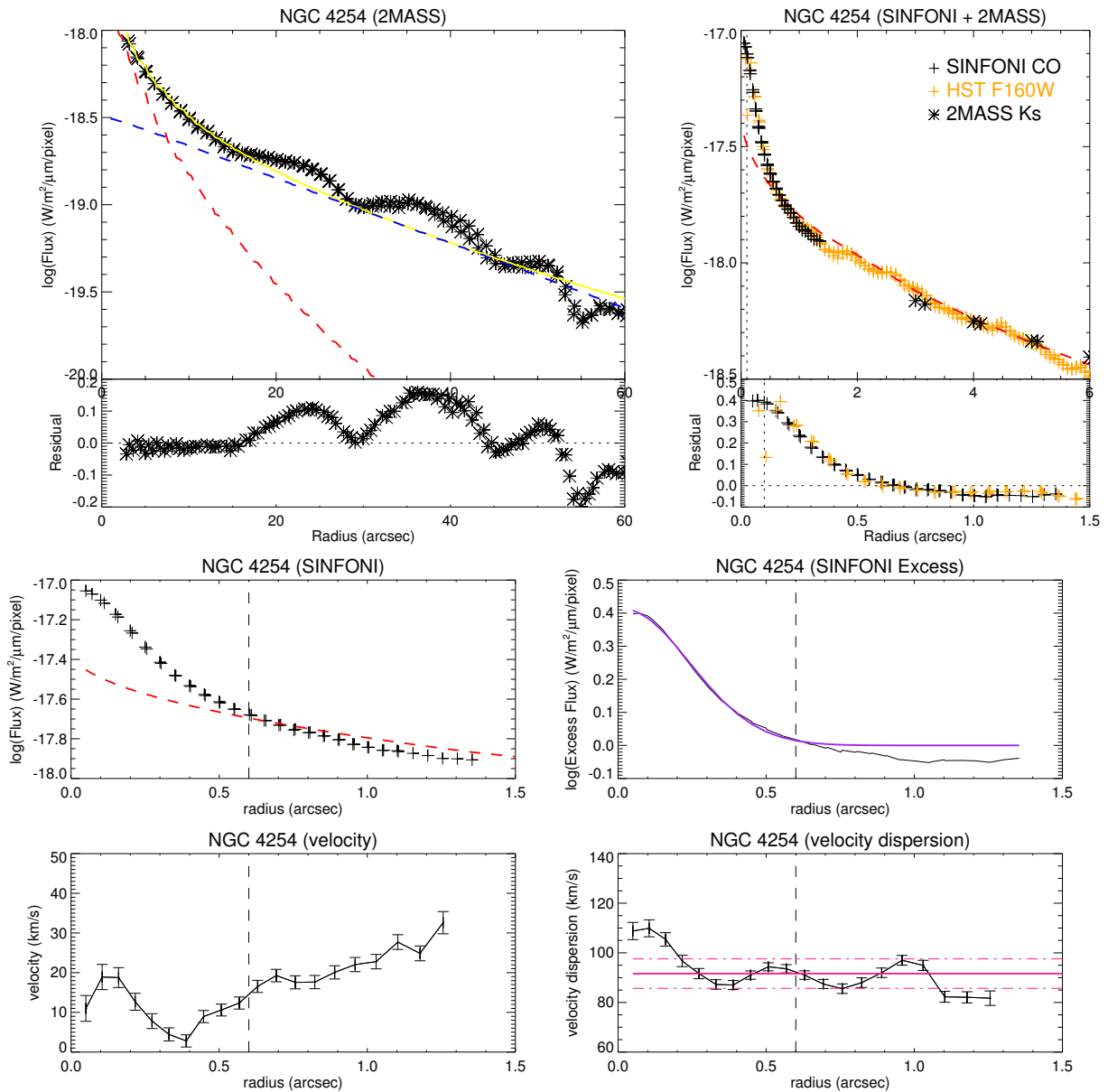


Figure B.6: NGC 4254 (Inactive galaxy in Pair 8).

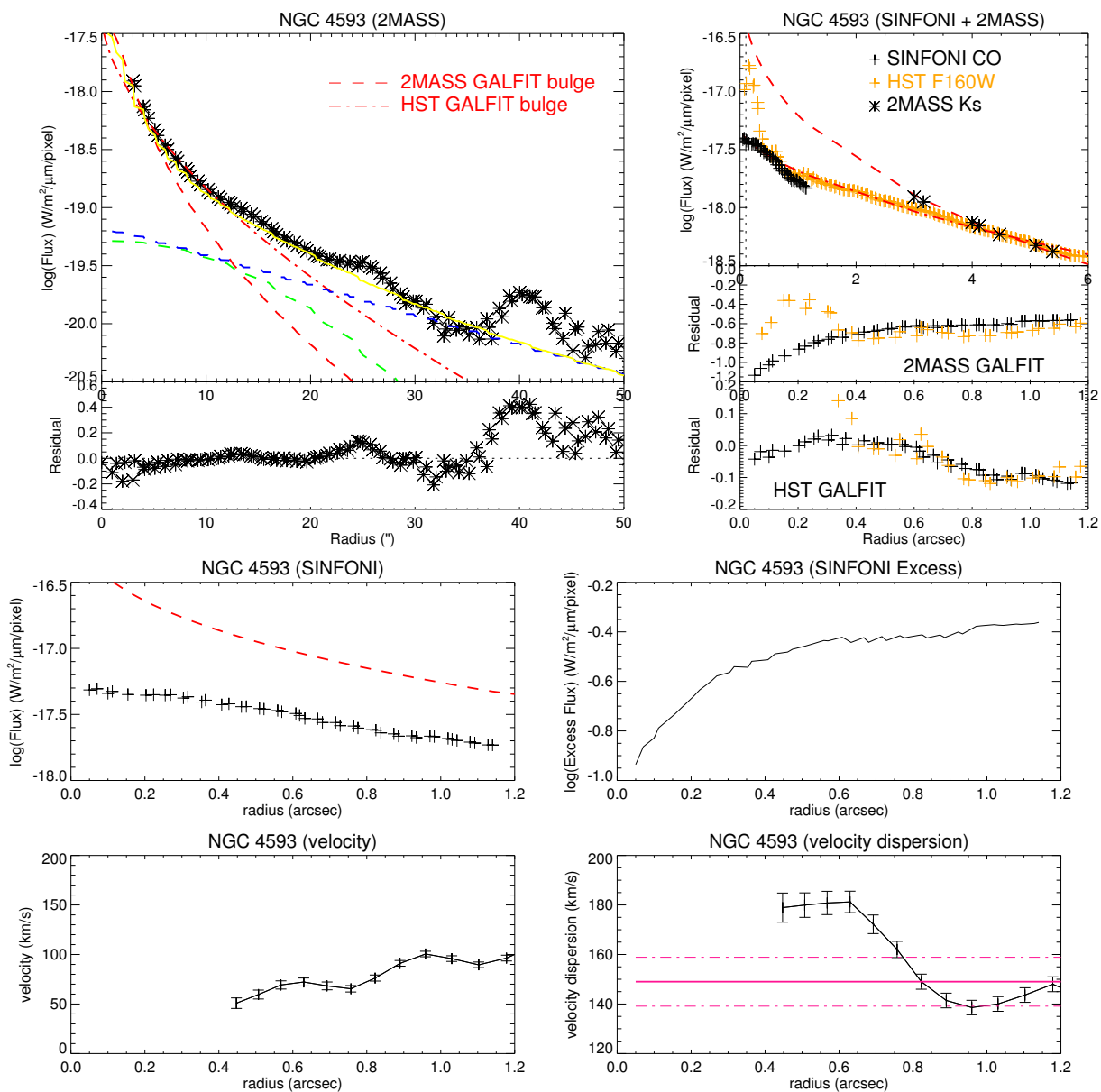


Figure B.7: NGC 4593 (Active galaxy in Pair 7). Top left panel: In addition to measuring bulge Sérsic profile based on 2MASS image, we use GALFIT to fit HST F160W image, which is presented in red dot-dashed line. Top right panel: The combined large-scale 2MASS, HST images and small-scale SINFONI image. We do not see any significant nuclear stellar excess toward the centre in both 2MASS and HST residuals. Middle and bottom panels:

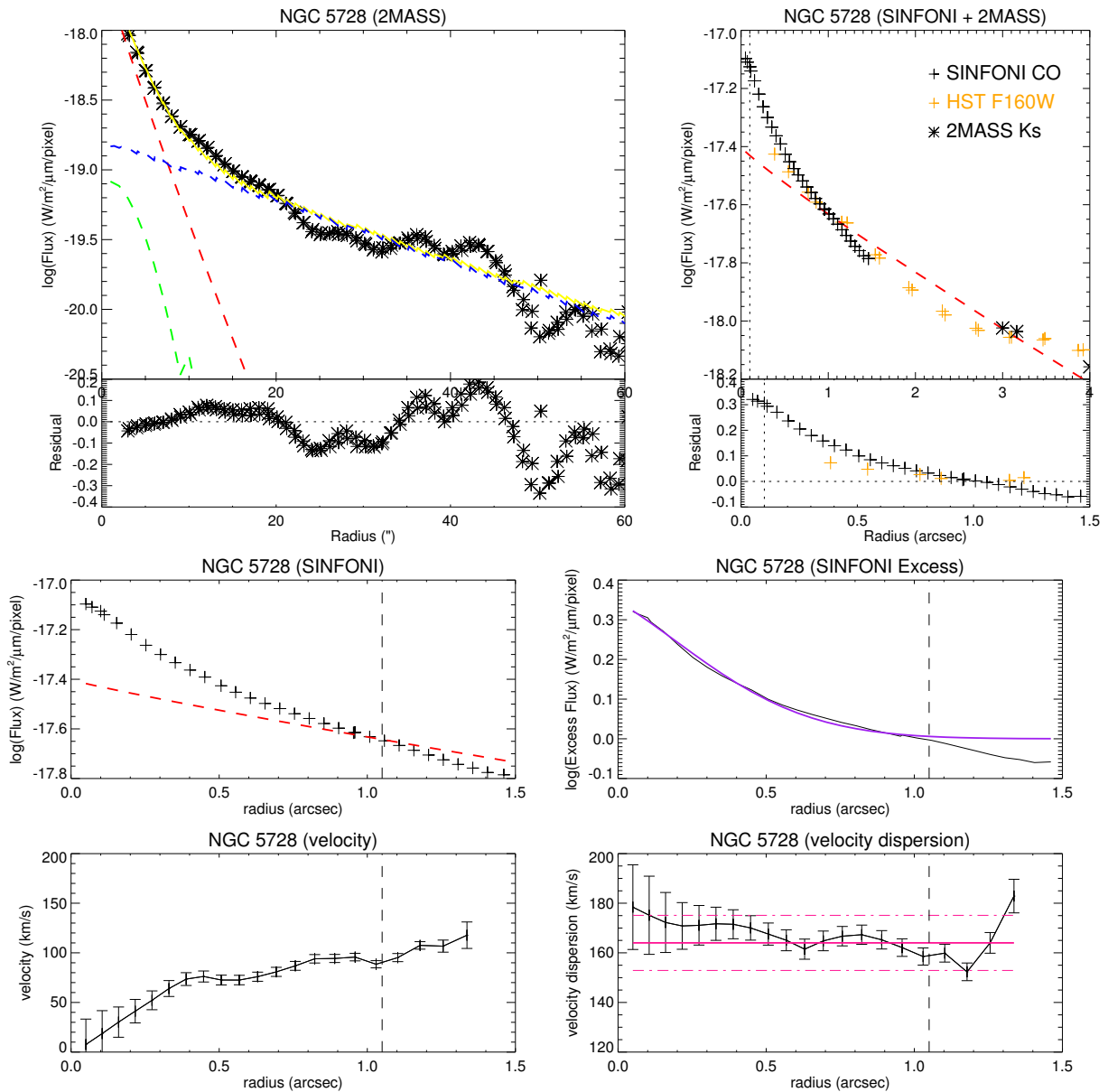


Figure B.8: NGC 5728 (Active galaxy in Pair 4).

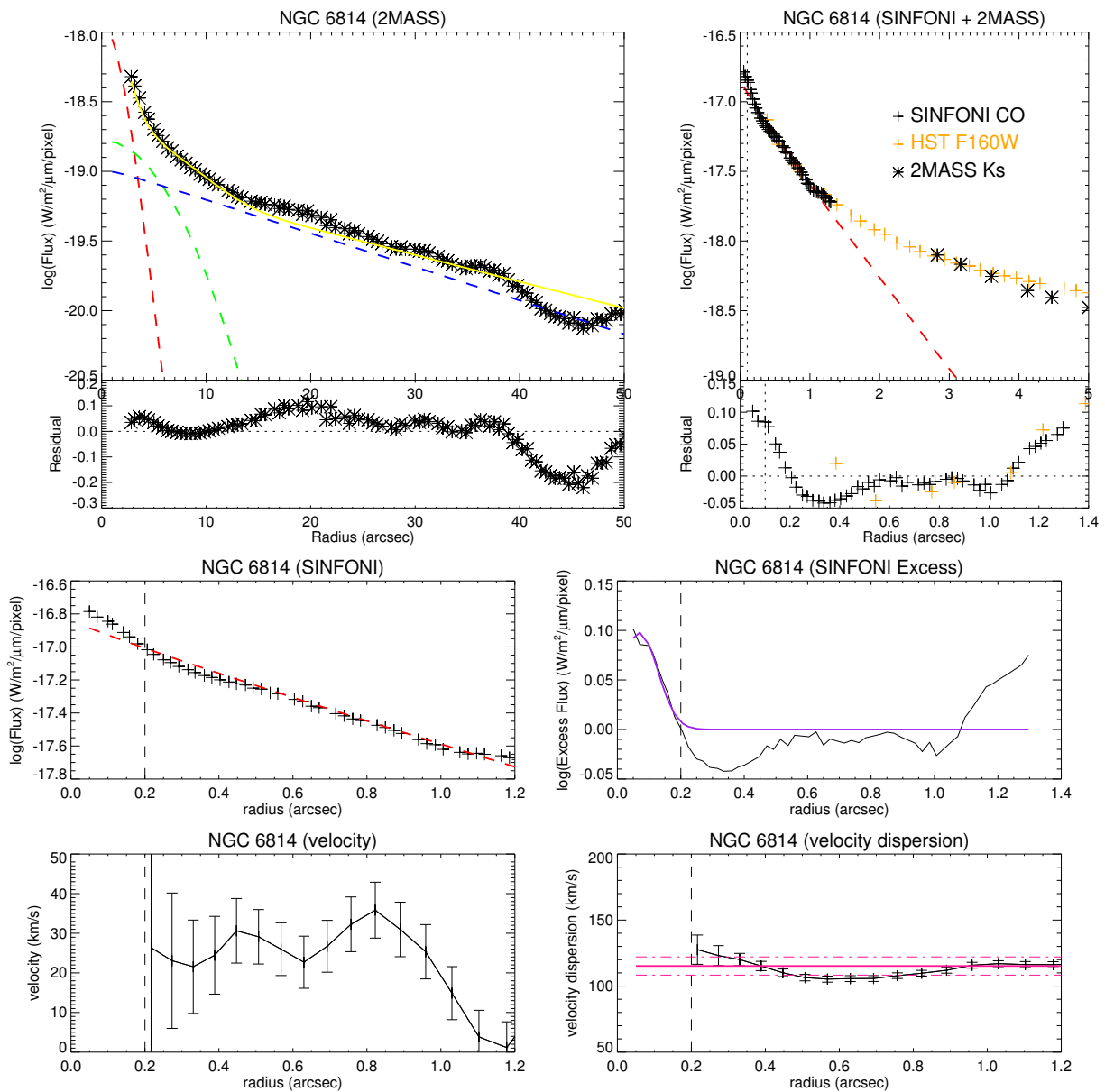


Figure B.9: NGC 6814 (Active galaxy in Pair 8).

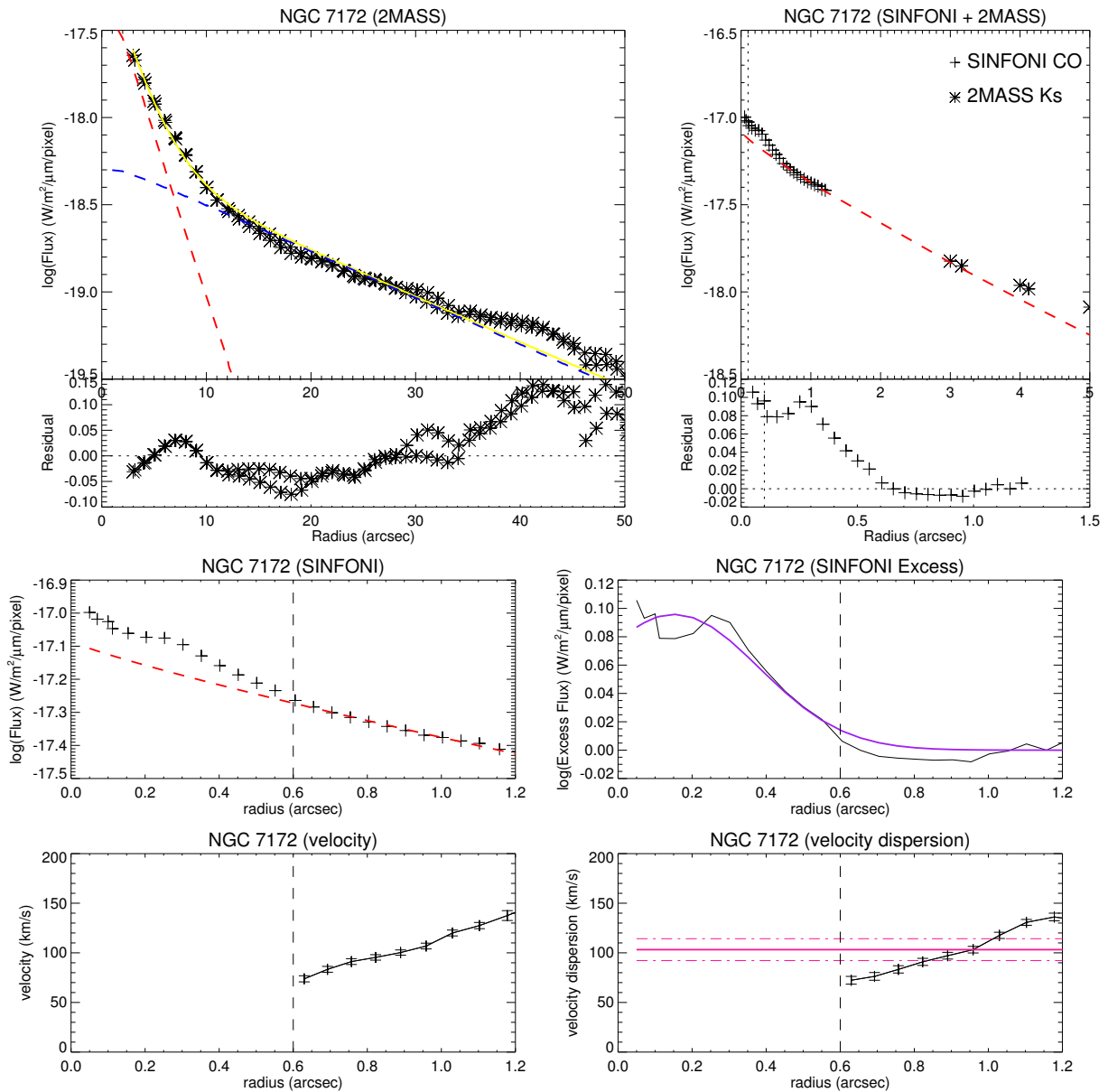


Figure B.10: NGC 7172 (Active galaxy in Pair 3).

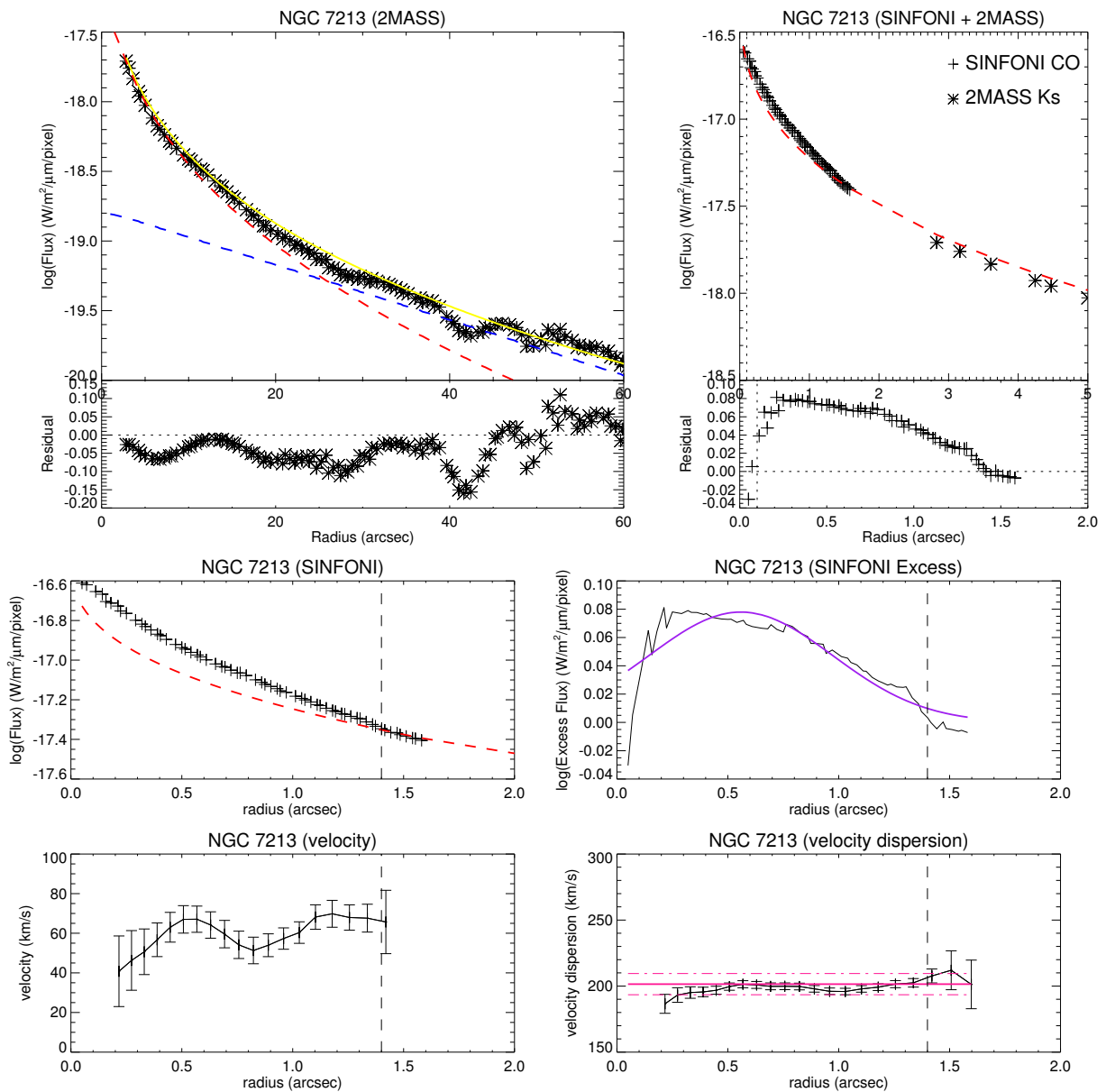


Figure B.11: NGC 7213 (Active galaxy in Pair 2).

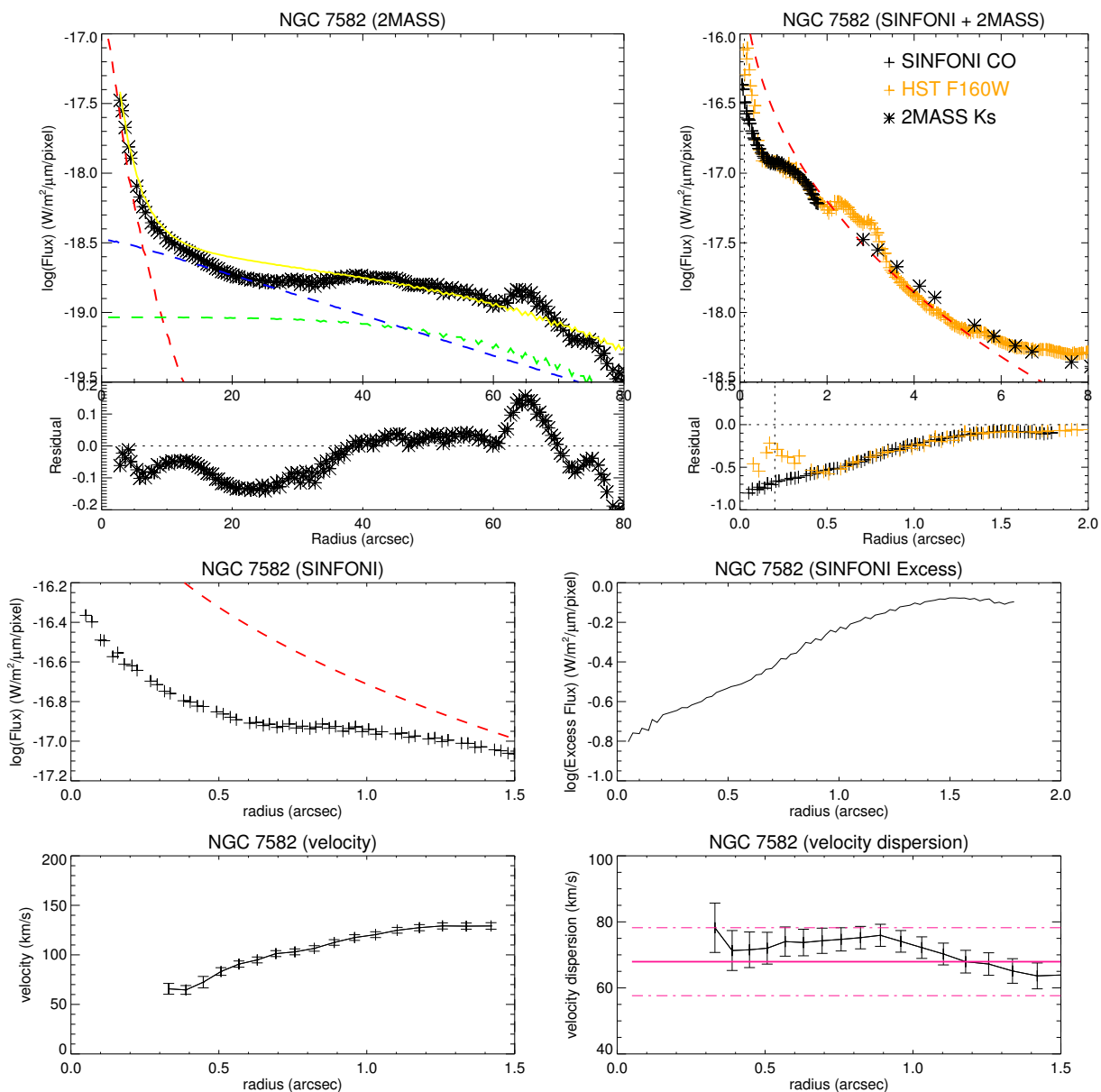


Figure B.12: NGC 7582 (Active galaxy in Pair 5).

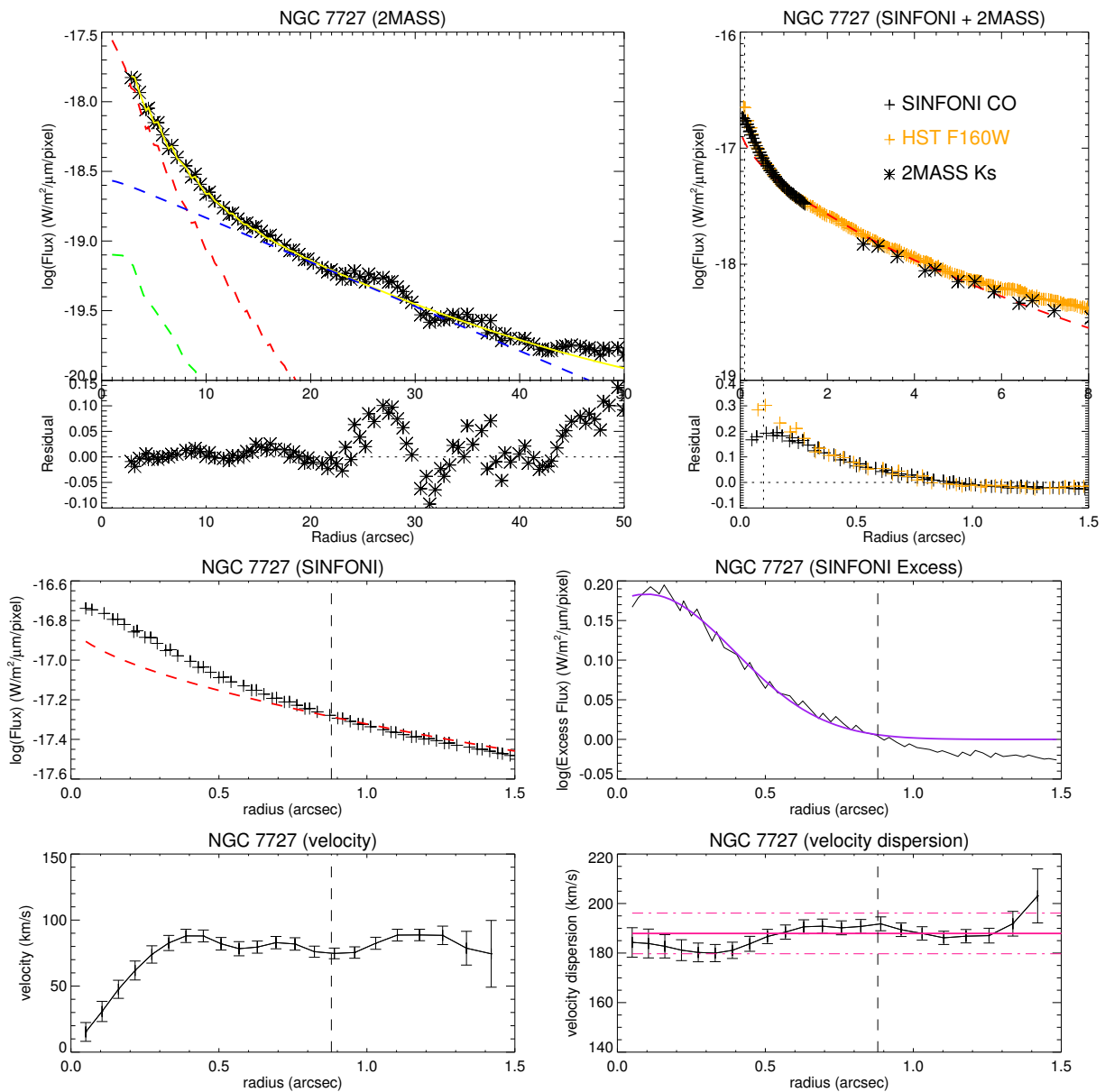


Figure B.13: NGC 7727 (Inactive galaxy in Pair 1, 2, and 4).



# Bibliography

- Aalto S., Martín S., Costagliola F., González-Alfonso E., Muller S., et al., 2015, *A&A*, 584, A42
- Abuter, R., Schreiber, J., Eisenhauer, F., et al. 2006, *New Astron. Rev.*, 50, 398
- Alonso-Herrero, A., Quillen, A. C., Simpson, C., Efstathiou, A., & Ward, M. J. 2001, *AJ*, 121, 1369
- Antonucci, R. R. J., & Miller, J. S. 1985, *ApJ*, 297, 621
- Antonucci, R., 1993, *ARA&A*, 31, 473
- Antonini, F. 2013, *ApJ*, 763, 62
- Balcells, M., Graham, A. W., & Peletier, R. F. 2007, *ApJ*, 665, 1084
- Barnes, E. I., & Sellwood, J. A. 2003, *AJ*, 125, 1164
- Baumgartner, W. H., Tueller, J., Markwardt, C. B., et al. 2013, *ApJS*, 207, 19
- Beckmann, V., & Shrader, C. 2012, *Active Galactic Nuclei*, 1st ed., ISBN: 9783527410910
- Bellocchi, E., Arribas, S., & Colina, L. 2012, *Aap*, 542, A54
- Bender, R., Saglia, R. P., & Gerhard, O. E. 1994, *MNRAS*, 269, 785
- Bennert, N., Canalizo, G., Jungwiert, B., et al. 2008, *ApJ*, 677, 846-857
- Bergin E., Tafalla M., 2007, *ARA&A*, 45, 339
- Bianchi, S., Chiaberge, M., Piconcelli, E., & Guainazzi, M. 2007, *MNRAS*, 374, 697
- Bianchi, S., Piconcelli, E., Chiaberge, M., et al. 2009, *ApJ*, 695, 781
- Boger G., Sternberg A., 2005, *ApJ*, 632, 302
- Böker, T., Sarzi, M., McLaughlin, D. E., et al. 2004, *AJ*, 127, 105
- Bonnet, H., Abuter, R., Baker, A., et al. 2004, *The Messenger*, 117, 17

- Bönsch G., Potulski E., 1998, *Metrologia*, 35, 13
- Braine J., Guélin M., Dumke M., Brouillet N., Herpin F., Wielebinski R., 1997, *A&A*, 326, 963
- Burtscher, L., Orban de Xivry, G., Davies, R. I., et al. 2015, *Aap* , 578, A47
- Buta, R., & Combes, F. 1996, *fcp* , 17, 95
- Cappellari, M., & Emsellem, E. 2004, *PASP* , 116, 138
- Cappellari, M., Emsellem, E., Bacon, R., et al. 2007, *MNRAS* , 379, 418
- Cappellari, M., McDermid, R. M., Bacon, R., et al. 2010, *American Institute of Physics Conference Series*, 1240, 211
- Cecil, G., Bland-Hawthorn, J., Veilleux, S., & Filippenko, A. V., 2001, *ApJ*, 555, 338
- Cecil, G., Bland-Hawthorn, J., & Veilleux, S., 2002, *ApJ*, 576, 745
- Cheung, E., Trump, J. R., Athanassoula, E., et al. 2015, *MNRAS* , 447, 506
- Cid Fernandes, R., González Delgado, R. M., Schmitt, H., et al. 2004, *ApJ* , 605, 105
- Cisternas, M., Sheth, K., Salvato, M., et al. 2015, *ApJ* , 802, 137
- Cole, D. R., Debattista, V. P., Erwin, P., Earp, S. W. F., & Roškar, R. 2014, *MNRAS* , 445, 3352
- Combes, F. 2001, *Advanced Lectures on the Starburst-AGN*, 223
- Combes, F., García-Burillo, S., Casasola, V., et al., 2013, *A&A*, 558, A124
- Corsini, E. M., Morelli, L., Pastorello, N., et al. 2016, *MNRAS* , 457, 1198
- Costagliola, F., Aalto, S., Rodriguez, M. I., et al., 2011, *A&A*, 528, A30
- Côté, P., Piatek, S., Ferrarese, L., et al. 2006, *ApJS* , 165, 57
- Côté, P., Ferrarese, L., Jordán, A., et al. 2007, *ApJ* , 671, 1456
- Davis, R. J., Muxlow, T. W. B., & Unwin, S. C. 1991, *Nature*, 354, 374
- Davies, R. I., Tacconi, L. J., & Genzel, R., 2004, *ApJ*, 602, 148
- Davies, R. I., Thomas, J., Genzel, R., et al. 2006, *ApJ* , 646, 754
- Davies, R. I. 2007, *MNRAS* , 375, 1099
- Davies, R. I., Müller Sánchez, F., Genzel, R., et al. 2007, *ApJ* , 671, 1388

- Davies, R. I., Maciejewski, W., Hicks, E. K. S., et al. 2009, ApJ , 702, 114
- Davies, R., Förster Schreiber, N. M., Cresci, G., et al., 2011, ApJ, 741, 69
- Davies, R., Mark, D., & Sternberg, A., 2012, A&A, 537, A133
- Davies, R. I., Maciejewski, W., Hicks, E. K. S., et al. 2014, ApJ , 792, 101
- Davies, R. I., Burtscher, L., Rosario, D., et al. 2015, ApJ , 806, 127
- Davies, R. I., et al. 2017, MNRAS , 466, 4917
- de Vaucouleurs, G., de Vaucouleurs, A., Corwin, H. G., Jr., et al. 1991, Third Reference Catalogue of Bright Galaxies. Volume I: Explanations and references. Volume II: Data for galaxies between  $0^h$  and  $12^h$ . Volume III: Data for galaxies between  $12^h$  and  $24^h$ ., by de Vaucouleurs, G.; de Vaucouleurs, A.; Corwin, H. G., Jr.; Buta, R. J.; Paturel, G.; Fouqué, P.. Springer, New York, NY (USA), 1991, 2091 p., ISBN 0-387-97552-7, Price US 198.00. ISBN 3-540-97552-7, Price DM 448.00. ISBN 0-387-97549-7 (Vol. I), ISBN 0-387-97550-0 (Vol. II), ISBN 0-387-97551-9 (Vol. III)., I
- Dib, S., Bell, E., & Burkert, A. 2006, ApJ , 638, 797
- Downes, D., Genzel, R., Hjalmarsen, A., Nyman, L. A., & Ronnang, B., 1982, ApJL, 252, L29
- Downes, D., Solomon, P. M., & Radford, S. J. E., 1993, ApJL, 414, L13
- Dumas, G., Mundell, C. G., Emsellem, E., & Nagar, N. M. 2007, MNRAS , 379, 1249
- Edelson, R. A., & Malkan, M. A. 1986, ApJ , 308, 59
- Eisenhauer, F., Abuter, R., Bickert, K., et al. 2003, procs pie , 4841, 1548
- Elitzur, M. 2012, ApJL , 747, L33
- Elitzur, M., & Shlosman, I., 2006, ApJL, 648, L101
- Emsellem, E., Greusard, D., Combes, F., et al. 2001, Aap , 368, 52
- Engel H., Davies R., Genzel R., Tacconi L., Sturm E., Downes D., 2011, ApJ, 729, 58
- Esquej, P., Alonso-Herrero, A., González-Martín, O., et al. 2014, ApJ , 780, 86
- Fabian, A. C. 2010, Co-Evolution of Central Black Holes and Galaxies, 267, 341
- Fabian, A. C. 2012, ARA&A, 50, 455
- Feltre, A., Hatziminaoglou, E., Fritz, J., & Franceschini, A., 2012, MNRAS, 426, 120
- Feruglio, C., Maiolino, R., Piconcelli, E., et al. 2010, Aap , 518, L155

- Filippenko, A. V. 1982, PASP , 94, 715
- Fisher, D. B., & Drory, N. 2008, AJ , 136, 773
- Fritz J., Franceschini A., Hatziminaoglou E., 2006, MNRAS, 366, 767
- Gao, Y., Carilli, C. L., Solomon, P. M., & Vanden Bout, P. A., 2007, ApJL, 660, L93
- Gao, Y., & Solomon, P. M., 2004, ApJS, 152, 63
- García-Burillo S., Combes F., Usero A., Aalto S., Krips M., et al., 2014, A&A, 567, A125
- Genzel, R., Eisenhauer, F., & Gillessen, S. 2010, Reviews of Modern Physics, 82, 3121
- Goldsmith P., 2001, ApJ, 557, 736
- Gottlieb C., Gottlieb E., Thaddeus P., 1983, ApJ, 264, 740
- Graham, A. W., & Guzmán, R. 2003, AJ , 125, 2936
- Granato, G. L., & Danese, L., 1994, MNRAS, 268, 235
- Granato, G. L., Danese, L., & Franceschini, A., 1997, ApJ, 486, 147
- Greene, J. E., & Ho, L. C. 2007, ApJ , 667, 131
- Greene, J. E., Seth, A., Lyubenova, M., et al. 2014, ApJ , 788, 145
- Guillard, N., Emsellem, E., & Renaud, F. 2016, MNRAS , 461, 3620
- Haan, S., Schinnerer, E., Emsellem, E., et al. 2009, ApJ , 692, 1623
- Hagiwara, Y., Klöckner, H.-R., & Baan, W., 2004, MNRAS, 353, 1055
- Hailey-Dunsheath S., Sturm E., Fischer J., Sternberg A., Graciá-Carpio J., et al., 2012, ApJ, 755, 57
- Harada, N., Herbst, E., & Wakelam, V., 2010, ApJ, 721, 1570
- Hawarden T., Israel F., Geballe T., Wade R., 1995, MNRAS, 276, 1197
- Heckman T., Armus L., Miley G., 1990, ApJSS, 74, 833
- Herrnstein, J. R., Moran, J. M., Greenhill, L. J., et al. 1999, Nature, 400, 539
- Hicks, E. K. S., Davies, R. I., Malkan, M. A., et al., 2009, ApJ, 696, 448
- Hicks, E. K. S., Davies, R. I., Maciejewski, W., et al. 2013, ApJ , 768, 107
- Ho, L. C., Filippenko, A. V., & Sargent, W. L. W. 1997, ApJ , 487, 579

- Ho, L. C., Filippenko, A. V., & Sargent, W. L. W. 1997, *ApJS* , 112, 315
- Ho, L. C. 2008, *ARA&A*, 46, 475
- Ho, I.-T., Medling, A. M., Bland-Hawthorn, J., et al. 2016, *MNRAS* , 457, 1257
- Holtzman, J. A., Faber, S. M., Shaya, E. J., et al. 1992, *AJ* , 103, 691
- Hoenig S., Beckert T., Ohnaka K., Weigelt G., 2006, *A&A*, 452,459
- Hönig, S. F., & Kishimoto, M. 2010, *Aap* , 523, A27
- Hopkins, P. F., Cox, T. J., Younger, J. D., & Hernquist, L. 2009, *ApJ* , 691, 1168
- Hopkins, P. F., & Quataert, E. 2010, *MNRAS* , 407, 1529
- Hopkins, P. F., Hayward, C. C., Narayanan, D., & Hernquist, L., 2012, *MNRAS*, 420, 320
- Hopkins, P. F. 2012, *MNRAS* , 420, L8
- Hopkins, P. F., Torrey, P., Faucher-Giguère, C.-A., Quataert, E., & Murray, N. 2016, *MNRAS* , 458, 816
- Hota A., Saikia D., 2006, *MNRAS*, 371, 945
- Hsieh P.-Y., Ho P., Kohno K., Hwang C.-Y., Matsushita S., 2012, *ApJ*, 747, 90
- Huchra J., Geller M., Corwin H., 1995 *ApJSS*, 99, 391
- Hung, C.-L., Rich, J. A., Yuan, T., et al. 2015, *ApJ* , 803, 62
- Iyomoto, N., Fukazawa, Y., Nakai, N., & Ishihara, Y., 2001, *ApJL*, 561, L69
- Kaspi, S., Brandt, W. N., George, I. M., et al. 2002, *ApJ* , 574, 643
- Kellermann, K. I., Sramek, R., Schmidt, M., Shaffer, D. B., & Green, R. 1989, *AJ* , 98, 1195
- Khachikian, E. Y., & Weedman, D. W. 1974, *ApJ* , 192, 581
- Kharb, P., Hota, A., Croston, J. H., et al., 2010, *ApJ*, 723, 580
- Klaas U., Walker H., 2002, *A&A*, 391, 911
- Klaassen, P. D., & Wilson, C. D., 2007, *ApJ*, 663, 1092
- Koda, J., Sofue, Y., Kohno, K., et al., 2002, *ApJ*, 573, 105
- Kohno, K., Vila-Vilaró, B., Sakamoto, S., et al., 2003, *PASJ*, 55, 103

- Kohno K., 2005, in *The Evolution of Starbursts: The 331st Wilhelm and Else Heraeus Seminar*, AIP Conf. Proc. vol. 783, pp. 203–208
- Kohno, K., Nakanishi, K., Tosaki, T., et al., 2008, *Ap&SS*, 313, 279
- Kondratko, P. T., Greenhill, L. J., & Moran, J. M., 2005, *ApJ*, 618, 618
- Kormendy, J., & Ho, L. C. 2013, *ARA&A*, 51, 511
- Koss, M., Mushotzky, R., Veilleux, S., et al. 2011, *ApJ* , 739, 57
- Koss, M. J., Assef, R., Baloković, M., et al. 2016, *ApJ* , 825, 85
- Krajnović, D., Cappellari, M., de Zeeuw, P. T., & Copin, Y. 2006, *MNRAS* , 366, 787
- Krajnović, D., Emsellem, E., Cappellari, M., et al. 2011, *MNRAS* , 414, 2923
- Krips, M., Neri, R., Garcá-Burillo, S., et al., 2007, *A&A*, 468, L63
- Krips, M., Neri, R., García-Burillo, S., et al., 2008, *ApJ*, 677, 262
- Krips, M., Martín S., Eckart A., Neri R., Garcá-Burillo S., et al., 2011, *ApJ*, 736, 37
- Krolik, Julian H., 1998, *Active Galactic Nuclei: From the Central Black Hole to the Galactic Environment*, 1st ed., ISBN-10: 0691011516
- Krolik, J. H., & Begelman, M. C., 1988, *ApJ*, 329, 702
- Krongold, Y., Nicastro, F., Brickhouse, N. S., et al. 2003, *ApJ* , 597, 832
- Kukula M., Pedlar A., Baum S., O’Dea C., 1995, *MNRAS*, 276, 1262
- Lin, M.-Y., Davies, R. I., Burtscher, L., et al. 2016, *MNRAS* , 458, 1375
- Lindt-Krieg, E., Eckart, A., Neri, R., et al. 2008, *Aap* , 479, 377
- Leon, S., Eckart, A., Laine, S., et al., 2007, *A&A*, 473, 747
- Lepp, S., & Dalgarno, A., 1996, *A&A*, 306, L21
- Lynden-Bell, D. 1969, *Nature*, 223, 690
- Malkan, M. A., Gorjian, V., & Tam, R. 1998, *ApJS* , 117, 25
- Maloney P., Hollenbach D., Tielens A., 1996, *ApJ*, 466, 561
- Maiolino, R., & Risaliti, G. 2007, *The Central Engine of Active Galactic Nuclei*, 373, 447
- Marconi, A., Risaliti, G., Gilli, R., et al. 2004, *MNRAS* , 351, 169
- Martini, P., Regan, M., Mulchaey, J., Pogge, R. 2003, *ApJS* , 146, 353

- Martín, S., Aladro, R., Martín-Pintado, J., & Mauersberger, R., 2010, *A&A*, 522, A62
- Martin-Pintado, J., Bachiller, R., & Fuente, A., 1992, *A&A*, 254, 315
- Mazzalay, X., Maciejewski, W., Erwin, P., et al. 2014, *MNRAS* , 438, 2036
- Meijerink, R., & Spaans, M., 2005, *A&A*, 436, 397
- Meijerink, R., Spaans, M., & Israel, F. P., 2007, *A&A*, 461, 793
- Menezes, R. B., da Silva, P., Ricci, T. V., et al. 2015, *MNRAS* , 450, 369
- Mezcua, M., Prieto, M. A., Fernández-Ontiveros, J. A., & Tristram, K. R. W. 2016, *MNRAS* , 457, L94
- Middelberg E., Agudo I., Roy A., Krichbaum T., 2007, *MNRAS*, 377, 731
- Milam, S. N., Savage, C., Brewster, M. A., Ziurys, L. M., & Wyckoff, S., 2005, *ApJ*, 634, 1126
- Miller, J. S., & Goodrich, R. W. 1990, *ApJ* , 355, 456
- Morganti R., Holt J., Saripalli L., Oosterloo T., Tadhunter Cl., 2007, *A&A*, 476, 735
- Morganti R., 2012 in *Nuclei of Seyfert galaxies and QSOs – Central engine & conditions of star formation*, Proceedings of Science, pub. Max-Planck-Institut für Radioastronomie (MPIfR), Bonn, Germany; online at <https://pos.sissa.it/cgi-bin/reader/conf.cgi?confid=169>
- Morganti R., Oosterloo T., Oonk J., Frieswijk W., Tadhunter Cl., 2015, *A&A*, 580, 1
- Mukherjee, D., Bicknell, G. V., Sutherland, R., & Wagner, A. 2016, *MNRAS* , 461, 967
- Mulchaey, J. S., & Regan, M. W. 1997, *ApJL* , 482, L135
- Muller S., Dinh-V-Trung, 2009, *ApJ*, 696, 176
- Müller Sánchez, F., Davies, R. I., Genzel, R., et al. 2009, *ApJ* , 691, 749
- Müller-Sánchez, F., Prieto, M. A., Mezcua, M., et al., 2013, *ApJL*, 763, L1
- Nenkova, M., Ivezić, Ž., & Elitzur, M., 2002, *ApJL*, 570, L9
- Netzer, H., Kaspi, S., Behar, E., et al. 2003, *ApJ* , 599, 933
- Netzer H., 2015, *ARA&A*, 53, 365
- Nenkova, M., Sirocky, M. M., Nikutta, R., Ivezić, Ž., & Elitzur, M. 2008, *ApJ* , 685, 160-180
- Nishiyama, S., Nagata, T., Tamura, M., et al. 2008, *ApJ* , 680, 1174-1179

- Osterbrock, D. E. 1977, *ApJ* , 215, 733
- Padovani, P., & Urry, C. M. 1992, *ApJ* , 387, 449
- Papadopoulos, P. P., 2007, *ApJ*, 656, 792
- Peterson, Bradley M., 1997, *An Introduction to Active Galactic Nuclei*, 1st ed., ISBN-10: 0521479118
- Pérez-Torres, M. A., & Alberdi, A., 2007, *MNRAS*, 379, 275
- Pier E., Krolik J., 1992, *ApJ*, 401, 99
- Portaluri, E., Corsini, E. M., Morelli, L., et al. 2013, *MNRAS* , 433, 434
- Predehl, P., & Schmitt, J. H. M. M. 1995, *Aap* , 293, 889
- Querejeta, M., Schinnerer, E., García-Burillo, S., et al. 2016, *Aap* , 593, A118
- Rangwala N., Maloney P., Wilson C., Glenn J., Kamenetzky J., Spinoglio L., 2015, *ApJ*, 806, 17
- Rees, M. J. 1984, *ARA&A*, 22, 471
- Ricci, C., Ueda, Y., Koss, M. J., et al. 2015, *ApJL* , 815, L13
- Ricci, C., Bauer, F. E., Treister, E., et al. 2017, *MNRAS* , 468, 1273
- Riffel, R., Pastoriza, M. G., Rodríguez-Ardila, A., & Bonatto, C. 2009, *MNRAS* , 400, 273
- Riffel, R. A., Storchi-Bergmann, T., Dors, O. L., & Winge, C. 2009, *MNRAS* , 393, 783
- Riffel, R. A., Storchi-Bergmann, T., & Winge, C. 2013, *MNRAS* , 430, 2249
- Riffel, R. A., Ho, L. C., Mason, R., et al. 2015, *MNRAS* , 446, 2823
- Sakamoto K., Aalto S., Wilner D., Black J., Conway J., et al., 2009, *ApJ*, 700, L104
- Salpeter, E. E. 1964, *ApJ* , 140, 796
- Sani E., et al. 2012, *MNRAS* , 424, 1963
- Sarzi, M., Ledo, H. R., Coccato, L., et al. 2016, *MNRAS* , 457, 1804
- Schartmann M., Meisenheimer K., Camenzind M., Wolf S., Henning T., 2005, *A&A*, 437, 861
- Schartmann M., Meisenheimer K., Camenzind M., Wolf S., Tristram K., Henning T., 2008, *A&A*, 482, 67

- Schartmann M., Wada K., Prieto M.A., Burkert A., Tristram K., 2014, MNRAS, 445, 3878
- Schawinski, K., Koss, M., Berney, S., & Sartori, L. F. 2015, MNRAS , 451, 2517
- Schnorr-Müller A., et al. 2016, MNRAS , 462, 3570
- Schnorr-Müller, A., Storchi-Bergmann, T., Robinson, A., Lena, D., & Nagar, N. M. 2016, MNRAS , 457, 972
- Schnorr-Müller, A., Storchi-Bergmann, T., Ferrari, F., & Nagar, N. M. 2017, MNRAS , 466, 4370
- Schweitzer, M., Lutz, D., Sturm, E., et al. 2006, ApJ , 649, 79
- Schweitzer, M., Groves, B., Netzer, H., et al., 2008, ApJ, 679, 101
- Schöier, F. L., van der Tak, F. F. S., van Dishoeck, E. F., & Black, J. H., 2005, A&A, 432, 369
- Seth, A. C., Cappellari, M., Neumayer, N., et al. 2010, ApJ , 714, 713
- Shapiro, K. L., Genzel, R., Förster Schreiber, N. M., et al. 2008, ApJ , 682, 231-251
- Sheth, K., Regan, M., Hinz, J. L., et al. 2010, PASP , 122, 1397
- Shlosman, I. 2013, Secular Evolution of Galaxies, 555
- Smajić, S., Fischer, S., Zuther, J., & Eckart, A. 2012, Aap , 544, A105
- Sobolev V., 1957, SvA, 1, 678
- Sofue, Y., & Rubin, V., 2001, ARA&A, 39, 137
- Solomon P., Radford S., Downes D., 1990, ApJL, 348, 53
- Solomon P.M. & Vanden Bout P.A., 2005, ARA&A, 43, 677
- Son, D.-H., Hyung, S., Ferruit, P., Pécontal, E., & Lee, W.-B. 2009, MNRAS , 395, 692
- Sternberg, A., & Dalgarno, A., 1995, ApJS, 99, 565
- Stevens J., Gear W., 2000, MNRAS, 312, L5
- Storchi-Bergmann, T., González Delgado, R. M., Schmitt, H. R., Cid Fernandes, R., & Heckman, T. 2001, ApJ , 559, 147
- Storchi-Bergmann, T., Dors, O. L., Jr., Riffel, R. A., et al. 2007, ApJ , 670, 959
- Storchi-Bergmann, T. 2014, Resolving The Future Of Astronomy With Long-Baseline Interferometry, 487, 199

- Takamiya, T., & Sofue, Y., 2002, *ApJL*, 576, L15
- Tempel, E., & Tenjes, P. 2006, *MNRAS* , 371, 1269
- Teng, S. H., & Veilleux, S. 2010, *ApJ* , 725, 1848
- Thean A., Mundell C., Pdelar A., & Nicholson R., 1997, *MNRAS*, 290, 15
- Thompson, T. A., Quataert, E., & Murray, N., 2005, *ApJ*, 630, 167
- Tristram, K. R. W., Burtscher, L., Jaffe, W., et al., 2014, *A&A*, 563, AA82
- Trotter, A. S., Greenhill, L. J., Moran, J. M., et al., 1998, *ApJ*, 495, 740
- Ulvestad, J. S. 2003, *Radio Astronomy at the Fringe*, 300, 97
- Unger, S. W., Pedlar, A., Axon, D. J., et al. 1987, *MNRAS* , 228, 671
- Urry, C. M., & Padovani, P., 1995, *PASP*, 107, 803
- Usero A., García-Burillo S., Fuente A., Martín-Pintado J., Rodríguez-Fernández N., 2004, *A&A*, 419, 897
- van der Marel, R. P., & Franx, M. 1993, *ApJ* , 407, 525
- Veilleux, S., Cecil, G., Bland-Hawthorn, J., et al., 1994, *ApJ*, 433, 48
- Veilleux, S., Rupke, D. S. N., Kim, D.-C., et al. 2009, *ApJS* , 182, 628-666
- Vernet, J., Dekker, H., D’Odorico, S., et al. 2011, *Aap* , 536, A105
- Viti S., García-Burillo S., Fuente A., Hunt L., Usero A., et al. 2014, *A&A*, 570, A28
- Vollmer B., Beckert T., Davies R., 2008, *A&A*, 491, 441
- Vollmer, B. 2009, *Aap* , 502, 427
- Wada, K., & Norman, C. A., 2002, *ApJL*, 566, L21
- Wada K., Papadopoulos P., Spaan M., 2009, *ApJ*, 702, 63
- Wada K., 2012, *ApJ*, 758, 66
- Wagner, S. J., Bender, R., & Dettmar, R.-J. 1989, *Aap* , 215, 243
- Weinzirl, T., Jogee, S., Khochfar, S., Burkert, A., & Kormendy, J. 2009, *ApJ* , 696, 411
- White R., Becker R., Helfand D., Gregg M., 1997, *ApJ*, 475, 479
- Wiklind, T., & Combes, F., 1995, *A&A*, 299, 382

Winge, C., Riffel, R. A., & Storchi-Bergmann, T. 2009, *ApJS* , 185, 186

Wozniak, H., Combes, F., Emsellem, E., & Friedli, D. 2003, *Aap* , 409, 469

Yamagishi M., Kande H., Ishihara D., Komugi S., Suzuki T., Onaka T., 2010, *PASJ*, 62, 1085

Zaragoza-Cardiel J., Font J., Beckman J., García-Lorenzo B., Erroz-Ferrer S., Gutiérrez L., 2014, *MNRAS*, 445, 1412

Ziurys, L. M., Snell, R. L., & Dickman, R. L., 1989, *ApJ*, 341, 857

Ziurys, L. M., Friberg, P., & Irvine, W. M., 1989, *ApJ*, 343, 201



# Acknowledgements

First of all, I want to thank my supervisor, Richard Davies. This thesis would never been completed without his supports. Ric always is a supportive, patient and considerate supervisor. When I face any trouble and problem, he always generously provides helpful suggests, assisting me to overcome the challenges. I would like to thank Reinhard Genzel for giving me an opportunity to do my doctoral research in MPE IR group. I also want to thank Eckhard Sturm and Linda Tacconi for being part of my thesis committee, providing kind helps and shaping my research projects. I also want to thank Dieter Lutz for providing useful scientific comments.

I am grateful to be a member of LLAMA project. In particular, many thanks go to Leonard Burtscher, David Rosario, Taro Shimizu and Gilles Orban de Xivry, they give great support in these research works. I thank all collaborators for providing deeply suggestions and insights into my research: Erin K. S. Hicks, Thaisa Storchi-Bergmann, Witold Maciejewski, Rogério Riffel, Rogemar A. Riffel, Marc Schartmann, Michael Koss, Claudio Ricci, Francisco Müller-Sánchez, Allan Schnorr-Müller, Amiel Sternberg, Sylvain Veilleux, Alessandra Contursi, Javier Graciá-Carpio, E. González-Alfonso. Special thank go to Eva Wuyt for giving me an opportunity to go to LBT for observing. I am thankful for all past and present members of the MPE IR group, such a nice and friendly environment inspires people's passion to explore Universe in deeper. Especially thanks to Annemieke Janssen and Magdalena Lippa, I enjoy a great time with them. I also want to give many thanks to Peter Buschkamp, Phillip Lang, Philipp Plewa, Nadia Murillo, Hannah Übler, Paolo Cazzoletti, Rebecca Davies, and Susanne Dengler. All of them are kind to give me helps, either to this thesis or to my daily life at MPE.

Finally, I dedicate this thesis to my parents, Ching-Yuan Lin & Shing-Yung Chang in Taiwan.